SANDIA REPORT
SAND2008-5801
Unlimited Release
Printed September 2008

Supersedes SAND2005-7959 dated December 2005, SAND2007-0969
Dated March 2007

Nanostructured Electrocatalyst for Fuel Cells: Silica Templated Synthesis of Pt/C Composites

Elise E. Switzer, Chris Cornelius, Cy H. Fujimoto, Michael Hibbs, Ellen Stechel and Plamen Atanassov

Prepared by Sandia National Laboratories Albuquerque, New Mexico 87185 and Livermore, California 94550

Sandia is a multiprogram laboratory operated by Sandia Corporation, a
Lockheed Martin Company, for the United States Department of Energy's
National Nuclear Security Administration under Contract DE-AC04-94AL85000.

Issued by Sandia National Laboratories, operated for the United States Department of Energy by Sandia Corporation.

Available to DOE and DOE contractors from
U.S. Department of Energy
Office of Scientific and Technical Information

P.O. Box 62
Oak Ridge, TN 37831

Telephone: (865)576-8401
Facsimile: (865)576-5728
E-Mail: reports@adonis.osti.gov
Online ordering: http://www.osti.gov/bridge

Available to the public from
U.S. Department of Commerce
National Technical Information Service
5285 Port Royal Rd
Springfield, VA 22161

Telephone: (800)553-6847
Facsimile: (703)605-6900
E-Mail: orders@ntis.fedworld.gov
Online order: http://www.ntis.gov/help/ordermethods.asp?loc=7-4-0#online

SAND2008-5801

Unlimited Release

Printed September 2007

Supersedes SAND2005-7959 dated December 2005, SAND2007-0969

Dated March 2007

Nanostructured Electrocatalyst for Fuel Cells: Silica Templated Synthesis of Pt/C Composites

Abstract

Platinum-based electrocatalysts are currently required for state-of-the-art fuel cells and represent a significant portion of the overall fuel cell cost. If fuel cell technology is to become competitive with other energy conversion technologies, improve the utilization of precious metal catalysts is essential. A primary focus of this work is on creating enhanced nanostructured materials which improve precious-metal utilization. The goal is to engineer superior electrocatalytic materials through the synthesis, development and investigation of novel templated open frame structures synthesized in an aerosol-based approach.

Bulk templating methods for both Pt/C and Pt-Ru composites are evaluated in this study and are found to be limited due to the fact that the nanostructure is not maintained throughout the entire sample. Therefore, an accurate examination of structural effects was previously impossible. An aerosol-based templating method of synthesizing nanostructured Pt-Ru electrocatalysts has been developed wherein the effects of structure can be related to electrocatalytic performance. The aerosol-based templating method developed in this work is extremely versatile as it can be conveniently modified to synthesize alternative materials for other systems. The synthesis method was able to be extended to nanostructured Pt-Sn for ethanol oxidation in alkaline media.

Nanostructured Pt-Sn electrocatalysts were evaluated in a unique approach tailored to electrocatalytic studies in alkaline media. At low temperatures, nanostructured Pt-Sn electrocatalysts were found to have significantly higher ethanol oxidation activity than a comparable nanostructured Pt catalyst. At higher temperatures, the oxygen-containing species contribution likely provided by Sn is insignificant due to a more oxidized Pt surface. The importance of the surface coverage of oxygen-containing species in the reaction mechanism is established in these studies. The investigations in this work present original studies of anion exchange ionomers as entrapment materials for rotating disc electrode (RDE) studies in alkaline media. Their significance is linked to the development of membrane electrode assemblies (MEAs) with the same ionomer for a KOH-free alkaline fuel cell (AFC).

TABLE OF CONTENTS

LIST OF FIGURES

LIST OF TABLES

1 INTRODUCTION

1.1 Fuel Cell Basics

1.1.1 Proton Exchange Membrane Fuel Cell (PEMFC)

In response to several significant global issues, a research initiative exists to develop environmentally clean and efficient alternatives to fossil fuels and the internal combustion engine. One particular energy conversion device, the fuel cell, has been at the forefront as a possible economically viable power source. While there are numerous different types and applications of fuel cells, one of the most favorable aspects is its association with clean emissions and renewable fuels. In simple terms, a fuel cell is an electrochemical system that converts chemical energy into electrical energy. Figure 1.1 is a schematic of the most basic type fuel cell, namely the proton-exchange membrane fuel cell (PEMFC) fueled by hydrogen gas.

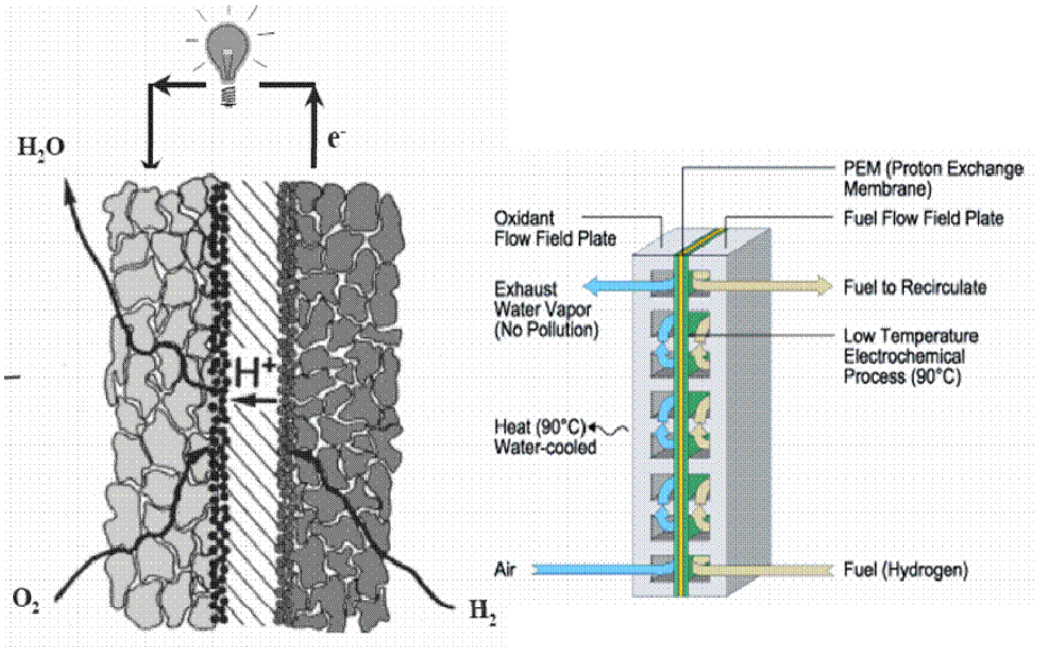

Figure 1.1: Operation and configuration of the basic Proton-Exchange Membrane Fuel Cell (PEMFC). The illustration on the left depicts the membrane electrode assembly (MEA) which consists of a gas diffusion layer and catalytic layer on either side of the proton-exchange membrane. The illustration on the right shows the integrated MEA in addition to the gas flow fields which comprises one complete fuel cell.

Hydrogen gas is fed to the fuel cell anode and travels through the gas diffusion layer (GDL) to the anodic catalytic layer. In this catalytic layer, hydrogen gas is oxidized which results in proton transfer through the proton exchange membrane and electron transfer through an electrical circuit. At the same time, oxygen gas is fed to the cathode and upon diffusion to the cathodic catalytic layer, it is reduced to water. These anodic and cathodic reactions as well as the overall cell reaction are shown in Equation 1-1.

$$\begin{aligned} &ANODE: H_2 \longrightarrow 2H^+ + 2e^- \\ &CATHODE: \frac{1}{2}O_2 + 2H^+ + 2e^- \longrightarrow H_2O \\ &OVERALL: H_2 + \frac{1}{2}O_2 \longrightarrow 2H_2O \end{aligned} \qquad \textbf{(1-1)}$$

The principle method to evaluate fuel cell performance is through a polarization curve. The theoretical cell voltage maximum is known as the thermodynamic open circuit potential (OCP). The theoretical OCP is calculated from Equation 1-2 where E^+ and E^- represent the cathode and anode potentials, respectively. These standard potentials can be calculated from thermodynamic data of each anodic and cathodic species, namely Gibbs energy of formation ΔG_f. The number of electrons transferred is represented by n and F represents the Faraday constant (96,485 C/mol).

$$E^0 = E^+ - E^- = \frac{-\Delta G_f^+}{nF} + \frac{-\Delta G_f^-}{nF} \quad \textbf{(1-2)}$$

By definition, the electrode potential for the anodic reaction (E^-) is 0 V vs. SHE (Standard Hydrogen Electrode) and the electrode potential for the cathodic reaction (E^+) is 1.229 V vs. SHE. Therefore, in the case of a hydrogen/oxygen fuel cell operating under standard conditions, the OCP or standard electromotive force (E^0) is approximately 1.229 V vs. SHE. This thermodynamic OCP is shown in a typical polarization curve exemplified by Figure 1.2.

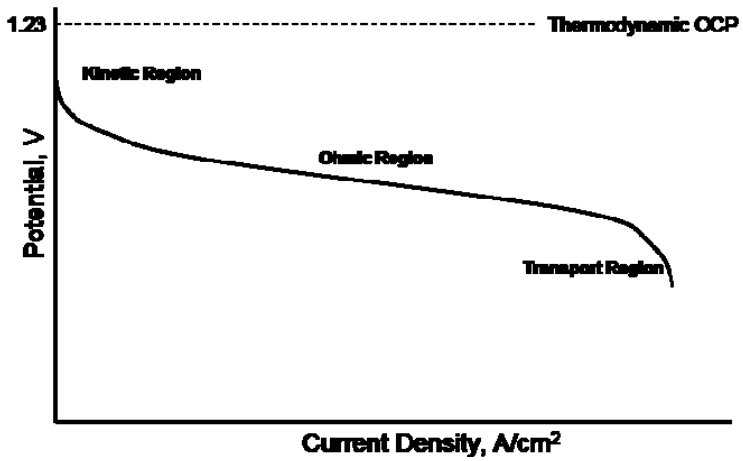

Figure 1.2: Example of a hydrogen/oxygen fuel cell polarization curve which shows the related potential and current density for a given fuel cell. The different limiting processes act at their respective regions.

Deviation in potential from the theoretical OCP is known as overpotential. Overpotential results in a loss of cell performance. There are three fundamental causes of cell overpotential. Each source of overpotential acts as the principle phenomena limiting cell performance at certain current density regimes. At low current densities, kinetic losses are observed due to slow reaction kinetics. At intermediate current densities, the overpotential is a result of electrical resistance of the electrodes and the flow of ions in the electrolyte. At high current densities, the overpotential is due to mass transport limitations within the cell.

The dependence of the reactant concentration/partial pressure on OCP is accounted for in the Nernst equation as shown in Equation 1-4 for the hydrogen fuel cell reactions.

$$E = E^0 + \frac{RT}{2F}\ln\left(\frac{a_{H_2}.a_{O_2}^{1/2}}{a_{H_2O}}\right) \qquad \textbf{(1-3)}$$

The most active catalysts developed have been platinum and platinum alloys. For anodic hydrogen oxidation and cathodic oxygen reduction, the standard electrocatalysts are carbon-supported platinum materials [1]. The support morphology is an important consideration in achieving high platinum dispersion, controlled particle size and long-term stability. The metal nanoparticle support needs to have a high surface area and be electrically conductive.

1.1.2 Alkaline Fuel Cell (AFC)

In comparison to a PEMFC, the same overall reaction occurs in an alkaline fuel cell (AFC); the major difference is the specific anodic and cathodic reactions which occur. In the AFC, hydroxyl ions (OH-) are the mobile species transported through the electrolyte membrane, instead of protons (H^+) as in the PEMFC. The basic anodic and cathodic reactions as well as the overall cell reaction are shown in Equation 1-4.

$$\begin{aligned} &ANODE: H_2 + 2OH^- \longrightarrow 2H_2O + 2e^- \\ &CATHODE: O_2 + 2H_2O + 4e^- \longrightarrow 4OH^- \\ &OVERALL: H_2 + \frac{1}{2}O_2 \longrightarrow 2H_2O \end{aligned} \qquad \textbf{(1-4)}$$

The hydroxyl species react with hydrogen at the anode to release electrons and energy, along with forming water. Water management becomes an issue at the anode instead of at the cathode, as in the PEMFC. New hydroxyl ions are formed at the cathode during the reaction of oxygen and water. The important fundamental advantage of the AFC is the anodic and cathodic kinetic or activation overpotential is less than in acid media.

Historically, the research and development of AFCs was at its peak during the 1960s and early 1970s following the success of the Apollo space program; it was the AFC that enabled the expedition of man to the moon. The decline of AFC research and development is mainly the result of two factors. First is the advantage of PEMFC technology due to the development of robust and highly conductive acidic proton exchange membranes, notably Nafion® (DuPont). This enables the completely solid-phase membrane electrode assembly (MEA) without the need of liquid electrolyte wherein the ionomer can be cast in the catalyst layer ink, increasing the reaction interface. The second major obstacle for AFC development has been the reaction between carbon dioxide and the alkaline electrolyte. The common alkaline electrolyte used in AFCs has been aqueous potassium hydroxide due to its low cost and high solubility. The carbon dioxide in air reacts with the potassium hydroxide electrolyte forming potassium carbonate as in Equation 1-5.

$$2KOH + CO_2 \longrightarrow K_2CO_3 + H_2O \qquad \textbf{(1-5)}$$

This reaction presents a problem of long-term stability for a liquid electrolyte AFC. The potassium carbonate salt is less soluble and precipitates, thus blocking pores in the electrodes. Mass transport losses increase due to an increase in viscosity consequently reducing diffusion rates. Ohmic losses increase due to a decrease in electrolyte conductivity. In addition, kinetic losses magnify; the anodic reaction rate decreases due to decreased OH^- concentration and the cathodic reaction rate decreases due to decreased oxygen solubility.

1.1.3 Direct Methanol Fuel Cell (DMFC)

Fuel cell operation using methanol instead of hydrogen as the fuel eliminates the problem of hydrogen storage or reforming. Currently, it is believed that direct methanol fuel cells (DMFCs) could be used in portable electronic equipment due to a higher energy density than batteries and faster recharging. Two major challenges exist in the development of DMFCs. The first is the inefficient anode reaction for the oxidation of methanol and the second is the crossover of methanol through the electrolyte membrane to the cathode. The anodic, cathodic and overall reactions for a DMFC are represented in Equation 1-6 which correspond to a theoretical OCP of 1.213 V.

$$\begin{aligned} &ANODE: CH_3OH + H_2O \rightarrow CO_2 + 6H^+ + 6e^- \\ &CATHODE: \frac{3}{2}O_2 + 6H^+ + 6e^- \rightarrow 3H_2O \\ &OVERALL: CH_3OH + \frac{3}{2}O_2 \rightarrow 2H_2O + CO_2 \end{aligned} \qquad \textbf{(1-6)}$$

Unsupported platinum-ruthenium blacks are commonly used as methanol oxidation electrocatalysts employed in Direct Methanol Fuel Cells (DMFCs) [2, 3]. Pure platinum is heavily poisoned by adsorbed carbon monoxide (CO_{ads}) in the anodic methanol oxidation reaction. Platinum alloyed with ruthenium has shown the greatest activity for this reaction due to the facility for CO_{ads} removal. As a result, extensive studies have been undertaken to examine the properties and mechanisms of Pt-Ru alloys. The anodic catalyst loading tends to be much higher in methanol fueled cells (~2

mg/cm^2) in comparison to hydrogen fueled cells (~0.2 mg/cm^2) for various reasons. A higher loading reduces the problem of fuel crossover and the activation losses are reduced to reasonable levels. Noble metal utilization in these catalysts is traditionally low in comparison to anode catalysts used in hydrogen/air fuel cells.

A major factor in the design of an efficient DMFC anode is the removal of product carbon dioxide. The free area for flow of the reactant methanol solution to the catalyst surface is reduced by the continuous evolution of product carbon dioxide. For exactly this reason, the gas diffusion layer is treated with Teflon to promote gas movement from the catalytic layer. The mass transport characteristics at the cathode are quite different than those at the anode side. At the cathode, the air flow becomes saturated with product water and flooding can occur at high current densities. However, the problem of cathodic flooding in the DMFC has not shown to limit cell performance in the typical DMFC operating current densities [4].

1.1.4 Direct Ethanol Fuel Cell (DEFC)

Recently, there has been increased interest in the development of direct ethanol fuel cells (DEFCs). Ethanol is a renewable resource as it can be produced directly by fermentation of biomass. In addition, building a support infrastructure would be far easier than for other fuels. For example, ethanol is already widely distributed as a fuel for conventional internal combustion engines in Brazil. Ethanol also possesses a relatively high energy density as shown in Table 1.1. Overall energy density is calculated from the Gibbs energy change for the overall reaction.

Fuel	Energy Density (kWh/kg)
H_2	32.8
H_2 (Tank Storage ~1.5 wt%)	0.42
Methanol	6.1
Ethanol	8.1

Table 1.1: Energy density comparison of possible fuels including hydrogen, methanol and ethanol. (From [5]).

The anodic, cathodic and overall reactions for a DEFC are shown in Equation 1-7 which correspond to a theoretical OCP of 1.145 V.

$$\begin{aligned} &ANODE: C_2H_5OH + 3H_2O \rightarrow 2CO_2 + 12H^+ + 12e^- \\ &CATHODE: 3O_2 + 12H^+ + 12e^- \rightarrow 6H_2O \\ &OVERALL: C_2H_5OH + 3H_2O + 3O_2 \rightarrow 2CO_2 + 6H_2O \end{aligned} \quad \textbf{(1-7)}$$

The key problem is creating enhanced materials for the anodic reaction. The electro-oxidation of ethanol is extremely complicated and the development of efficient anode electrocatalysts presents a difficult challenge. For ethanol electro-oxidation, platinum-based alloys have shown the greatest activity. These alloys include Pt-Ru, Pt-Sn as well as a variety of other metallic alloys and oxides [6, 7]. A comparison of the high anodic overvoltages that exist for different anode catalysts in the DEFC are depicted in Figure 1.3.

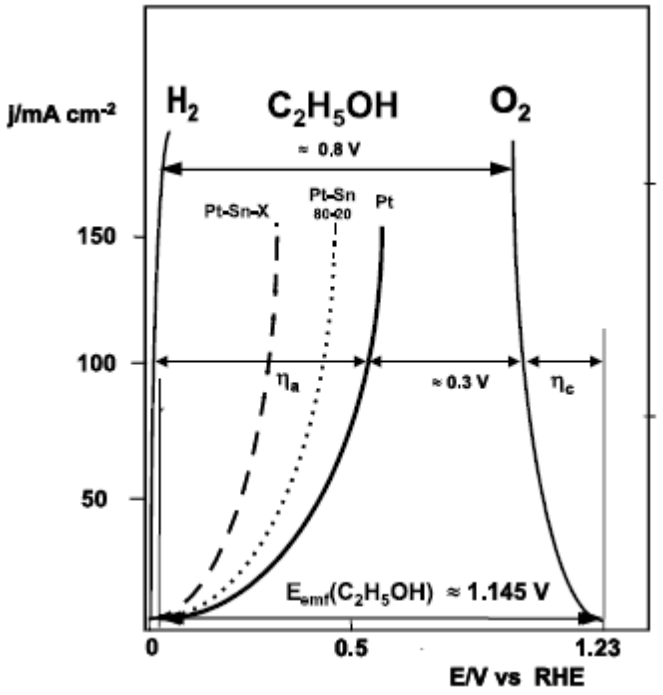

Figure 1.3: Current vs. Voltage curves for ethanol/oxygen fuel cell with different platinum-based anode catalysts compared to that of a hydrogen/oxygen fuel cell with platinum catalysts. (From [5]).

As shown in Figure 1.3, for a pure platinum anode catalyst, the anodic overpotential (η_a) of ethanol electro-oxidation is ~0.6 V at 100 mA/cm^2. Use of a Pt-Sn alloy can reduce this overpotential by ~0.1 V. In addition, a tri-metallic catalyst like Pt-Sn-Ru reduces the overpotential by ~0.3 V. Research continues into determination of an effective anode catalyst. In comparison to methanol oxidation, there is a need to tune the catalyst to break the C-C bond effectively for the oxidation of ethanol. It is promotion of this bond breakage that is essential in developing anode catalysts for DEFCs.

1.1.5 Alkaline DEFC

It has been found that ethanol undergoes significantly more complete oxidation to CO_2 in an alkaline fuel cell compared to a PEMFC. One study estimated that

approximately 50% more current from complete CO_2 formation was collected in an alkaline fuel cell than in a comparable acid fuel cell[8]. Although this suggests higher C-C bond scission rates, the mechanism of ethanol oxidation in alkaline media is still ill-defined. This is especially difficult to investigate because product CO_2 forms potassium carbonate in the presence of aqueous alkaline electrolyte.

1.2 Tafel Equation for Electrochemical Reaction

In Section 1.1.1, the concept of overpotential was introduced as the deviation in potential from the theoretical OCP or rest potential (E_r). At low current densities, kinetic overpotential or "electron transfer overpotential" dominates and is associated with the limiting rate of electron transfer across the boundary between the ionic and electronic conductors. This electron transfer rate is dependent upon the species participating in the reaction, properties of the electrolytic phase and the character of the electrode (like the chemical nature of the metal). Considering a reaction wherein A+B → products, activated complex theory states the reaction will proceed through an activated complex (AB)*. The activated complex is assumed to be in equilibrium with the reactants and can also decompose into products. The Gibbs free energy difference between the reactant and the activated complex can be represented as ΔG_f^* and the forward reaction rate constant k_f and the forward reaction rate v can be expressed in Equation 1-8 and 1-9, respectively.

$$k_f = k_f^0 \exp\left(\frac{-\Delta G_f^*}{RT}\right) \quad \textbf{(1-8)}$$

$$v = k_f^0 c_A c_B \exp\left(\frac{-\Delta G_f^*}{RT}\right) \quad \textbf{(1-9)}$$

It is evident from Equation 1-9, that a change in ΔG_f^* will have an effect on the overall reaction rate. A change in applied potential E will affect ΔG_f^* and thus the reaction rate. This effect is illustrated in Figure 1.4 which shows the change in energy of a redox system as a function of reactant coordinate for two different potentials E_1 and E_2.

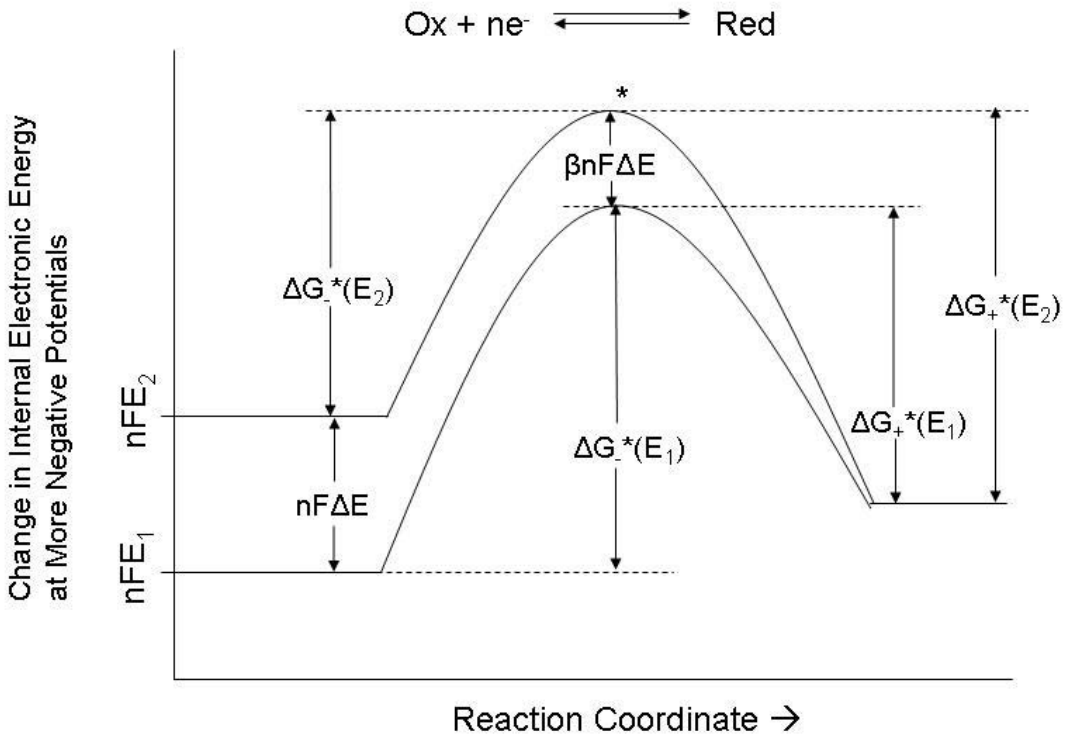

Figure 1.4: Internal energy diagram of electron during transition from electrode to redox species comparing two potentials ($E_2 < E_1$) (Adapted from [9].)

In Figure 1.4, the free energy of Ox + ne^- is on the left side of the diagram and the free energy of the reduced species (Red) is on the right side. The total free energy change due

to a change in potential is equal in magnitude to nFΔE. However, only a fraction β of the total free energy change appears for the activated complex. The change in free energy due to a change in potential for the cathodic and anodic reactions is expressed in Equations 1-10 and 1-11 respectively.

$$\Delta G_{-}^{*}(E_2) = \Delta G_{-}^{*}(E_1) + (1-\beta)nF\Delta E \quad \textbf{(1-10)}$$

$$\Delta G_{+}^{*}(E_2) = \Delta G_{+}^{*}(E_1) - \beta nF\Delta E \quad \textbf{(1-11)}$$

The asymmetry parameter β expresses how symmetric the free energy potential curve is with respect to reactants and products. Incorporating Equations 1-9, 1-10 and 1-11, choosing the E_1 as the zero of the reference electrode and replacing E_2 and ΔE by an arbitrary potential E leads to the rate of the cathodic (Equation 1-12) and anodic (Equation 1-13) reaction.

$$i^{-}(E) = -nFc_{Ox}k^{0}\exp\left(-\frac{(1-\beta)nFE}{RT}\right) \quad \textbf{(1-12)}$$

$$i^{+}(E) = nFc_{\mathrm{Re}d}k^{0}\exp\left(\frac{\beta nFE}{RT}\right) \quad \textbf{(1-13)}$$

These equations express two partial current densities of opposite algebraic sign. At the rest potential ($E = E_r$), the net current is zero and the two partial currents are equal in magnitude. This value is known as the exchange current density (i_0) and corresponds to a dynamic equilibrium. The exchange current density (i_0) depends on the concentration of electroactive species and the free energy of reaction at the rest potential. In addition, the

exchange current density (i_0) is increased when a reaction is catalyzed. At the rest potential ($E = E_r$), Equations 1-12 and 1-13 can be equated and after rearrangement the result in the Nernst equation similar to Equation 1-3. If the electrode potential E is substituted by $E_r + \eta$, where η is the overpotential, and incorporating the definition of i_0 the result is the well-known Butler-Volmer equation shown in Equation 1-14.

$$i = i^- + i^+ = i_0\left[\exp\left(-\frac{\beta nF\eta}{RT}\right) - \exp\left(-\frac{(1-\beta)nF\eta}{RT}\right)\right] \quad \textbf{(1-14)}$$

The Butler-Volmer equation is the net algebraic sum of the anodic and cathodic currents which relates the overall current density to the overpotential or deviation from the rest potential.

The Tafel equation follows by manipulation of the anodic and cathodic current densities by solving for η and taking the logarithms to the base 10. The Tafel equation describes the anode and cathode separately and assumes that the reverse reaction rate is negligible in comparison to the forward reaction rate. The Tafel equations for the cathodic and anodic branches are shown in Equation 1-15 and 1-16, respectively.

$$\log_{10} i = \log_{10} i_0 + \left(\frac{(1-\beta)nF}{2.3RT}\right)\cdot\eta \quad \textbf{(1-15)}$$

$$\log_{10} i = \log_{10} i_0 + \left(\frac{\beta nF}{2.3RT}\right)\cdot\eta \quad \textbf{(1-16)}$$

The exchange current density (i_0) can be determined from the intercept in a plot of $\log_{10} i$ vs. η provided that the cell is operating in a purely kinetically-limited regime as illustrated in Figure 1.5.

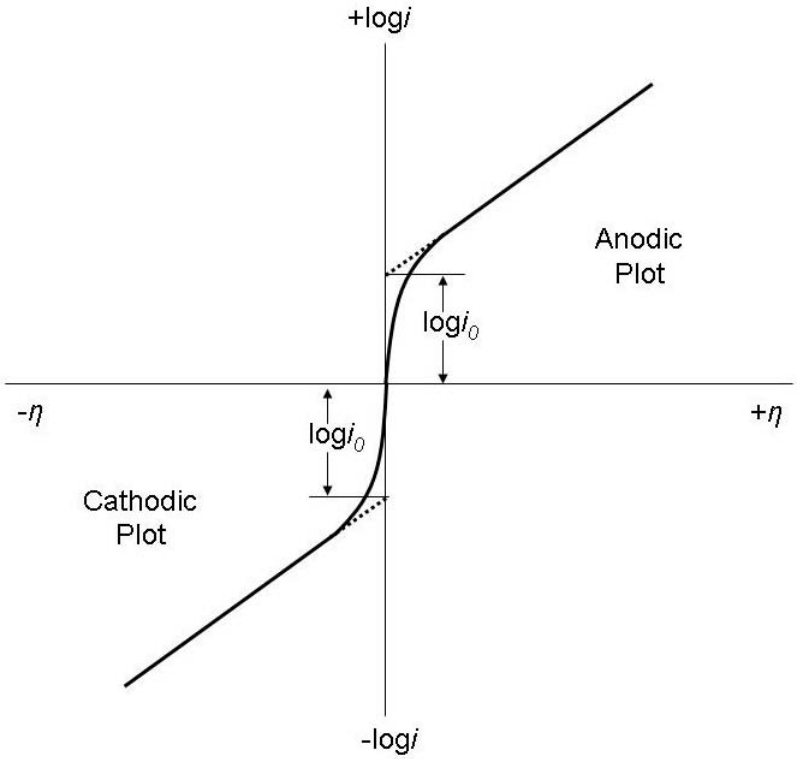

Figure 1.5: Graphical representation of the Tafel equation where current is plotted on a logarithmic scale vs. overpotential η and $\beta = 0.5$.

Given the same concentration of electroactive species, the relative exchange current densities (i_0) between two catalysts demonstrates their relative electrocatalytic activities. A larger relative exchange current density denotes a more active catalyst.

1.3 Fuel Cell Active Layer

1.3.1 Significant Properties Across Length Scales

The nature of the kinetic and transport properties of an electrocatalyst and its integration in the fuel cell is due in part to the hierarchical structure which combines distinct structural considerations across length-scales. On the scale of 1-10 nm, the key factors affecting activity include the crystallite size and identity of the exposed crystallite faces of the catalyst. On the scale of 10-100 nm the topography of the catalyst microstructure and/or catalyst support are the significant elements. At this level, the transport channel for reactants and products is a direct consequence of the local structure. The local roughness at this level is associated with the surface area as well as the effective diffusivity of reactants and thus greatly influences the catalytic activity.

On the scale of 1-100 microns, the key features are of the catalyst aggregates. The larger gas diffusion channels are a consequence of the agglomerated catalytic structure at this level. On the scale of 0.1 - 1 mm, the characteristic layer gradations of the fuel cell are apparent, namely the gas diffusion, catalytic and electrolytic membrane layers. Finally, on the scale of 1 - 10 mm, the fuel cell design and production irregularities become important.

1.3.2 Effectiveness Factor through Modeling

Many models have been created of the fuel cell active layer to gain a greater understanding of the transport and kinetic characteristics. A particularly notable model which attempts to model the active layer at the microscopic level has been developed [10,

11]. This model confirms the generally accepted observation that higher porosity in the fuel cell active layer will result in higher efficiency. The models as well as experimental data shows that diffusion limits catalyst utilization for both the anodic and cathodic reactions [12]. In addition, the models show the existence of local diffusion limitations at the particle level [11].

The governing equations of the active layer are the Tafel equation (Equation 1-17), Fick's Law (Equation 1-18) and Ohm's Law (Equation 1-19) which describe electrochemical reaction, diffusion of reactant gas and ionic conduction, respectively.

$$i = i_0 \exp\left(\frac{2.3\eta}{b}\right)\frac{C}{C_0} \tag{1-17}$$

$$N = -D\left|grad(C)\right| \tag{1-18}$$

$$i_{ionic} = -\sigma\left|grad(V)\right| \tag{1-19}$$

A mass balance can be performed over the control volume consisting of the active layer which is given by Equation 1-20.

$$D\frac{\partial^2 C}{\partial z^2} - \frac{\gamma_l i_0}{nFl}\left[\exp\left(\frac{2.3|\eta|}{b}\right)\frac{C}{C_0}\right] = 0 \tag{1-20}$$

Upon non-dimensionalization of the mass balance equation for a porous catalytic layer, a dimensionless parameter U is determined and is expressed in Equation 1-21. The

mass transfer resistance parameter U is similar to a Damköhler number which demonstrates the influence of diffusion mass transport compared to kinetics.

$$U = \frac{\gamma_l k l}{D C_0} \quad where \quad k(n_i) = \text{kinetic rate constant} = \frac{i_0}{nF} \exp\left(\frac{2.3\eta_i}{b}\right) \tag{1-21}$$

A local roughness factor γ_l accounts for the geometry of the catalytic layer and the catalyst agglomerate width is given by l. The local roughness factor γ_l in the above equations is estimated in this model using the following relationship in Equation 1-22 where L is defined as the active layer thickness.

$$\frac{\text{Total Active Surface}}{\text{Agglomerate Volume}} = \frac{\gamma}{(L - \Theta)} = \frac{\gamma_l}{2l} \quad \text{where } \Theta = \text{Porosity} \tag{1-22}$$

The mass transfer parameter U is similar to the Thiele Modulus ε which compares the characteristic rate of reaction to the characteristic rate of diffusion and thus can be used to calculate the effectiveness factor by Equation 1-23.

$$\varepsilon = \frac{\tanh\sqrt{U}}{\sqrt{U}} \tag{1-23}$$

This effectiveness factor ε for a fuel cell active layer is similar to the effectiveness factor for porous catalyst particles in heterogeneous catalysis. The effectiveness factor characterizes electrocatalyst utilization by comparison of current density with mass

transport limitations to purely kinetic current density. The effectiveness factor for the catalytic layer is dependent upon an electrochemical Thiele Modulus which is in turn dependent upon factors describing the local morphology of the catalyst layer. The models indicate the importance of local catalyst morphology although experimental data is lacking.

1.4 Economic Factors

Commercialization of polymer electrolyte membrane (PEM) fuel cells and direct methanol fuel cells (DMFC) is constrained due in part to the high cost of the catalytic materials required to transform chemical energy into electrical energy. Platinum and platinum-based alloys are the most effective catalysts for both anodic and cathodic reactions. Historically, the cost of platinum has steadily increased and any indication of stabilization has been absent as depicted in Figure 1.6. Much research is directed towards increasing precious metal utilization and efficiency in fuel cell systems.

Figure 1.6: Historical market value of platinum in US$/ounce from January 1992-May 2008. (From [13]).

The amount of platinum required for each PEMFC electrode is around 0.2 mg Pt/cm^2 but this amount is significantly higher (~8 mg/cm^2) for a DMFC anode. Current DMFC literature estimates a power delivery of 60 mW/cm^2 which translates to a 200 mW/cm^3 power density. At the current platinum price, this becomes ca. $20 catalyst per Watt which is extremely expensive. The catalyst utilization is known to be much smaller in methanol/oxygen fuel cells compared to hydrogen/oxygen fuel cells and this issue must be addressed if direct alcohol fuel cells with platinum-based catalysts are to become viable power sources.

2 LITERATURE REVIEW

2.1 Spray Pyrolysis

2.1.1 Mesoporous Silica

Since 1992 when the first surfactant-templated porous silica materials were synthesized by researchers at the Mobil Corporation [14, 15], a plethora of surfactant templates and synthesis routes have been explored by researchers around the world. The surfactant acts as the structure-directing agent wherein silica-surfactant self-assembly occurs based on the relative concentration and variety of surfactant. Calcination removes the surfactant phase resulting in a mesostructured silica material. One material that is of particular interest is SBA-15 which was developed at UC Santa Barbara [16, 17] in 1998. This material consists of a hexagonal array of straight pores around 6-7 nm, interconnected by smaller pores around 1 nm in size.

Aerosol-assisted self-assembly can be used to produce a variety of well-ordered spherical silica particles possessing stable pore structures of hexagonal and cubic form[18]. The surfactant concentration determines the type of mesophase (hexagonal, cubic, lamellar) and the choice of surfactant can determine the pore size. The process of aerosol-assisted self assembly of mesostructured spherical silica particles has been extensively studied. First, a solution of surfactant and silica precursor (usually Tetraethylorthosilicate) is formulated. Ordered mesoporous silica is then synthesized in an aerosol reactor similar to the device shown in Figure 2.1.

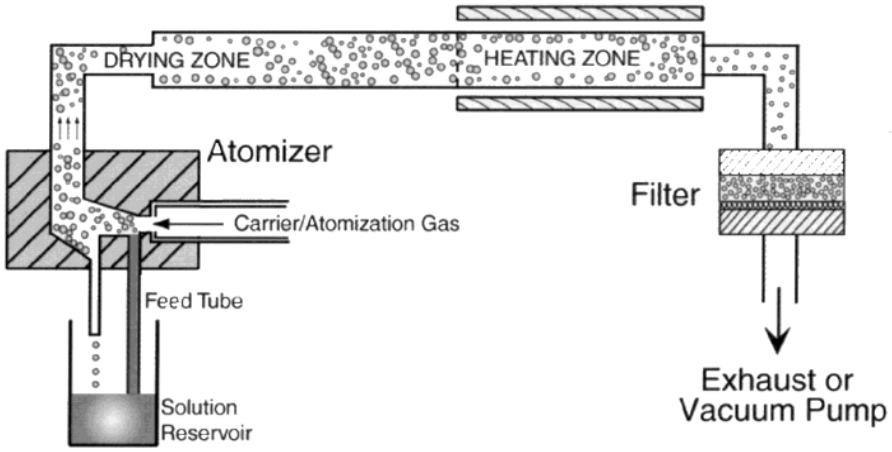

Figure 2.1: Aerosol reactor in which a precursor solution is aerosolized, undergoes a controlled temperature conversion. The final material is collected by a filter. (From [18]).

The surfactant/silica precursor solution is added to the solution reservoir. The solution is ultrasonically vaporized by a commercially-sold humidifier that acts as the atomizer, creating spherical particles around 2 μm. Nitrogen is usually used as the carrier gas to transport the aerosol droplets through the system. The aerosol reactor temperature can be easily adjusted depending on the experiment. Particles are collected on a filter locked in between two metal disks. The disks are wrapped with a heating coil to ensure complete drying of the final powder. Once the powder is dry, it can be collected and is then calcined to remove the surfactant, resulting in spherical mesoporous silica particles.

2.2 Electrocatalyst Design and Synthesis

2.2.1 Conventional Electrocatalysts

The bulk method of electrocatalyst synthesis is by metallic impregnation or co-precipitation wherein an aqueous solution of the metallic precursor is contacted with the support substrate. After evaporation of the water, the metallic phase can be reduced

under hydrogen flow for experimental use. The standard industrial method of producing fuel cell electrocatalysts is by adding a reducing agent, usually formaldehyde or formic acid, to an aqueous mixture of ionic metallic precursors which results in precipitation of the metallic catalyst.

2.2.2 Nanostructured Electrocatalysts

One approach to the synthesis of nanostructured materials has centered on the replication of nanostructured silica templates followed by template removal. Many studies have focused on the synthesis of nanostructured carbon supports for electrocatalyst supports. Mesoporous carbon materials have been synthesized from several mesoporous silica materials [19, 20]. It has been found that SBA-15 is the best template due to its interconnecting micropores between larger mesopores. Silica-templated mesoporous carbons with large surface areas have also been synthesized between the range of 10 nm to 10 μm, depending on the choice of silica template [21].

Various lengths and shapes of monometallic nanowires, templated by various silica structures, have been reported [22-24]. Bimetallic structures templated by nanostructured silica have also been reported which include Pt-Rh and Pt-Pd nanowires [25]. Previous work on the synthesis of nanostructured Pt-Ru electrocatalysts includes the synthesis of a bimetallic Pt-Ru nanowire network templated by mesoporous silica, specifically SBA-15 [26]. The SBA-15 silica template is synthesized separately and is then immersed in a solution of Pt and Ru precursors. This infiltration procedure has to be repeated numerous times, usually about ten, before full pore infiltration can be accomplished [26]. Following this approach, a significant increase in the electrocatalytic

activity was found when compared to a commercial Pt-Ru black. Impregnation synthesis of a bimetallic network in mesoporous silica presents an interesting material design approach, although it is limited in application due to its complexity, parameter variability and time-consuming synthesis. This technique will also be referred to as the "Bulk" templating approach in the work presented here.

2.3 Electrochemical Oxygen Reduction Reaction (ORR)

The cathodic oxygen reduction reaction (ORR) in PEMFCs can occur by two pathways as shown in

Figure 2.2.

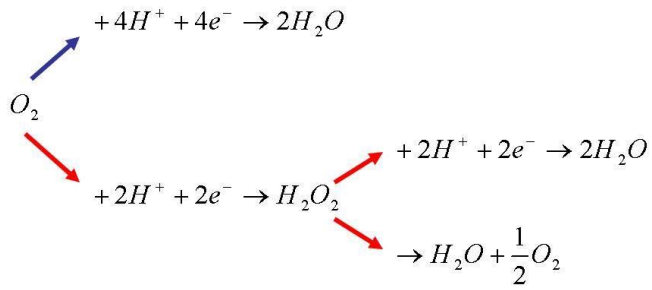

Figure 2.2: Mechanism of oxygen reduction depicting the direct four-electron pathway (blue) and the two-electron pathway (red) forming peroxide which is reduced to water or chemically decomposes.

In the first pathway, oxygen is adsorbed on the catalytic surface and is directly reduced in a four-electron pathway to form water. In the second pathway, the adsorbed oxygen is reduced in a two-electron pathway to generate hydrogen peroxide. The hydrogen peroxide is further reduced to water or chemical decomposes to form water and

oxygen. The desired reaction is the direct four-electron pathway because it results in higher energy conversion avoids degradation of the electrode material.

2.4 Electrochemical Methanol Oxidation Reaction (MOR)

2.4.1 Acid Media

Methanol has been the most extensively studied small organic molecule for direct oxidation in fuel cells. It is evident from Table 1.1, that methanol can provide a relatively high energy density in comparison to hydrogen when considering the issues of storage. In contrast to the hydrogen/oxygen fuel cell, the anodic methanol oxidation reaction (MOR) is the most challenging aspect in the development of DMFCs. The methanol oxidation reaction is the subject of several reviews [27-31] and countless original research papers with the central focus being on the high activity provided by bimetallic Pt-Ru electrocatalysts. The enhancement of the MOR by the addition of Ru to Pt, has been well-known for decades [32, 33] and the explanation for this phenomena is generally understood to be due to a bi-functional mechanism. Ongoing research exists exploring the character and yields of MOR intermediates [34-36] as well as atomic-level details of the MOR usually by studying model single-crystal catalysts [30, 37-39]. The complete MOR mechanism by Pt and Pt-Ru electrocatalysts is complicated because it consists of several possible parallel and series pathways; as such, it is the subject of ongoing mechanistic studies [31, 35, 40-42]. For the purposes of this work, however, these pathways can be simplified as in the representation in Figure 2.3.

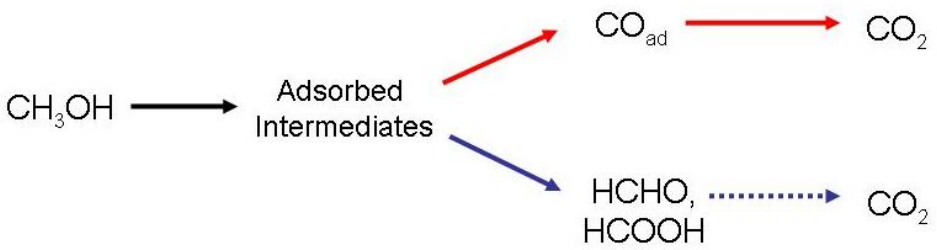

Figure 2.3: Schematic mechanism of methanol electro-oxidation by platinum-based electrocatalysts.

It is challenging to accurately quantify all of the reaction products although several methods have been researched. Infrared spectroscopy is limited as the hydrated formaldehyde species is undetectable and formic acid produces weak bands[36]. Liquid chromatography presents a practical technique and has been successfully used to measure the soluble formaldehyde and formic acid products[35, 42]. Comparisons of the product distributions in varied electrolytes have indicated that the MOR is hindered by strong anion adsorption (e.g. SO_4^{2-} from sulfuric acid electrolyte) by inhibiting the dissociative steps where CO_{ad} is formed.

In addition to an electronic effect wherein Ru donates electrons to Pt reducing the bond strength of Pt adsorbates [43-45], a bi-functional mechanism is considered to be responsible for the enhancement of the MOR by the addition of Ru to Pt [32, 46-49]. It is well-known that Pt is required to catalyze the methanol dehydrogenation reaction and that the resulting intermediates heavily poison a Pt surface [31, 50]. Ru atoms are responsible for adsorption of oxygen-containing species at lower potentials than for Pt. This oxygen-containing species is in turn responsible for oxidation of adsorbed intermediates, like CO_{ad} present on Pt sites. This bi-functional mechanism is expressed in a simplified manner by Equation 2-1.

$$CH_3OH \xrightarrow{Pt} CO_{ad} + 4H^+ + 4e^- \xrightarrow{Ru,H_2O} CO_2 + 2H^+ + 2e^- \quad \textbf{(2-1)}$$

In regards to the optimal Pt:Ru composition, several studies which have included model electrocatalysts as well as high-surface area electrocatalysts have found the optimal composition to be around 50 at.% Ru [37, 51-54]. A plot of current density vs. Ru composition for Pt-Ru model catalysts from several different studies is shown in Figure 2.4.

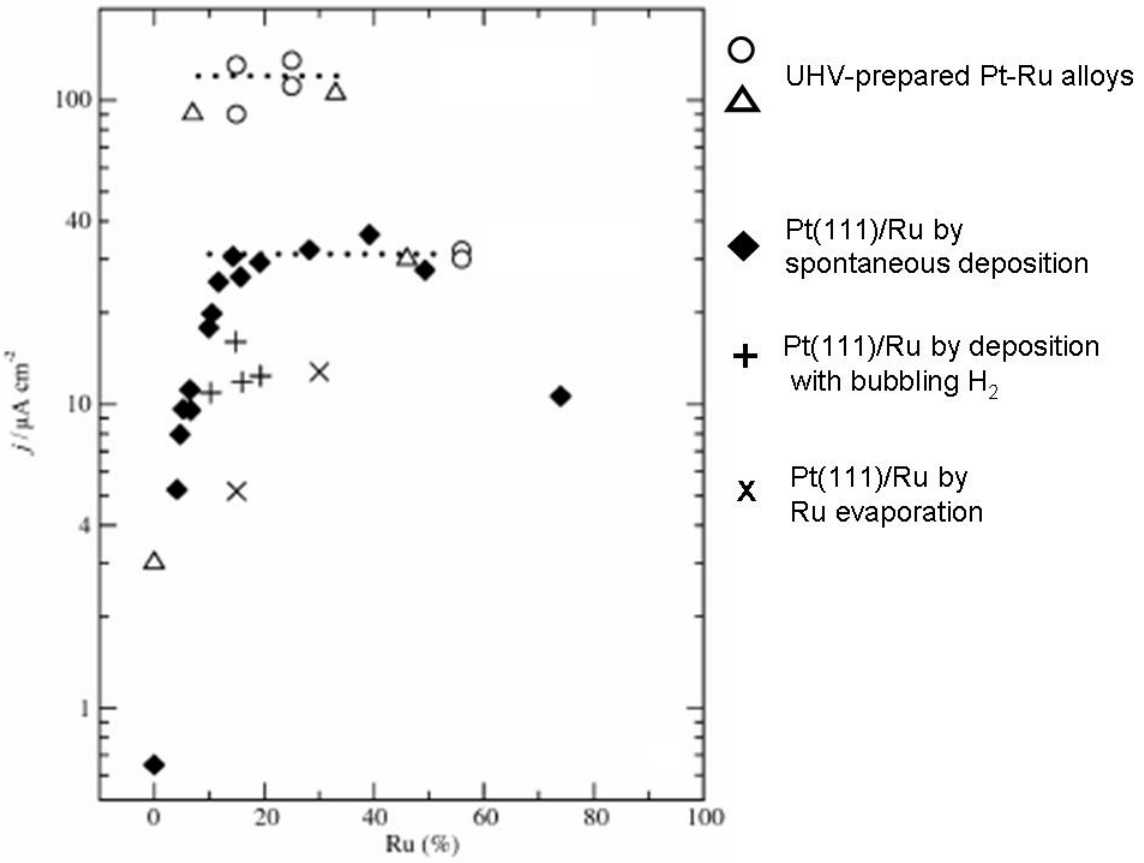

Figure 2.4: Activity towards methanol electro-oxidation as a function of Ru percentage at the surface. (Adapted from Ref. [37])

From the plot in Figure 2.4, the optimal composition has been shown to lie in the range from 20-60% Ru. However, a composition on the higher end of that range is generally accepted to be ideal for long-term operation of the catalyst. In the case of unsupported Pt-Ru electrocatalysts, two major factors have been shown to enhance MOR activity. The first is a maximum catalyst surface area and the second is a maximum number of metal alloy sites with composition close to 1:1 [51]. A high overall degree of alloying, ideally in a 1:1 Pt:Ru atomic ratio is considered advantageous.

2.4.2 Alkaline Media

The mechanism of the methanol oxidation reaction (MOR) in alkaline media on Pt-based anodes is the subject of ongoing research and debate. In-situ spectroscopic studies have detected formate (Equation 2-2) and carbonate (Equation 2-3) as products, both of which are formed through several adsorbed intermediates [40, 55-57].

$$CH_3OH + 5OH^- \rightarrow HCOO^- + 4H_2O + 4e^- \quad \textbf{(2-2)}$$

$$CH_3OH + 8OH^- \rightarrow CO_3^{2-} + 6H_2O + 6e^- \quad \textbf{(2-3)}$$

The formation of carbonate (Equation 2-3) is known to proceed in part through an adsorbed CO intermediate expressed in Equation 2-4 and then further oxidized to carbon dioxide as expressed in Equation 2-5. In alkaline environment, OH^- anion discharge results in oxygen containing species (represented by OH_{ad} in Equation 2-6) and carbon dioxide is rapidly converted to carbonate as in Equation 2-7.

$$CH_3OH + 4OH^- \rightarrow CO_{ad} + 4H_2O + 4e^- \quad \textbf{(2-4)}$$

$$CO_{ad} + 2OH_{ad} \rightarrow CO_2 + H_2O \quad \textbf{(2-5)}$$

$$OH^- \rightarrow OH_{ad} + e^- \quad \textbf{(2-6)}$$

$$CO_2 + 2OH^- \rightarrow CO_3^{2-} + H_2O \quad \textbf{(2-7)}$$

Reports have suggested that the reaction of adsorbed CO and adsorbed OH, as expressed in Equation 2-5, is the rate limiting step for the MOR in alkali [55, 58, 59]. Significant CO coverage on Pt electrodes has been observed during methanol oxidation from in-situ IR spectroscopic measurements [40, 59-61]. Interestingly, the CO coverage observed from the IR spectroscopic measurements is lower than expected, leading some to conclude that adsorbed CO is not the primary poisoning species, but instead some other adsorbed species like HCO [60, 62]. The exact form of the main poisoning species is controversial; some explain the low amount of CO_{ad} observed from IR spectroscopic measurements by a low steady-state CO coverage and a multi-fold adsorption site instead of the atop position which is more easily observed by IR spectroscopic measurements [55].

The primary final product of the MOR in alkali is the subject of some controversy. A variety of the relative amounts of final products have been reported, some suggesting carbonate, others formate as the main product [40, 57]. The assorted experimental descriptions are likely compatible considering the range of Pt surface structures and potential ranges studied. Generally at low potentials, carbonate is the primary product and at higher potentials, parallel pathways occur, often leading to a prevalence of

formate. In regard to surface structure, formate is produced at much lower potentials on polycrystalline platinum than on Pt(111).

In acid media, Ru is widely known to effectively promote the MOR. The mechanism of this enhancement has been extensively studied and is described in Section 2.4.1. The effect of Ru has been investigated significantly less in alkaline media and there are practically no studies on the role of Pt:Ru composition. MOR rates on both Pt/C and Pt-Ru/C catalysts have been reported to be higher in alkaline media than in acid media which has in part been attributed to a higher coverage of OH_{ad} at lower potentials in addition to the absence of adsorbing anions from the acidic electrolyte [57, 63]. Additionally, some studies on Pt-Au alloy nanoparticles [64] and non-noble metal (Bi, Cd and Pb) adatoms [58] showed improved MOR activity in alkaline media.

2.5 Electrochemical Ethanol Oxidation Reaction (EOR)

While the electro-oxidation of methanol in acid has a fairly well established mechanism, the electro-oxidation of ethanol is more complex and is the focus of ongoing mechanistic studies. The overall reaction is expressed in Equation 2-8.

$$C_2H_5OH + 3H_2O \longrightarrow 2CO_2 + 12H^+ + 12e^- \quad \textbf{(2-8)}$$

The reaction involves a greater number of electrons exchanged and many adsorbed intermediates and products. Conversely to methanol electro-oxidation, Pt-Sn electrocatalysts have been shown to outperform Pt-Ru electrocatalysts for ethanol electro-

oxidation [65-67]. A comparison of ruthenium, tungsten, palladium and tin addition to platinum for ethanol oxidation in acid media is shown in Figure 2.5.

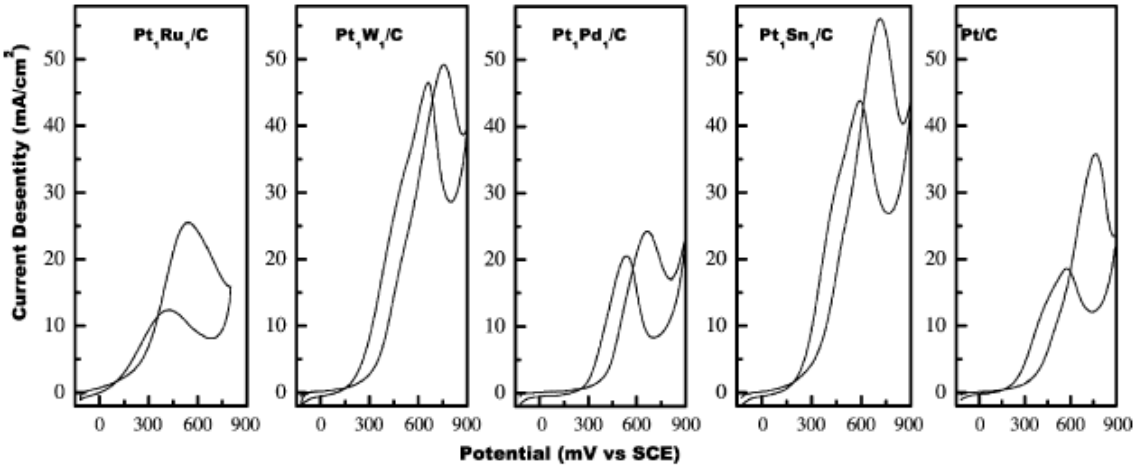

Figure 2.5: Cyclic voltammograms of ethanol oxidation at different anode catalysts in 0.5M H_2SO_4 + 1M Ethanol at 25°C. (From [65].)

It is evident from the cyclic voltammograms in Figure 2.5 that the Pt-Sn catalyst exhibits the highest current density at the oxidation peak. MEA studies of the same Pt-based catalysts in working DEFC configuration have shown the cell incorporating the Pt-Sn anodic catalyst exhibits almost twice the maximum power density compared to the cell incorporating the Pt-Ru electrocatalyst and almost three times that of the Pt-W electrocatalyst [66].

2.5.1 Acid Media

In-situ IR spectroscopic studies have shown that in addition to adsorbed CO, adsorbed acetyl intermediates are also present which can then form acetaldehyde and

acetic acid [68-72]. Two principal routes for the oxidation of ethanol on Pt-Sn catalysts can be proposed as shown in Figure 2.6.

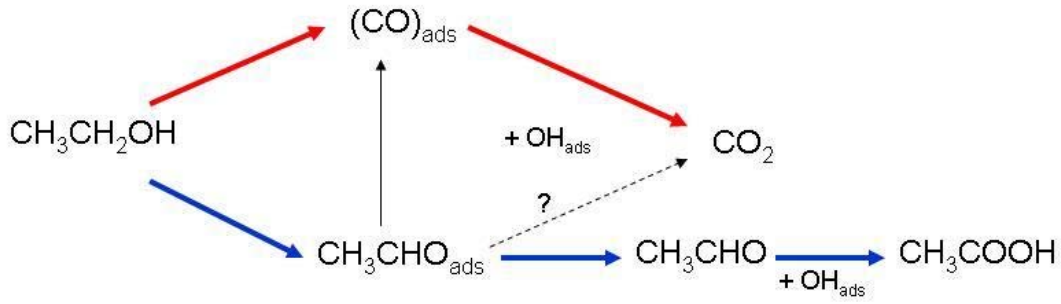

Figure 2.6: Schematic mechanism of ethanol electro-oxidation on a platinum electrode.

The first route, shown in red, involves the formation of adsorbed CO (CO_{ads}). The formation of CO_2 is observed after the disappearance of CO_{ads} which has higher coverages at low potentials. The second route, shown in blue, involves the formation of an adsorbed two-carbon species (CH_3CHO_{ads}) which results in the formation of acetaldehyde and acetic acid which is clearly observed during ethanol oxidation on Pt-Sn electrocatalysts. Particular interest has focused on Pt-Sn alloys due to the low potential at which Sn is partially covered by OH species.

A significant focus of ethanol electro-oxidation research has been on the superior performance of Pt-Sn catalysts in acid media [67, 73-79]. The superior performance is attributed to a bi-functional mechanism wherein tin or tin oxides provide the surface with oxygen species allowing for improved removal of strongly adsorbed species such as CO. Depending on preparation method, the optimal Pt-Sn composition reportedly varies. In general, the optimal composition of Sn ranges from 10-20 atomic % for co-impregnated catalysts [67].

2.5.2 Alkaline Media

The kinetics of both cathodic oxygen reduction and anodic oxidation of organic molecules are much more facile in alkaline media in comparison to acid media which presents a key advantage [8, 57, 63, 74, 80, 81]. In alkaline environment, studies into suitable electrocatalysts for ethanol oxidation are spotty but in general, platinum and palladium based catalysts have been the primary focus. In early work, metal ad-atoms (Pb, Tl, Cd) were shown to improve the activity of ethanol oxidation at a Pt electrode [82]. More recently, studies have investigated the effect of different bimetallic and oxide promoted catalysts. In one particular study, Pt-CeO_2/C composites showed better performance for ethanol oxidation than a comparable Pt/C [83]. The improved performance was suggested to be the result of a greater ability of the Pt-CeO_2/C catalyst to form oxygen-containing species at lower potentials, functioning in a similar way as Ru addition to Pt does. CO-like poisoning species on Pt can be transformed to CO_2 at lower potential as a result of the formation of oxygen-containing species. The addition of ZrO_2 and MgO to Pt has also shown to improve ethanol oxidation performance [84, 85]. Also, Ni-supported Pt-Ru electrocatalysts have been investigated and it was found that an optimal Ru content was in the range of 30-50 at% [86].

In-situ infrared spectroscopic studies have shown the that adsorbed CO is a primary poisoning species and acetate is a primary product for ethanol oxidation by platinum in alkaline media [81]. In addition, it has been found that ethanol undergoes a more complete oxidation to CO_2 in alkaline media than in acid media by the same platinum anode [8].

2.6 Electrochemical Oxidation of Carbon Monoxide (CO)

The importance of investigating the electrochemical oxidation of CO stems from the fact that CO_{ad} has been found to be a primary poisoning species in methanol and ethanol electro-oxidation by platinum. In acid media, it is generally accepted that CO oxidation occurs through a Langmuir-Hinshelwood mechanism between CO_{ad} and an adsorbed oxygen-containing species derived from water [87-93]. In alkaline media, however, there is some debate as to the mechanism of CO oxidation which has been studied on Pt single crystals. Some authors believe a purely Langmuir-Hinshelwood mechanism occurs between CO_{ad} and OH_{ad} [94, 95]. The exact nature of the oxygen-containing species is somewhat controversial, but is generally called OH_{ad}. Alternatively, it has been suggested that at low potential, CO oxidation occurs by an Eley-Rideal reaction between CO_{ad} and OH^- in the outer Helmholtz plane [80, 96]. More recent investigations have proposed that the Eley-Rideal mechanism has been mistaken for a non-competitive Langmuir-Hinshelwood mechanism wherein an OH_{ad} does not compete with CO_{ad} for adsorption sites at low potentials [97].

A CO oxidation study at two temperatures (2°C and 60°C) on Pt single crystals in alkali demonstrated that CO oxidation is an activated process presumably due to enhanced mobility of CO_{ad} and increased activity of oxygenated species at higher temperatures [95]. Therefore, the reaction rate of CO oxidation is likely determined by the surface coverages of OH_{ad} (Equation 2-9) and CO_{ad} (Equation 2-10) and the probability of interaction of these two adsorbed species. The overall reaction mechanism is shown in Equation 2-11.

$$OH^- \rightarrow OH_{ad} + e^- \quad \textbf{(2-9)}$$

$$CO_{bulk} \rightarrow CO_{ad} \quad \textbf{(2-10)}$$

$$CO_{ad} + OH_{ad} + OH^- \rightarrow CO_2 + H_2O + e^- \quad \textbf{(2-11)}$$

Modeling of this type of Langmuir-Hinshelwood reaction mechanism has shown the importance of CO mobility; islands form as a result of poor mixing due to low surface mobility [98]. Additionally, for Pt-Ru catalysts, modeling indicates that the bi-functional mechanism does not operate unless CO is mobile on the surface [49].

3 Problem Statement and Objectives

3.1 Problem Statement

Platinum-based electrocatalysts are currently required for state-of-the-art fuel cells. The precious metal catalyst represents a substantial portion of the overall cost. Therefore, if fuel cell technology is to become competitive with other energy conversion technologies, increasing the precious metal utilization as well as alloying Pt with cheaper metals is absolutely crucial. In 2004, it was reported that a five-fold decrease in platinum loading is needed for mass commercialization of state-of-the-art PEMFCs [99]. The primary objective in the design of precious metal catalysts is to increase utilization. The focus of this work is on creating enhanced nanostructured materials which improve precious-metal utilization. The goal is to engineer superior electrocatalytic materials through the synthesis, development and investigation of novel templated open frame structures in an aerosol-based approach. Previous methods of creating such nanostructured materials, like the bulk template synthesis technique, have shown significant drawbacks. The most striking drawback is the inability to create a structure that is maintained throughout the entire sample.

3.2 Objectives

The main objective of this work is to develop a method for synthesizing nanostructured Pt-Ru electrocatalysts wherein the effects of the structure can be related to electrocatalytic performance. Previously, bulk templating methods were limited due to

the fact that the nanostructure did not permeate throughout the majority of the sample. A central goal is to determine if the aerosol-based templating method can be extended to different materials for other systems, namely Pt-Sn for ethanol oxidation in alkaline media. Finally, the effect of Sn addition to Pt on ethanol oxidation in alkaline media is evaluated in a unique approach incorporating anion-exchange ionomers as entrapment materials for RDE studies.

Catalyst Synthesis

1. Examine bulk templating synthesis routes for Pt/C and Pt-Ru composites and evaluate resulting nanostructure.

2. Develop a synthesis method for nanostructured electrocatalysts wherein the desired structure exists throughout the entirety of the sample.

3. Investigate alternative Pt-Ru aerosol synthesis procedures using diverse precursor solution formulations.

4. Extend synthesis method to other systems, i.e. nanostructured Pt-Sn electrocatalysts for anodic ethanol oxidation.

5. Investigate Pt-Sn composition effects by altering precursor solution formulations.

Catalyst Performance

1. Investigate the effect of Pt-Ru:template aerosol precursor solution formulations on electrocatalytic performance.

2. Identify an effective open-frame structure for Pt-Ru electrocatalysts based on experimental performance data of the integrated materials.

3. Evaluate the electrocatalytic performance of aerosol-derived Pt-Ru electrocatalysts compared to commercially-available catalysts.

4. Examine viability of studying catalytic layer transport effects due to local electrocatalyst morphology in working fuel cell.

5. Investigate Pt-Sn composition effects on electrochemical ethanol oxidation in alkaline media.

6. Examine the effect of Sn addition to Pt by incorporating anion-exchange ionomers in RDE studies tailored to alkaline media.

4 Experimental Methodology

4.1 Synthesis

4.1.1 Bulk Templating

In the bulk method of templating, the mesoporous silica template is first formed separately. This is followed by impregnation of the silica template with an aqueous solution of the metallic precursors. After evaporation under vacuum, the material is reduced under hydrogen flow. Finally, the silica template is removed with a strong base.

4.1.2 Spray Pyrolysis Templating

In the aerosol method of templating, an aqueous solution of the silica template and metallic precursors is ultrasonically atomized. The resulting aerosol droplets are carried through a controlled temperature conversion via an inert gas. The final material is collected on a filter paper. Just as in the bulk method, the material is then reduced under hydrogen flow and the silica template is removed with a strong base. This process is shown in Figure 4.1.

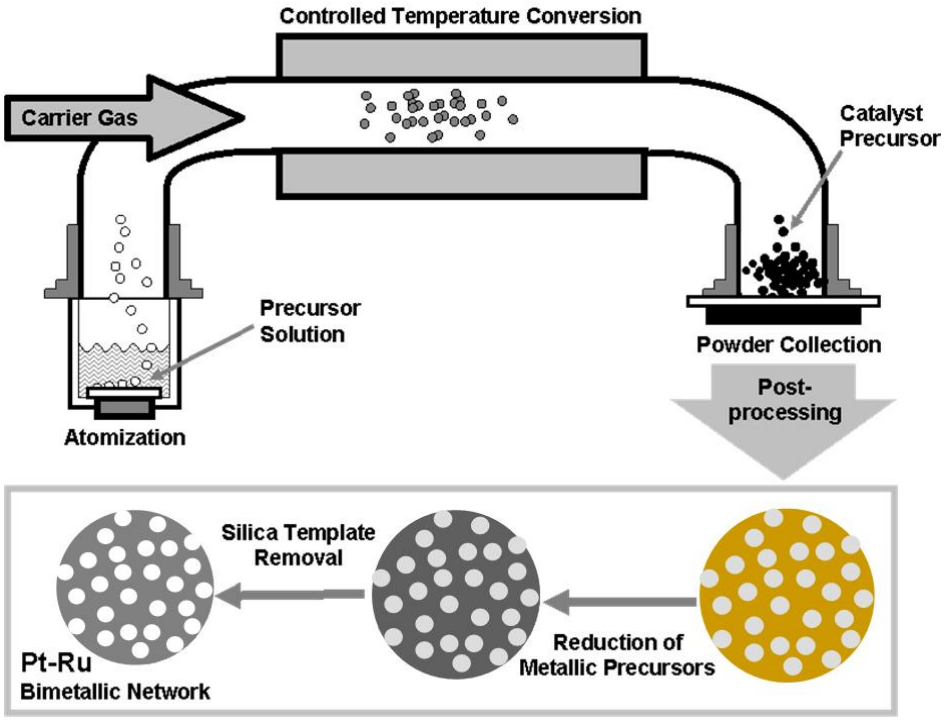

Figure 4.1: Illustration of steps in the synthesis of a Pt-Ru bimetallic network. A solution of precursors is aerosolized and flown through a temperature controlled furnace by means of an inert carrier gas. Upon powder collection, the material is reduced, followed by silica template removal.

There are many advantages of synthesizing templated electrocatalyst materials by spray pyrolysis. The final morphology and composition of the electrocatalyst is determined by the precursor solution atomized. Changing the morphology and composition of the precursor solution is extremely simple and straightforward. For alloys, the template and alloy constituent precursors are in close contact during synthesis which results in a more homogeneous final material as opposed to bulk templating methods.

4.2 Characterization

4.2.1 Transmission Electron Microscopy (TEM)

Transmission electron microscopy (TEM) is an imaging technique wherin a beam of electrons is focused on a particular sample. The electrons are generated by thermionic emission, then accelerated and focused by electric and magnetic fields. The electrons that remain, after encountering the sample, are detected on a fluorescent screen or CCD camera. Thus, areas of the sample where electrons are scattered appear dark on the screen or camera. Visualization of the synthesized electrocatalyst structure is one of the most important methods in this work.

4.2.2 Energy Dispersive Spectroscopy (EDS)

Energy dispersive spectroscopy (EDS) is a chemical characterization technique wherein a beam of electrons is focused on a particular sample; hence it is commonly used in conjunction with TEM analysis. The incident beam will excite an electron in a low energy state which results in the formation of an electron hole in the atom's electronic structure. To compensate, an electron in a higher energy state will fill this hole, releasing a certain amount of energy in the form of an X-ray. These X-rays are collected and arranged by energy and intensity. Each element has a unique electronic structure and accordingly, a unique response to electromagnetic waves. Therefore, the elemental composition of particular sample can be determined from the energy spectrum which is extremely useful for characterizing the composition of synthesized electrocatalysts.

4.2.3 X-Ray Diffraction (XRD)

X-ray diffraction (XRD) is a crystallographic technique in which a beam of X-rays irradiates a particular crystalline sample. Upon interaction with the electrons in the crystal, the X-rays diffract in a pattern dependant on the particular crystal structure of the sample. The X-ray diffraction pattern exhibits peaks in intensity at certain angular positions. The peak height, position and width are used to determine several aspects of the material structure. To characterize synthesized electrocatalysts, XRD can be used to determine the type of lattice, crystallite size and estimate the degree of alloying.

4.2.4 X-Ray Photoelectron Spectroscopy (XPS)

X-ray photoelectron spectroscopy (XPS) is a surface characterization technique wherein a particular sample is irradiated with a beam of X-rays under ultra-high vacuum (UHV) conditions. This results in ejection of electrons from the top 10 nm of the sample. The amount of electrons with a certain kinetic energy is measured, resulting in an XPS spectrum exhibiting peaks in intensity at certain values of the binding energy. Each element produces characteristic peaks corresponding to certain electron configurations. To characterize synthesized electrocatalysts, this technique is extremely useful to determine the surface elemental composition and oxidation states of the material. In conjunction with EDS, the elemental composition can be compared and confirmed.

4.2.5 Rotating Disc Electrode (RDE) Studies

A standard three electrode cell setup is commonly used in research to investigate electrode reactions. It is an electrochemical cell consisting of a working electrode (W), a counter electrode (C) and a reference electrode (R) as shown in Figure 4.2.

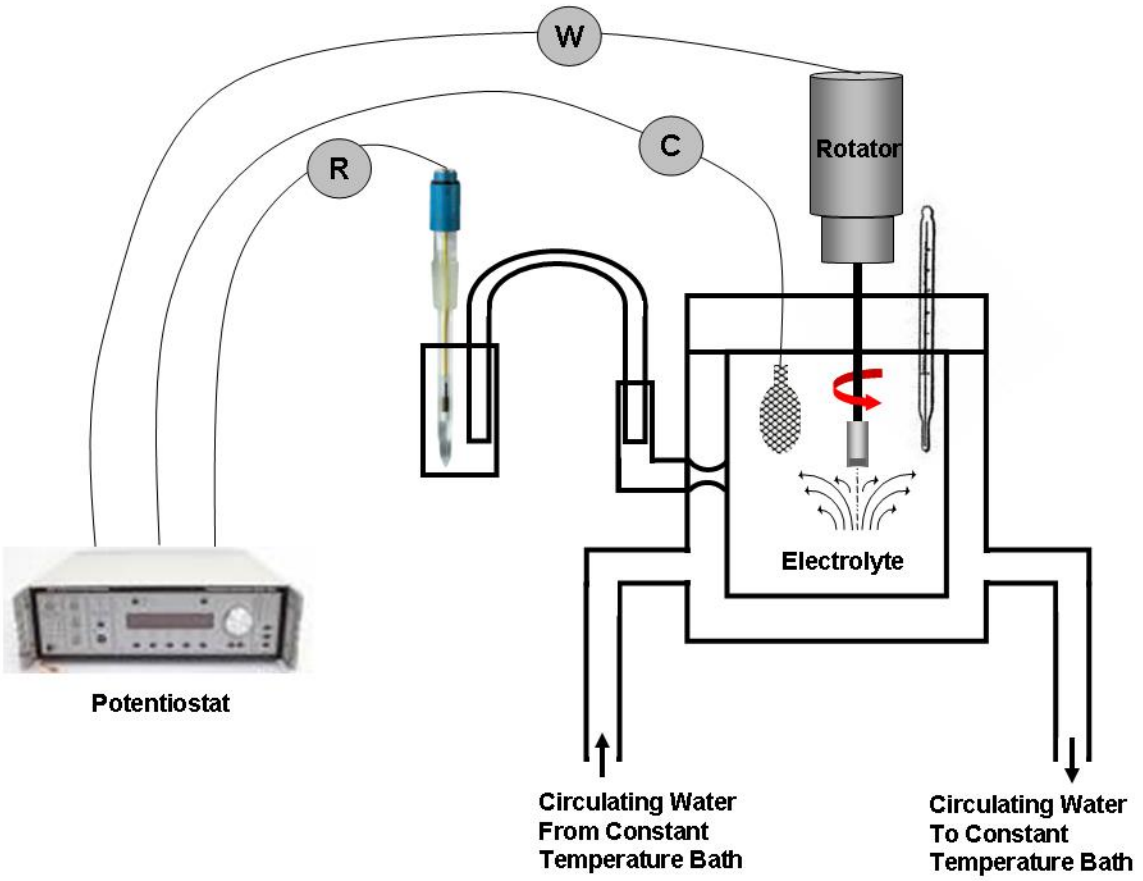

Figure 4.2: Jacketed electrochemical cell setup with working (W), counter (C) and reference (R) electrodes. The jacketed electrochemical cell allows the electrolyte solution to be held at a constant temperature. The reference electrode (R) is situated in separate electrolyte solution at room temperature and connected through an electrolyte bridge.

Current flows between the working and counter electrodes, while the potential of the working electrode is measured against the reference electrode. The working electrode is where the reaction of interest occurs and often consists of a rotating disc electrode

(RDE). A silver-silver chloride (Ag/AgCl) reference electrode is used for experiments in acid media and corresponds to +0.2 V vs reversible hydrogen electrode (RHE) in 0.5M H_2SO_4. Alternatively, a mercury-mercury oxide (Hg/HgO) reference electrode is used in alkaline media and corresponds to +0.92 V vs. RHE in 1M KOH. The measurements here were made using a Pt gauze counter electrode and a Pine Model AFCBP1 potentiostat.

For temperature-dependent experiments, a jacketed electrochemical cell is employed in which temperature-controlled water is circulated through the outer compartment. The temperature of the electrolyte solution can be monitored by an alcohol thermometer during temperature-dependant experiments. The reference electrode is separated from the working electrode compartment by a closed electrolyte bridge to eliminate temperature effects on the reference electrode. The measurements were made using a Pt gauze counter electrode and a Pine Model AFCBP1 potentiostat.

A rotating disc electrode (RDE) consists of a short glassy carbon cylindrical disc embedded in a fitted tube of insulating Teflon. This piece is attached to a rotator shaft which is vertically mounted to a controllable speed motor and rotated at a constant angular velocity about an axis perpendicular to the front face of the glassy carbon disc. Electrical contact to the shaft is made through the rear face of the glassy carbon disc. The RDE is rotated in the electrolyte solution to eliminate transport limitations within the liquid electrolyte. The rotation results in convective transport of solution to the electrode surface, replenishing the solution by a flow normal to the electrode surface. The diffusion layer δ decreases with increasing electrode angular velocity under laminar flow conditions (up to ~4000 rpm) by Equation 4-1 where D is the diffusion coefficient of the reactant, ν is the kinematic viscosity of the electrolyte and ω is the angular velocity.

$$\delta = 1.61 D^{1/3} \omega^{-1/2} \nu^{1/6} \quad \textbf{(4-1)}$$

Rotation speeds of 100-4000 rpm correspond to values in the 5-50 μm range. Also, Equation 4-1 indicates that the thickness of the diffusion layer is independent of disc diameter.

Traditionally, a RDE configuration was used to characterize the electroactive properties of idealized single-crystal substances. For example, a Pt(hkl) single crystal would be prepared by flame annealing and then mounted into the disc position of an insertable electrode. Evaluating electrocatalytic properties of newly developed high surface area electrocatalysts was often measured in a membrane electrode assembly (MEA) configuration. Utilizing the MEA method for extracting the true transport and kinetic properties of the electrocatalyst itself is hampered, however, by incomplete wetting and/or mass transport resistances throughout the entire electrode. Considering these problems, Gloaguen et. al. proposed studying high surface area electrocatalysts in a RDE configuration by binding the electrocatalyst to a glassy carbon electrode with Nafion® [100]. However, extensive mathematical modeling which included ill-defined geometric and material parameters was necessary to establish the properties of the electrocatalyst from the experimental data. The now generally accepted method of studying powder electrocatalysts in a RDE configuration was introduced by Schmidt et al. in 1998 [101]. The simplified method consisted of decreasing the thickness of the Nafion® film until the effects of the film became experimentally negligible. This was

performed by finding the maximum current density for H_2 oxidation at different Nafion® loadings while holding the carbon-supported Pt catalyst loading constant.

To accurately extract the mass-transport properties of nanostructured electrocatalysts from cyclic voltammograms, film diffusion through Nafion and boundary-layer diffusion through the electrolyte must be taken into account. The overall current density i can be looked at as a combination of distinct current density contributions expressed in Equation 4-2.

$$\frac{1}{i} = \frac{1}{i_k} + \frac{1}{i_{RDE}} + \frac{1}{i_f} \tag{4-2}$$

The true kinetic current density contribution of the electrocatalyst is represented as i_k. The boundary-layer diffusion limited current i_{RDE} is determined by the mass transport properties of the RDE. These RDE properties are well-known by the Levich equation given in Equation 4-3 where F is the Faraday constant (96,485 C/mol), A is the electrode surface area, and C is bulk reactant concentration.

$$i_{RDE} = 0.62nFAD^{2/3}\omega^{1/2}\nu^{-1/6}C \tag{4-3}$$

The Nafion film diffusion limited current is represented as i_f in Equation 4-4. This term is controlled by reactant diffusion through the Nafion film and is essential to consider when Nafion is present on the working electrode. This contribution has been defined as in Equation 4-4 [101].

$$i_f = \frac{nFC_f D_f}{L_f} \quad \textbf{(4-4)}$$

In Equation 4-4, C_f and D_f represent the solubility and diffusion coefficient of the reactant in the Nafion® film, respectively. The Nafion® film thickness L_f can be calculated from the Nafion® mass and surface area covered by the film assuming a dry Nafion® film density of 1.98 g/cm^3 [102].

A procedure must be developed to definitively demonstrate the effect of electrocatalyst morphology. It must be experimentally determined if the electrocatalyst nanostructure results in greater activity due to an intrinsic improvement of the local transport properties or if it is merely a result of increased surface area. The transport hindrances due to diffusion through the electrolyte and the ionomer film must be eliminated. It is well-known that elimination of the transport hindrance due to diffusion of reactant species through the electrolyte can be achieved by rotation of the electrode. The point at which the diffusion through the ionomer film is no longer a factor must be experimentally determined for a particular electrocatalyst. This can be achieved by varying the ionomer:catalyst ratio. The catalyst loading on the RDE is held constant while the amount of ionomer deposited on the electrode varies. Beginning with a thick layer of ionomer, the amount can be decreased until no change in performance is observed. At this point, the observed current is not limited by diffusion through the ionomer film.

Once the optimum ionomer:catalyst ratio is established, the catalyst loading is varied while the ionomer:catalyst ratio is held constant to select an optimal catalyst loading. A catalyst loading that is too small will not be reproducible and the current

densities are susceptible to interference from traces of oxygen in the electrolyte. A catalyst loading that is too high can result in the system operating under ohmic control, thereby reducing the electrocatalytic characteristics that can be observed in the data. Unless otherwise stated, the optimal catalyst loading was established and set at 60 $\mu g/cm^2$ which corresponds to 12 μg catalyst on the 0.196 cm^2 glassy carbon RDE. The current densities are either normalized to mass of catalyst (mA/mg_{cat}) or the geometric surface area of the electrode (mA/cm^2) and are interchangeable by the 60 $\mu g/cm^2$ factor.

4.2.5.1 Cyclic Voltammetry (CV)

Cyclic Voltammetry (CV) is a potentiodynamic technique that employs a rotating disk electrode (RDE) as the working electrode in a standard three electrochemical cell. A potentiostat applies a gradual potential ramp to the working electrode. The potential is linearly swept through the potential range of interest and then reverses direction back through this range in a triangular wave-form as in Figure 4.3.

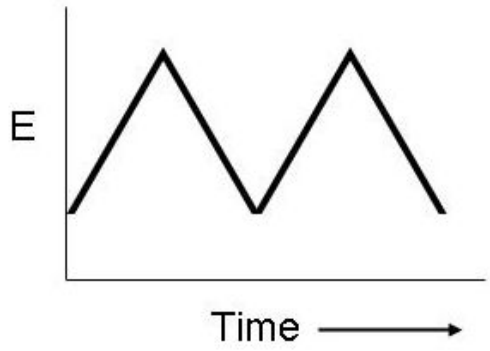

Figure 4.3: Plot of potential vs. time showing a triangular waveform applied by the potentiostat through the potential range of interest used in cyclic voltammetry.

During this scan, the resulting current due to the applied potential is measured by the potentiostat. CV is one of the most common and useful techniques for screening a particular material to determine if it is electroactive.

4.2.5.2 Chronoamperometry

Chronoamperometry is a potentiostatic technique that can be used in conjunction with a rotating disk electrode (RDE) as the working electrode in a standard three electrochemical cell. A potentiostat applies a single potential to the working electrode for a given amount of time (Figure 4.4) and the resulting current due to the applied potential is measured by the potentiostat.

Figure 4.4: Plot of potential vs. time for chronoamperometric studies wherein a single potential is applied by a potentiostat for a given amount of time

This potentiostatic technique provides more steady-state current densities and is more closely related to fuel cell operating conditions than cyclic voltammetry.

4.2.6 Membrane Electrode Assembly (MEA) Studies

The most realistic technique to study the performance of new electrocatalysts is by integration into a membrane electrode assembly (MEA) and evaluation of its performance in a single fuel cell. For a proton exchange membrane fuel cell (PEMFC), the most common solid electrolyte used is Nafion. In the research phase of catalyst development, the catalyst layer is applied to the membrane in the form of an ink. The anodic and cathodic catalyst layer ink is painted on each side of the Nafion membrane followed by application of a gas diffusion layer (GDL) as illustrated in Figure 4.5.

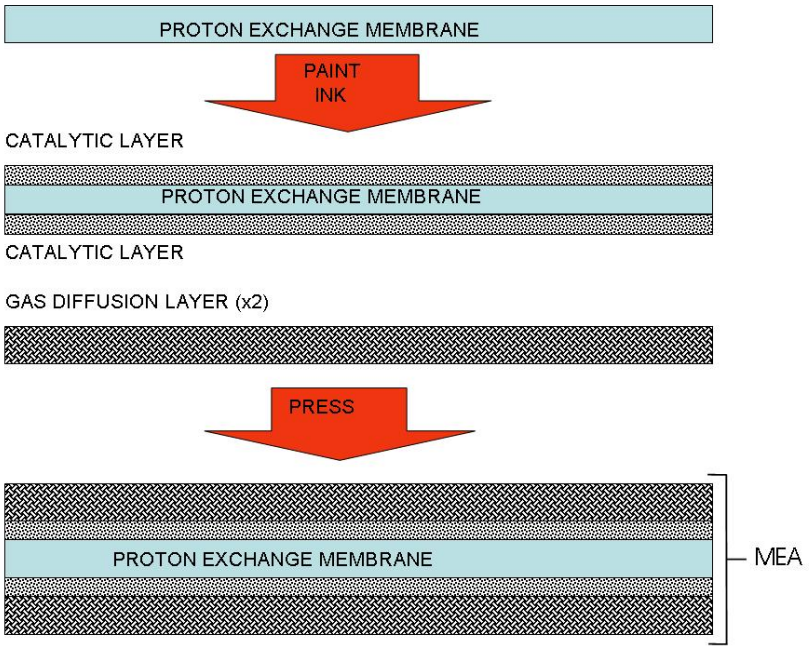

Figure 4.5: Illustration of membrane electrode assembly (MEA) construction process in which the electrocatalyst ink is painted onto either side of the solid electrolyte membrane, most commonly Nafion. A gas diffusion layer is then pressed on either side forming the complete MEA.

To evaluate the performance of a new electrocatalyst, alternative catalyst ink formulations are prepared while all other MEA components remain the same. The

electrocatalyst ink consists of catalyst, ionomer (Nafion) solution and solvents which are sonicated to an ink-like consistency. The standard anode ink was prepared as follows: 50 mg of Pt-Ru (either Pt-Ru Black or Aerosol-derived Pt-Ru), 500 mg deionized water, and 160 mg of 5% Nafion solution. The standard cathode ink was prepared as follows: 50 mg of Pt Black, 500 mg deionized water, and 160 mg of 5% Nafion solution. These catalysts solutions are sonicated and hand painted onto a 1035 Nafion membrane (Ion Power). A gas diffusion layer (GDL LT 1400-W) is added to the anode and cathode and the MEA is then pressed at 1500 lbs. at 125 Cº for 10 min.

The MEA is placed in a 5 cm^2 cell with serpentine flow channels and the bolts are compressed to 80 in-lbs. A Fuel Cell Technologies Fuel Cell Test Station is used to obtain H_2/O_2 and H_2/air polarization curves. Polarization curves were obtained galvanostatically with a 30 second delay before data actuation. The anode and cathode gases were heated and humidified at 85 Cº, and the flow rates were 266 and 466 sccm, respectively. The cell operating temperature was maintained at 80ºC.

5 Templated Pt/C Composites for Electrochemical Oxygen Reduction

5.1 Synthesis of Carbon-Supported Electrocatalysts

5.1.1 Bulk Templating Synthesis

The mesoporous silica template is first synthesized separately in a bulk sol-gel process followed by calcination to remove the surfactant. The mesoporous silica template is then impregnated with platinum and carbon precursors in the form of tetra-amine platinum hydroxide and sucrose, respectively. After pyrolysis and silica template removal, the material consisted of platinum nanoparticles dispersed on carbonaceous fibers that precisely match the silica pore size as shown in Figure 5.1.

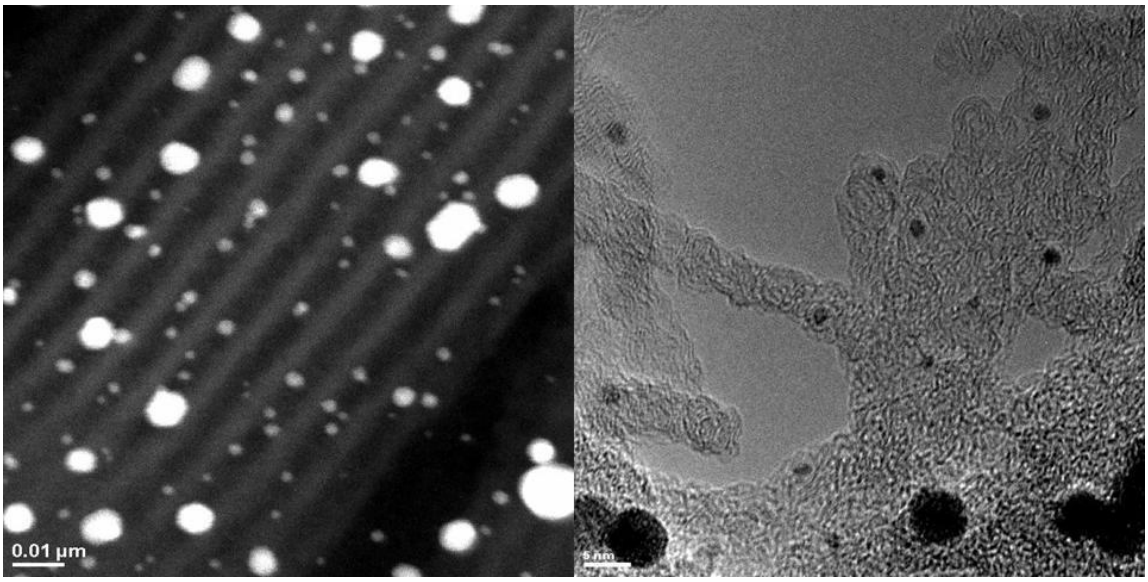

Figure 5.1: TEM images of a carbon-supported platinum composite templated by SBA-15 mesoporous silica shown before (left) and after (right) silica template removal. The diameter of the carbon fibers in the image on the right precisely match the SBA-15 pore size (~6nm).

It is evident from the images in Figure 5.1 that not all of the platinum nanoparticles infiltrate the pores. The larger platinum nanoparticles are formed on the exterior of the silica template and are not constrained by the pores. This bimodal particle size distribution carries over to the final material after template removal.

Extensive TEM studies of the material also showed that the carbon precursor fails to fully infiltrate the silica pores so after silica removal, large "chunks" of untemplated carbonaceous material remain. The electrochemical performance of the bulk templated Pt/C composites was extremely poor, exhibiting severe transport limitations. Representative examples of these observations are shown in Figure 5.2.

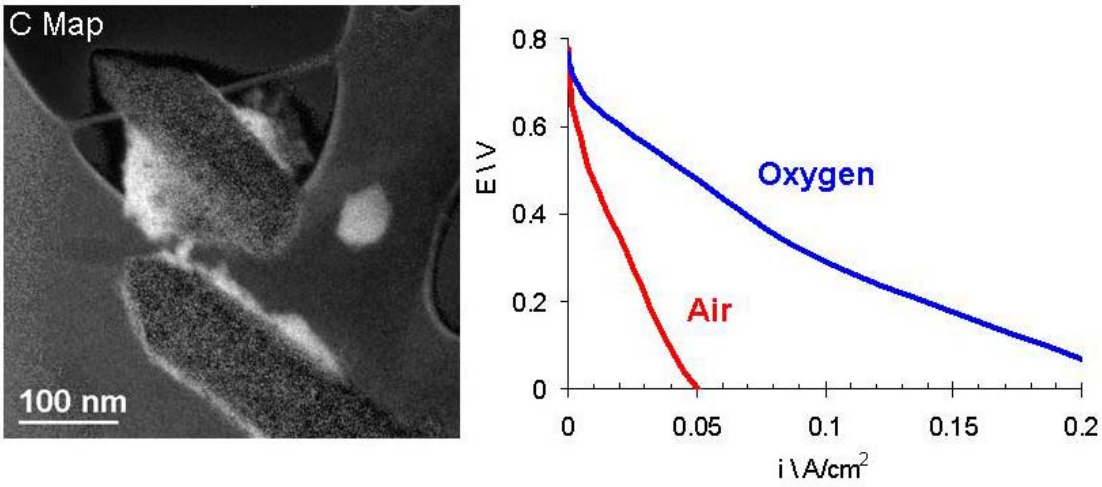

Figure 5.2: Carbon map TEM micrograph of bulk-templated Pt/C composite with carbon shown in white (left). Polarization curve of bulk-templated Pt/C after silica template removal as cathodic catalyst with oxygen and air supplied to the cathode (right).

The severe transport limitations can be observed in the polarization curve of Figure 5.2 wherein a large potential difference for a given current density exists between oxygen and air when supplied to the cathode. This technique is used to elucidate transport hindrances and is explained in more depth in Chapter 9 – Appendix A. These

observations illustrate the inherent disadvantage of the bulk synthesis method which results in inhomogenous materials.

5.1.2 Aerosol Templating Synthesis

Numerous attempts have been made to synthesize an aerosol-derived silica-templated Pt/C composite. The system was first simplified by eliminating the presence of the carbon precursor in the precursor solution in an attempt to understand the formation of the platinum. An example of the resulting material is shown in Figure 5.3.

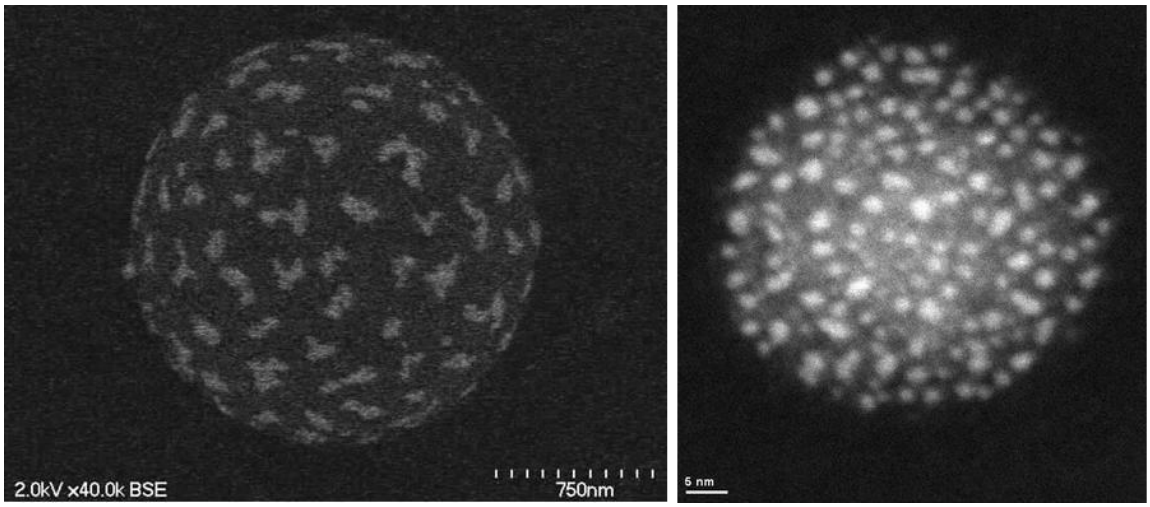

Figure 5.3: SEM backscattered electron (BSE) image of large silica particle (~1.5 um) exhibiting large unreduced platinum islands on exterior (left). STEM image of a small silica particle (~50 nm) exhibiting reduced platinum nanoparticles (~2 nm) (right). Both images are from a one-step aerosol-derived Pt/Silica material.

The one-step aerosol process generated small silica particles (~50 nm) containing reduced platinum nanoparticles (~2 nm) amid large silica particles (~1 um) containing unreduced platinum islands. In the case of the larger silica particles, it is believed that the platinum

precursor is carried to the particle exterior and thus the platinum is not confined in the aerosol particle structure.

It is believed that the presence of carbon in the aerosol droplet facilitates the reduction of platinum. An example of such a material in which the carbon precursor is included in the aerosol synthesis procedure is shown in Figure 5.4.

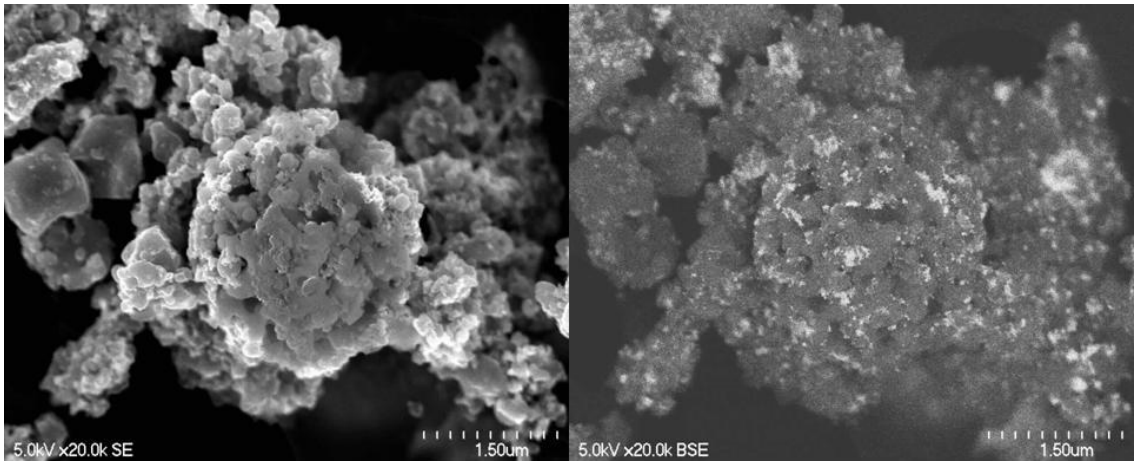

Figure 5.4: SEM secondary electron SE (left) and backscattered electron BSE (right) images of one-step aerosol-derived composite including platinum, silica and carbon that has been partially etched.

Unfortunately, discrete platinum nanoparticles were not observed in the material. The complexity of forming such a material is evident from the images. Modifications to the aerosol synthesis process included altering the furnace temperature, relative precursor concentrations, type of platinum precursors and type of atomizer. Most adjustments resulted in minor benefit. A successful one-step silica templated aerosol synthesis process is extremely complicated. The challenge is ensuring the precise formation sequence of the platinum nanoparticles, carbon support and silica template. Synthesis of an aerosol-derived carbon-supported platinum electrocatalyst represents the most complex material development challenge which should be attempted only after

examining possible aerosol synthesis routes for unsupported nanostructured electrocatalysts like Pt-Ru catalysts for electrochemical methanol oxidation.

6 Nanostructured Pt-Ru Electrocatalysts for Electrochemical Methanol Oxidation in Acid Media

6.1 Synthesis of Pt-Ru Electrocatalysts

6.1.1 Bulk Synthesis

For the bulk synthesis of Pt-Ru electrocatalysts, mesoporous SBA-15 silica was synthesized separately. This was followed by a one-step infiltration of the pores by an aqueous solution of platinum (tetraamineplatinum (II) hydroxide) and ruthenium (hexaammineruthenium (III) chloride) precursors mixed in an equal atomic ratio. TEM micrographs of the material before silica template removal are shown in Figure 6.1.

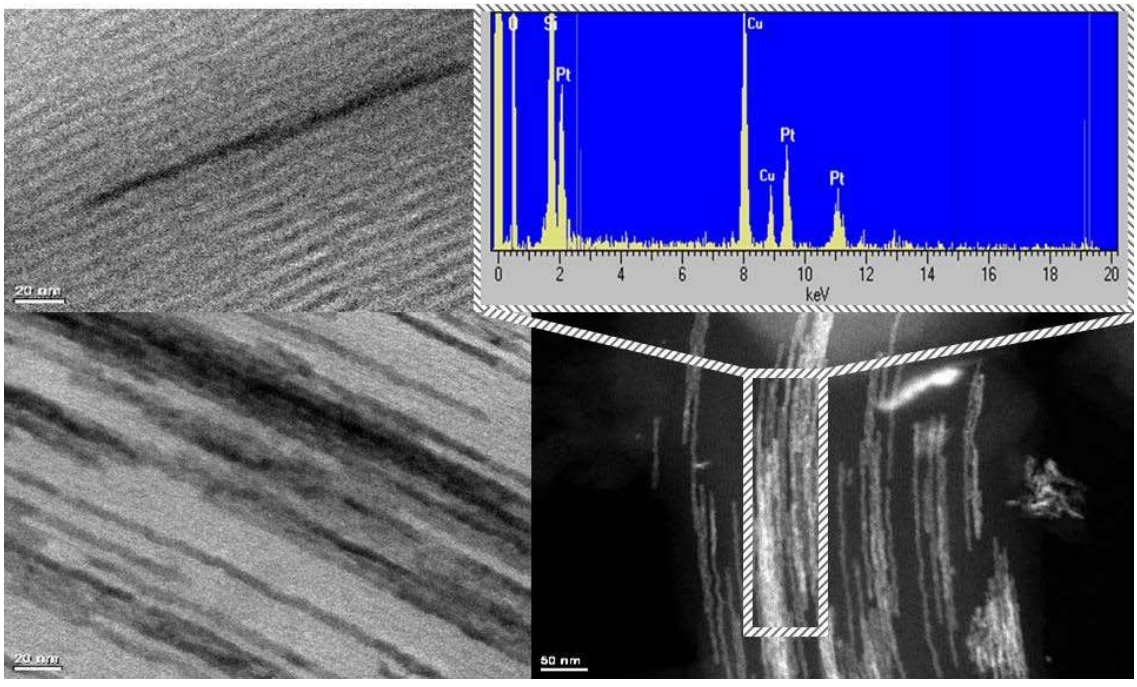

Figure 6.1: TEM images of Pt-Ru material templated by SBA-15 in a bulk synthesis process. The images show incomplete silica pore infiltration. The EDS spectrum shows only platinum present in the particular area examined.

It is evident from the TEM micrographs in Figure 6.1 that the metallic phase does not fully infiltrate the pores of the silica template. In addition, the platinum and ruthenium metallic phase does not form homogenously within the pores. The EDS spectrum in Figure 6.1 of the designated section of the sample where the metallic phase is present shows only characteristic Pt peaks and a complete absence of Ru peaks. These representative micrographs show a serious drawback of the bimetallic bulk synthesis method. The bulk templating technique results in an inhomogeneous material wherein particular structural features cannot be directly associated with electrochemical data. Additionally, an intimate mixing of alloy constituents during synthesis is desirable to promote a high degree of alloying. While used extensively in the literature as described in Section 2.2.2, this bulk synthesis technique is not promising for creating homogeneous templated materials throughout the entire sample.

6.1.2 Aerosol Synthesis

The aerosol synthesis procedure is illustrated in Figure 4.1 of Section 4.1.2. The precursor solution consisted of an aqueous mixture of tetraamineplatinum (II) hydroxide, hexaaminеruthenium (III) chloride and Ludox® TM50 colloidal silica solution with monodisperse silica particles having an average diameter of 20 nm. Several formulations of the metallic precursor/silica template ratio in the precursor solution were investigated. The materials discussed here had varied metallic precursor/silica template ratios in the aerosol precursor solution. The metal/silica molar ratio is 0.4 (50 wt% metal) for the Aerosol LML (Low Metal Loading) sample, metal/silica ratio 1 (70 wt% metal) for the

Aerosol MML (Mid Metal Loading) sample and 1.7 (80 wt.% metal) for the Aerosol HML (High Metal Loading) sample.

6.2 Structural and Compositional Analysis of Templated Pt-Ru

TEM micrographs of the aerosol-derived Pt-Ru materials are shown in Figure 6.2. The Pt-Ru/SiO_2 aerosol-derived particles before silica removal have diameters on the order of one micron as observed in Figure 6.2a and Figure 6.2b. In general, once the silica template was removed, the metallic particles became disconnected, forming smaller derivative particles around 100 nm in the case of the Aerosol LML and MML samples shown in Figure 6.2c and Figure 6.2d, respectively. Other formulations of the precursor solution, namely the Aerosol HML sample, formed a less detached network which resulted in more structured nanocomposite with a higher surface area and greater electrochemical performance. EDS analysis showed the presence of Pt and Ru in approximately the same ratio present in the precursor solution (50 at.% Pt / 50 at.% Ru) and the absence of the silica after silica template removal.

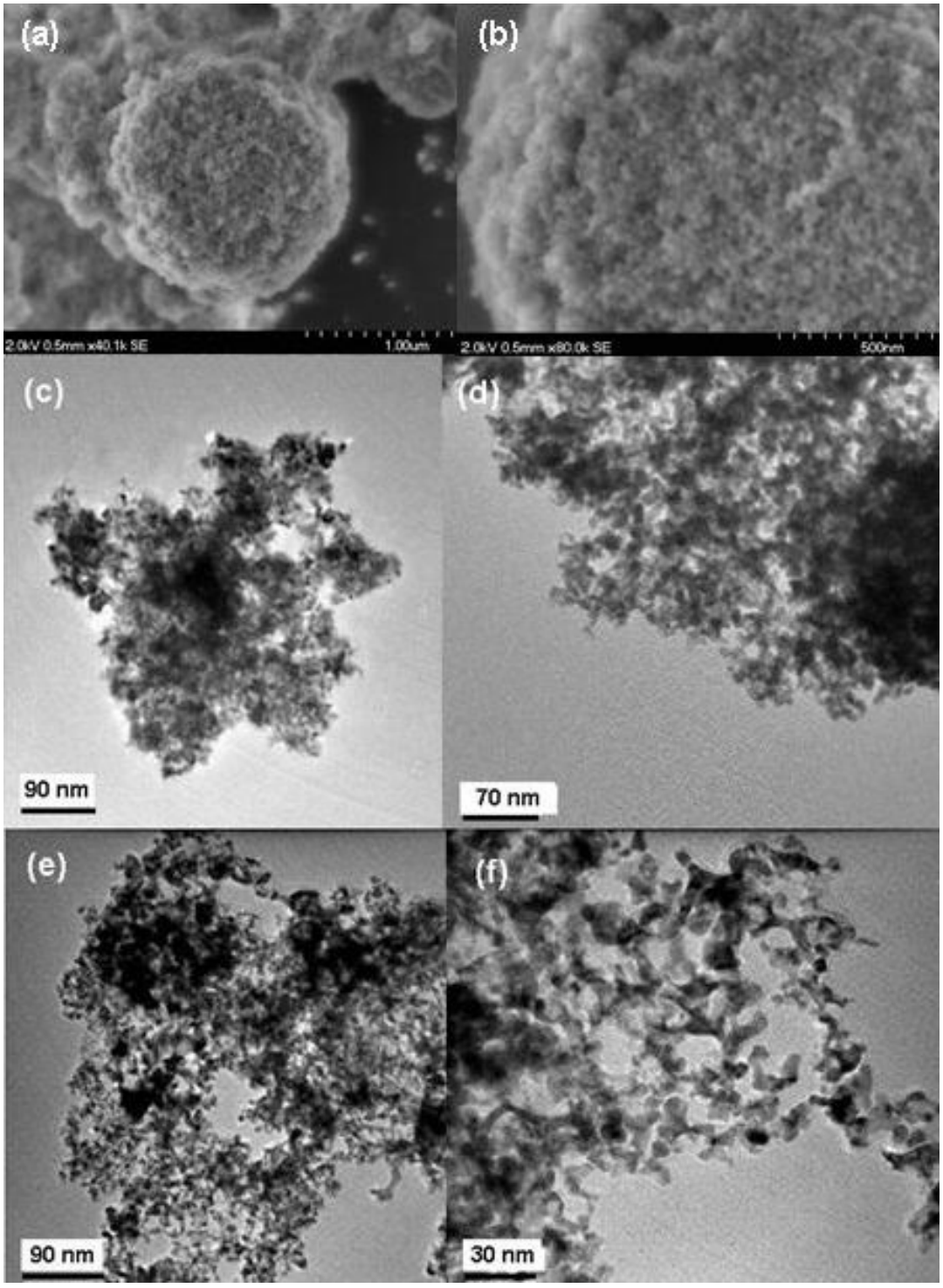

Figure 6.2: SEM micrographs of the aerosol-derived templated Pt-Ru composites before silica template removal with (a) 1 µm and (b) 500 nm scale bar. TEM micrographs of the aerosol-derived templated Pt-Ru nanocomposites after silica template removal are shown for the (c) Aerosol LML sample, (d) the Aerosol MML. The TEM micrographs of the (c, d) Aerosol HML sample show a highly porous, connected Pt-Ru network in which the voids from the 20 nm silica particles are observable.

The Aerosol HML precursor formulation exhibited an open frame structure with a high degree of connectivity as shown in Figure 6.3. The voids which contained the 20 nm silica particles are observable from the micrographs. The Aerosol HML sample also showed the highest BET surface area of 50 m^2/g compared to the Aerosol LML of 10 m^2/g and the Aerosol MML of around 20 m^2/g. For comparison, the commercial Pt-Ru black used in this study was measured at 60 m^2/g while an advanced industrial catalyst for methanol oxidation (commercial 80% Pt-Ru/Vulcan XC-72) has a surface area of 90 m^2/g.

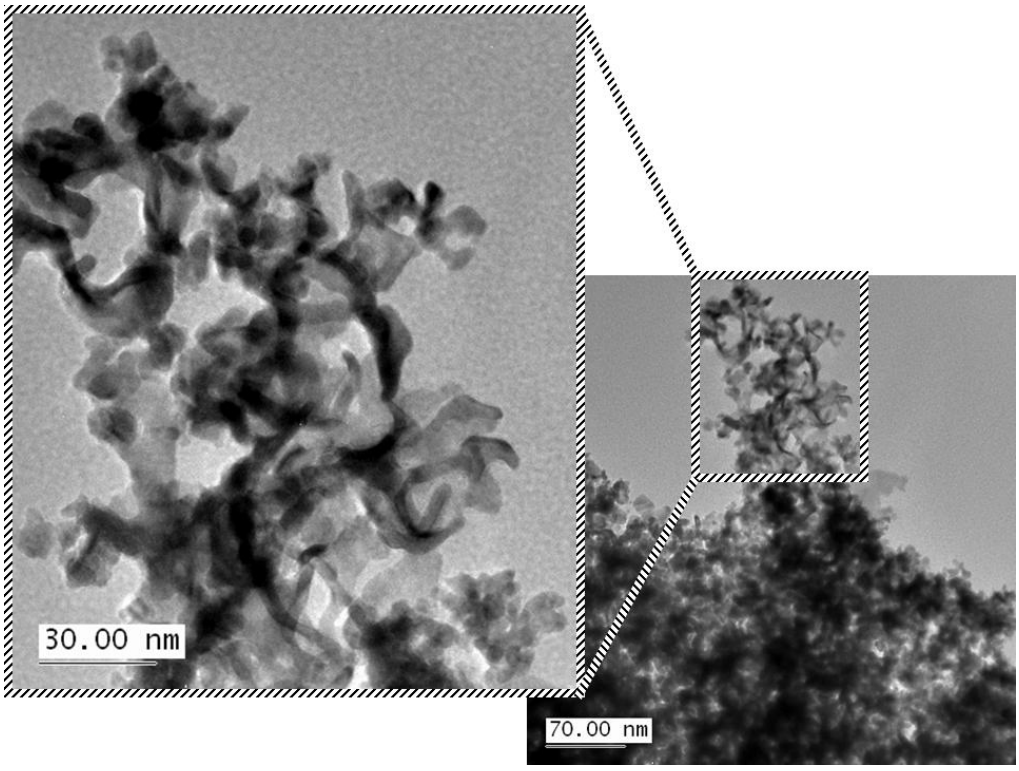

Figure 6.3: TEM micrographs of Aerosol HML sample showing the open frame structure after removal of the 20 nm silica colloids. The voids where the template existed are recognizable.

The X-Ray diffraction (XRD) pattern of the Aerosol HML Pt-Ru nanocomposite is compared to a similarly-synthesized aerosol Pt nanocomposite in Figure 6.4. The sample exhibits only the characteristic diffraction peaks of platinum. There are no

diffraction peaks indicating a presence of pure Ru or Ru-rich hexagonal close-packed (hcp) alloys.

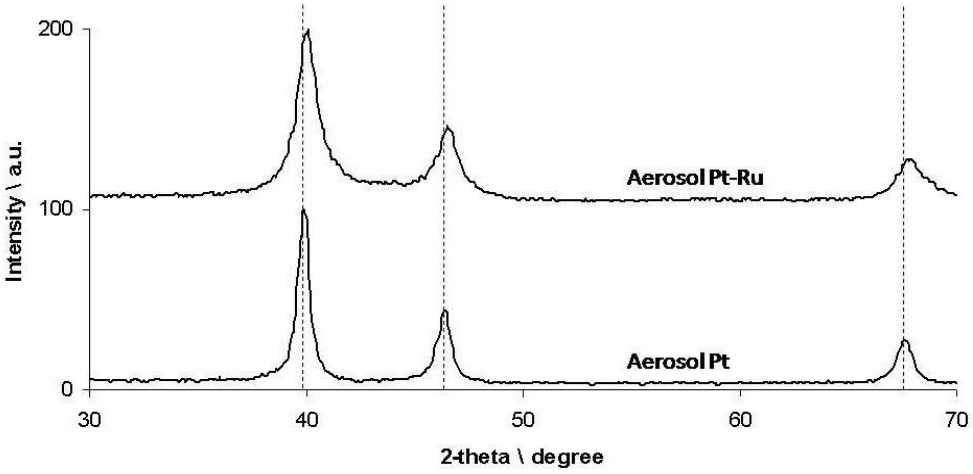

Figure 6.4: XRD diffractograms of templated Pt (bottom) and templated Pt-Ru (top) catalyst powder samples.

The average crystallite size for the aerosol-derived Pt-Ru catalyst can be calculated from the diffraction peak broadening with the use of Scherrer's equation (Equation 5-1) [103] in which λ is the wavelength of the X-ray (1.54056 Å), θ_{max} is the angle at the peak maximum and $B_{2\theta}$ is the width of the peak at half height.

$$d = \frac{0.9\lambda}{B_{2\Theta}\cos\Theta_{max}} \qquad \textbf{(5-1)}$$

The average crystallite size was found to be around 10 nm. The formation of the Pt-Ru alloy in the fcc structure leads to a contraction of the Pt lattice parameter. The lattice parameter (a_{fcc}) for this material can be calculated with Equation 5-2 [104]:

$$a_{fcc} = \frac{\sqrt{2}\lambda}{\sin\Theta_{\max}} \quad \textbf{(5-2)}$$

The diffraction peaks of the aerosol Pt-Ru are similar to the diffraction peaks of the aerosol Pt except for the fact that the 2θ values are slightly shifted to higher values. From this shift, the amount of ruthenium dispersed in the platinum lattice can be estimated from a Vegard's law relationship (Equation 5-3) [105]:

$$\%Ru\ in\ alloy = \frac{a_{fcc}^{Pt-Ru}(nm) - a_{fcc}^{Pt}(nm)}{-0.000124} \quad \textbf{(5-3)}$$

This shift corresponds to a lattice parameter of 0.3906 nm for the aerosol Pt-Ru sample whereas the aerosol Pt sample is calculated to be 0.3913 nm. This shift corresponds to ca. 8% Ru in the alloy for the aerosol Pt-Ru sample. The same analysis for commercial unsupported Pt-Ru Black (Johnson-Matthey Pt:Ru 50:50) results in ca. 30% Ru in alloy form.

X-ray Photoelectron Spectroscopy (XPS) was used to measure the relative Pt:Ru surface compositions of the aerosol-derived templated electrocatalysts and two commercial catalysts used in this study as a benchmark. A commercial unsupported Pt-Ru black (Johnson-Matthey Pt:Ru 50:50) and a state-of-the-art commercial supported 80% Pt-Ru/Vulcan XC-72 catalyst (Johnson Matthey Pt:Ru 50:50) were incorporated into the study. The composition from XPS was measured to be 37% Pt / 63% Ru for the aerosol-derived Pt-Ru (Aerosol HML), 38% Pt / 62% Ru for the commercial Pt-Ru black and 36% Pt / 64% Ru for the commercial 80% Pt-Ru/C catalyst. The very slight

differences in the surface compositions between the three catalysts make a significant comparison possible. Although the bulk Pt:Ru compositions were close to 50:50, the XPS data indicate a ruthenium-rich surface which has similarly been observed in other studies of commercial and laboratory-prepared Pt-Ru composites[106-108].

The oxidation states of Ru determined by XPS before electrochemical testing for the aerosol-derived Pt-Ru (Aerosol HML), commercial Pt-Ru black and commercial 80% Pt-Ru/C are compared in Figure 6.5.

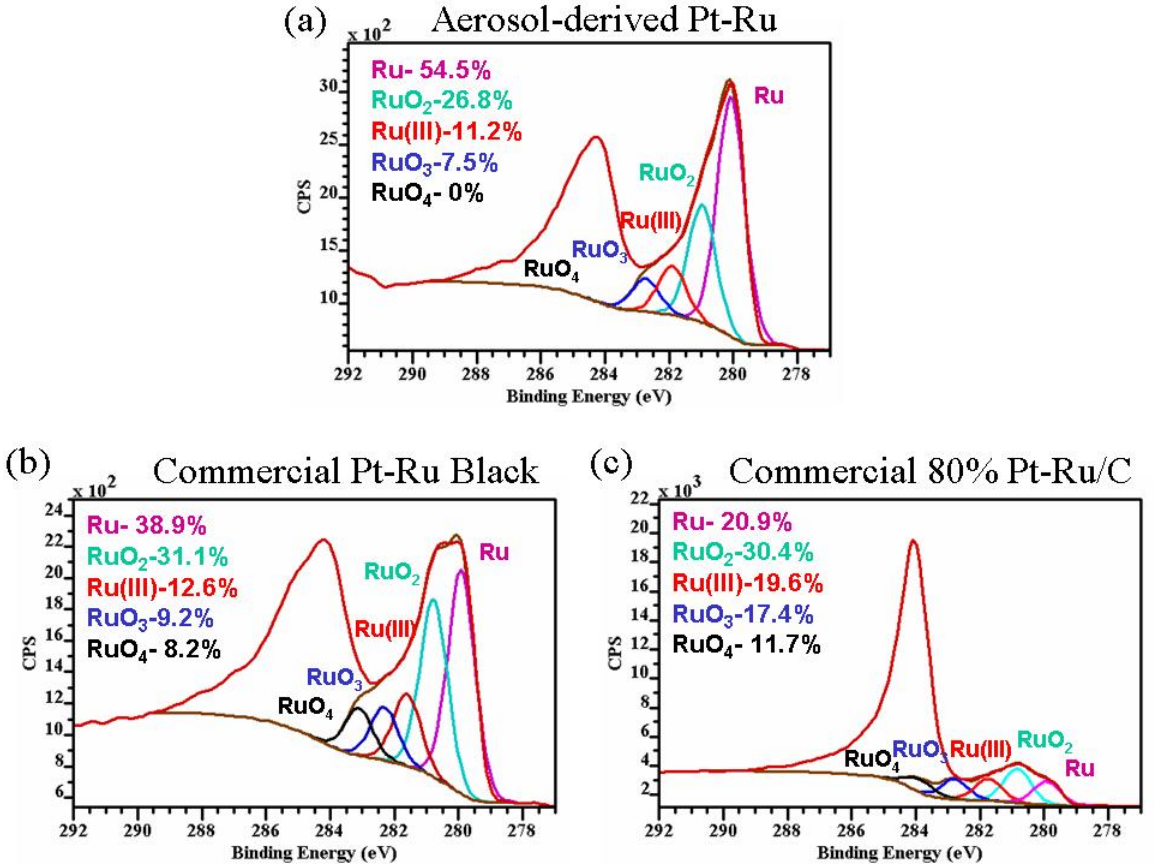

Figure 6.5: XPS spectra of Ru 3d for (a) aerosol-derived Pt-Ru, (b) commercial Pt-Ru black and (c) commercial 80% Pt-Ru/C.

The XPS spectra show the order of metallic Ru for the three samples is Aerosol Pt-Ru > commercial Pt-Ru black > commercial 80% Pt-Ru/C. Although there are few studies on the most active form of Ru for methanol oxidation by Pt-Ru alloys, studies on model single-crystal Pt-Ru surfaces have indicated that the presence of Ru in metallic state is required for methanol electro-oxidation[109, 110]. Some experiments have shown a decrease in methanol oxidation activity due to prior formation (i.e. before continuous operation) of Ru oxides is very small (<5%) and is only observable at potentials above 0.6V vs. RHE[110]. Alternative studies have shown that additional oxidation treatments in air resulted in enhanced electrochemical activity for Pt-Ru/C catalysts which was attributed to further segregation of Ru to surface and formation of RuO_2[108]. In addition, another study has shown Pt-Ru (50:50) catalysts showing the highest activity exhibit oxygen-induced phase separation on the nanoscale with Pt-rich metal embedded in Ru-rich oxide[111]. The accepted opinion here is that metallic Ru is likely required for methanol oxidation and for purposes of this study, the difference in the amount of Ru oxides between the electrocatalysts compared here has a relatively small effect on the methanol oxidation characteristics.

6.3 Analysis of Kinetic and Transport Properties

6.3.1 Rotating Disc Electrode (RDE) Experiments

Cyclic voltammetry was used to compare the methanol oxidation behavior of the samples synthesized from different formulations of the precursor solutions. Cyclic voltammograms of the Aerosol LML (50 wt.% metal), Aerosol MML (70 wt.% metal)

and Aerosol HML (80 wt.% metal) are shown in Figure 6.6. The same mass of each catalyst is present on the RDE and for a more rigorous comparison the current densities are normalized to BET surface area. The Aerosol HML sample exhibited a relatively low onset potential and the highest current density in comparison to the other samples.

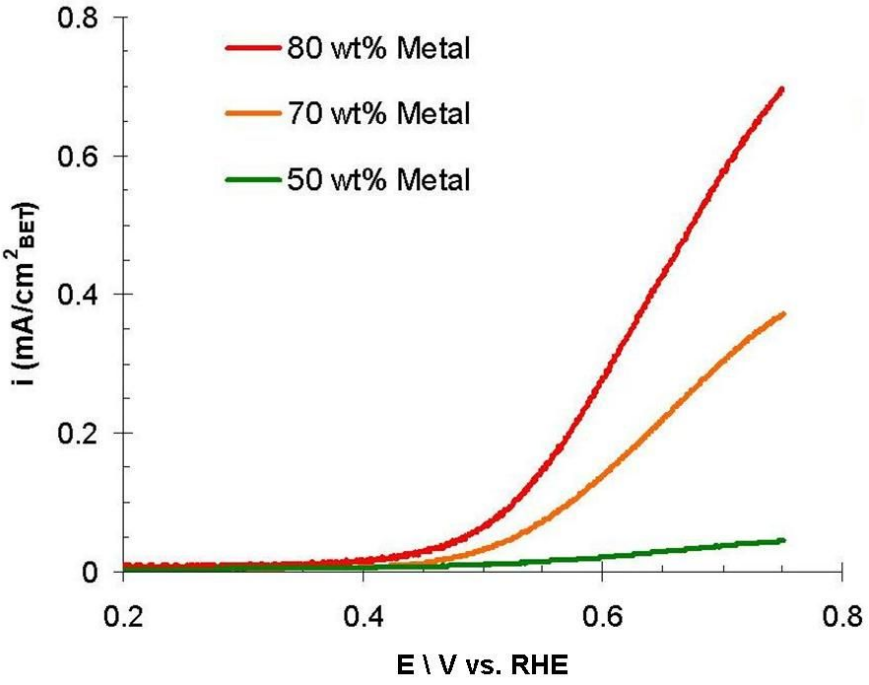

Figure 6.6: Comparison of the methanol oxidation behavior for the Aerosol HML (80wt% metal, red), the Aerosol MML (70wt% metal, orange) and Aerosol LML (50wt% metal, green). The cyclic voltammograms are measured in 0.5M H_2SO_4 / 3M methanol with 10 mV/s scan rate, 1600 RPM RDE rotation rate and 50 µg of catalyst. The current density is normalized to BET surface area.

These results demonstrate that the relative amounts of the metal precursor and silica template in the aerosol precursor solution ultimately determine the final catalyst structure and thus the methanol electro-oxidation behavior. It is evident from Figure 6.6 that the precursor formulations with higher metal/silica template ratios, namely the Aerosol HML sample, result in a greater performance for methanol oxidation. It is believed that a lower metal/template ratio will result in a final material with less network connectivity.

Therefore, if the relative amount of metallic phase is great enough to form around the silica template spheres, a templated bimetallic network will take shape. The fact that alterations in the aerosol precursor formulation result in very different surface areas and electrochemical behavior demonstrates the precursor formulation is a central variable in the development of these type of materials.

The unsupported aerosol-derived templated Pt-Ru (Aerosol HML) catalyst was compared to commercial unsupported Pt-Ru black. For a rough comparison, a state-of-the-art commercial supported 80% Pt-Ru/C was used as a benchmark. The mass-specific current densities from the cyclic voltammetric studies are shown in Figure 6.7.

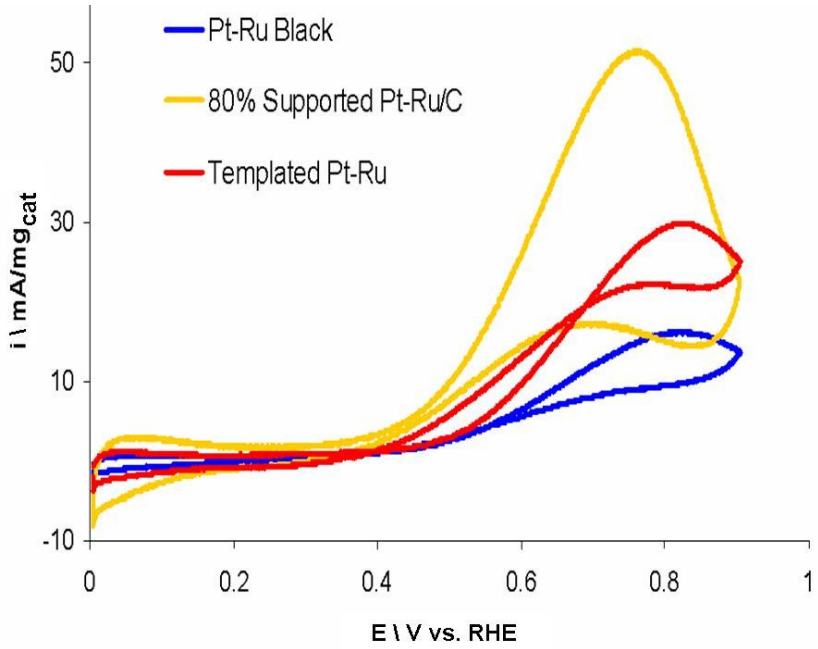

Figure 6.7: Cyclic voltammograms of aerosol-derived templated Pt-Ru, commercial Pt-Ru black and commercial supported 80% Pt-Ru/C measured in 0.5M H_2SO_4 / 3M methanol with 10 mV/s scan rate, 1600 RPM RDE rotation rate and 15 µg metal.

It is apparent that the aerosol-derived templated Pt-Ru catalyst exhibits higher current densities per gram of catalyst in comparison to the analogous unsupported Pt-Ru black.

The commercial 80% Pt-Ru/C results in the greatest overall performance for methanol oxidation with the lowest methanol oxidation onset potential and highest peak current density. Despite having a lower BET surface area than the commercial electrocatalysts, and having approximately the same Pt:Ru composition, the Aerosol HML sample demonstrated a notable methanol oxidation capability. This is especially illustrated if the current densities of the cyclic voltammograms are normalized to BET surface area as in Figure 6.8.

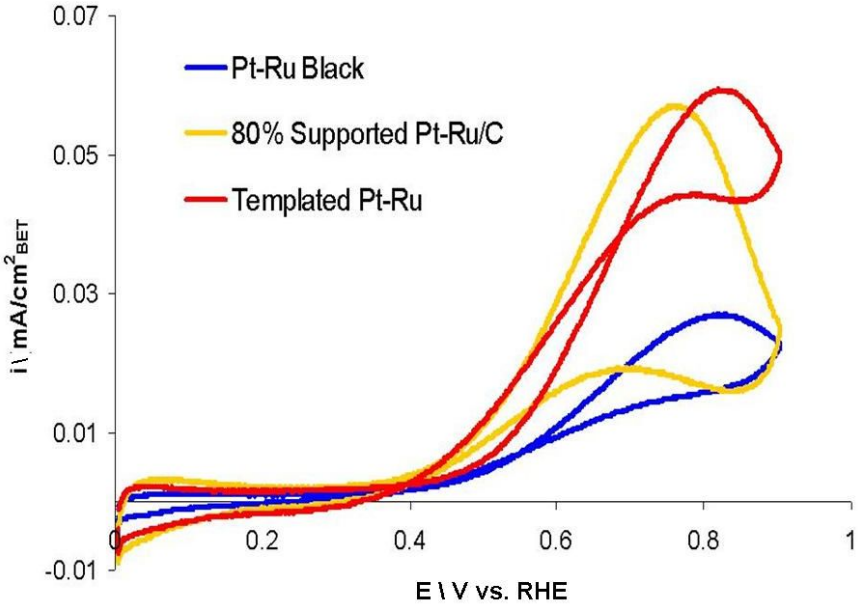

Figure 6.8: Cyclic voltammograms of aerosol-derived templated Pt-Ru, commercial Pt-Ru black and commercial supported 80% Pt-Ru/C measured in 0.5M H_2SO_4 / 3M methanol with 10 mV/s scan rate, 1600 RPM RDE rotation rate and 15 µg metal. The current density is normalized to BET surface area.

In comparing the templated Pt-Ru and the Pt-Ru black in Figure 6.8, the improvement in methanol oxidation current density provided by the nanostructured Pt-Ru catalyst is emphasized. This is an important result because it indicates that despite having a lower BET surface area, the accessibility of the reactive surface may be greater for the

nanostructured material than for the Pt-Ru black catalyst. This proposition is supported by an analysis of the two structures by TEM. Representative TEM micrographs of the Pt-Ru black and the aerosol-derived templated Pt-Ru catalysts are shown in Figure 6.9.

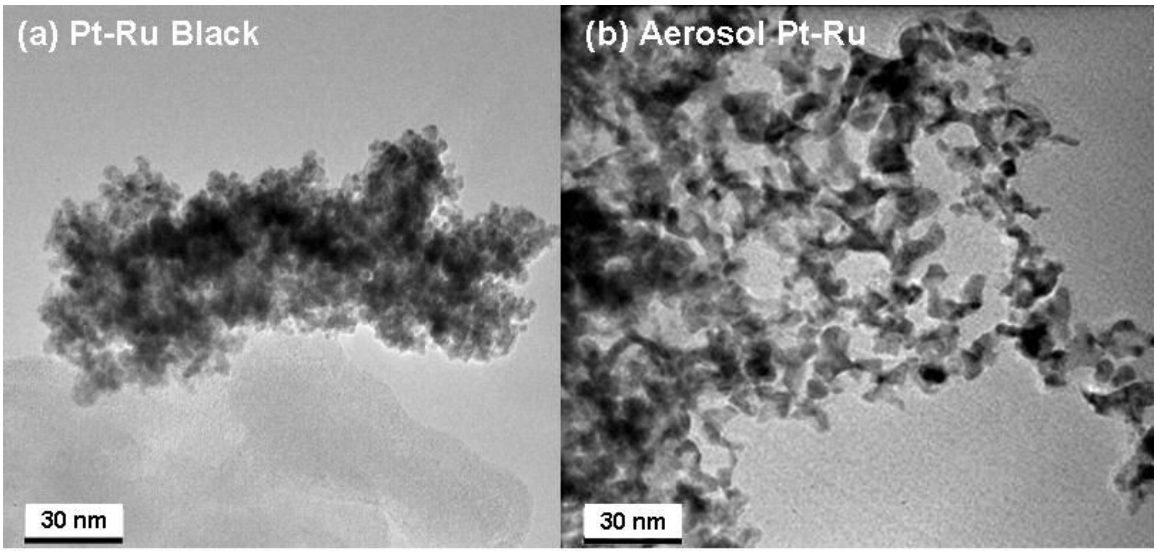

Figure 6.9: TEM micrographs of (a) the commercial Pt-Ru black and (b) the aerosol-derived templated Pt-Ru catalyst.

While the Pt-Ru black catalyst appears as a cluster of agglomerates, the open frame structure of the aerosol-derived templated Pt-Ru electrocatalyst is observable in Figure 6.9. An approximate comparison of the electrochemically accessible surface areas can be calculated from the charging currents of the background cyclic voltammograms assuming a specific capacitance of the catalysts. A comparison between the commercial Pt-Ru black and the aerosol-derived templated Pt-Ru is shown in Table 6.1.

Catalyst	Pt:Ru Composition[a]	BET Surface Area (m^2/g)	Electrochemically Accessible Surface Area (m^2/g)[b]
Aerosol Pt-Ru	38:62	65	36
Pt-Ru Black	37:63	50	44

Table 6.1: Comparison of Pt-Ru Black and aerosol-derived templated Pt-Ru (Aerosol HML). [a]Determined by XPS. [b]From cyclic voltammograms charging current assuming a specific capacitance of 40 uF/cm^2 for both catalysts.

From Table 6.1, it is evident that the electrochemically accessible surface area for the templated Pt-Ru catalyst reaction is greater than that for the Pt-Ru black catalyst. The differences in the Pt:Ru surface composition determined from XPS are negligible. These results indicate that the open frame structure of the aerosol-derived catalyst is advantageous for electrochemical reactions by increasing the accessibility of the reactive surface area.

6.3.2 MEA Experiments to Study Catalyst Layer Transport Effects

6.3.2.1 Theoretical Background

Understanding of mass transport in the DMFC anode in its entirety (flow fields, gas diffusion layer and catalytic layer) is extremely complicated. The primary reason is the existence of two-phase liquid (reactant methanol solution) and gas (product carbon dioxide) flow. While the majority of papers have focused on the diffusion layer and flow field geometry, there is a conspicuous absence of studies that focus solely on the active layer morphology. It is logical that in this layer, the complex transport of methanol is affected by the gaseous CO_2 flow behavior, CO_2 production rate and catalyst geometry. It is also reasonable that the morphology of the active layer becomes even more important in smaller fuel cells.

In studies of carbon dioxide evolution patterns using in-situ cameras, it was observed that the product gas is not uniformly produced at the diffusion layer (DL) [4]. This was attributed to the structure of both the DL and the catalytic layer. Accumulation

of gas in the DL and catalytic layer leads to large bubbles which are not removed until planar movement to an open channel occurs.

The influence of catalytic layer morphology was examined by a comparison of polarization curves of MEAs with synthesized nanostructured electrocatalysts and conventional electrocatalysts. All MEAs were fabricated identically except for the anode catalyst utilized. Supplying an extremely high oxygen concentration to the cathode ensures that the limiting current density is a result of the methanol transport limitation rather that the oxygen transport limitation. The challenge is how to experimentally measure distinctive transport characteristics of electrocatalyst layer morphologies. This challenge can perhaps be illuminated by approximation of a mass transport coefficient. This technique has been used to analyze the transport characteristics of different flow field morphologies [112].

Consider the schematic of the DMFC anode shown in Figure 6.10 which includes the gas flow field (FF), diffusion layer (DL), catalytic layer (CL) and solid electrolyte membrane (M). At each interface there is a boundary methanol concentration: the concentration at the FF-DL interface is represented as C_{DL}, the concentration at the DL-CL interface is represented as C_{CL}, and the concentration at the CL-M is represented as C_M.

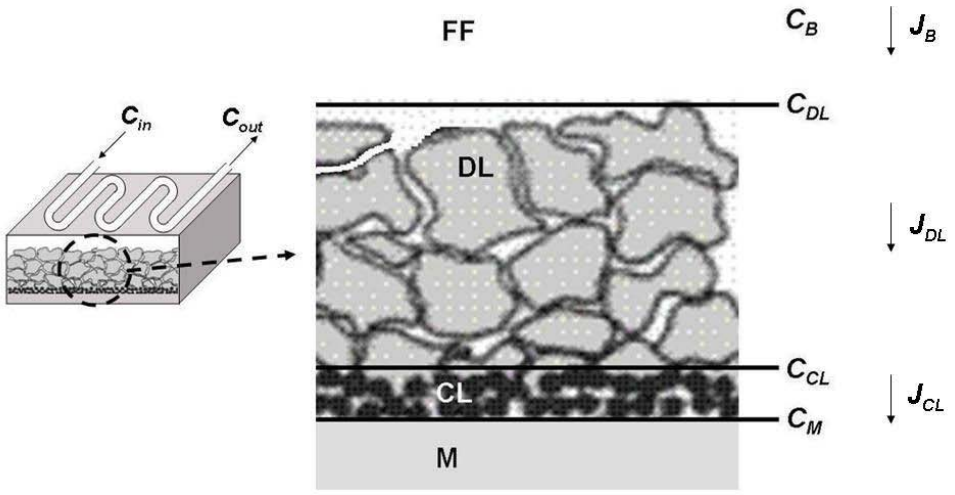

Figure 6.10: Illustration of DMFC anode: Concentration of reactant in C_{in} and out C_{out} of the gas flow field (FF), diffusion layer (DL), catalytic layer (CL) and solid electrolyte membrane (M). The methanol concentration at the FF-DL interface is C_{DL}, at the DL-CL interface is C_{CL}, at the CL-M is C_M and in the FF is C_B.

The methanol concentration in the bulk flow field (C_B) can be estimated by Equation 6-5 which is the average of the methanol concentration in (C_{in}) and out (C_{out}).

$$C_B = \frac{C_{in} + C_{out}}{2} \tag{6-5}$$

According to Faraday's 1st law of electrolysis, the overall methanol flux (J_{TOT}) through the anode can be estimated by Equation 6-6. This equation includes the total cell current (I), Faraday's constant (F), the molecular weight of methanol (M) and the methanol crossover flux (J_M).

$$J_{TOT} = \frac{I}{6F} M + J_M \tag{6-6}$$

The mass flux of methanol is influenced by three mass transfer resistances corresponding to three different regions of the anode. The mass transfer from the flow field to the FF-DL interface is characterized by flow channel hydrodynamics and CO_2 bubbles released at this interface [4]. Gas bubbles can accelerate the methanol solution velocity which increases the convective mass-transfer coefficient but the bubbles can also decrease the effective area for methanol transport [113]. The mass flux in this region can be expressed in Equation 6-7 which accounts for both factors. In this equation, the electrode area is expressed as A, the flow field open ratio is expressed as δ, the FF-DL interface gas coverage fraction is expressed as β and the FF-DL mass transfer coefficient is expressed as h. It is very difficult to accurately quantify both β and h [112].

$$J_B = A\delta(1-\beta)h(C_B - C_{DL}) \quad \textbf{(6-7)}$$

Mass transport in the DL is also very difficult to definitively quantify so an effective mass transfer resistance parameter (k_{DL}) is used in Equation 6-8. This parameter takes into account the effects of gaseous CO_2 pore blocking and non-uniform transport paths due to the interdigitated flow fields.

$$J_{DL} = Ak_{DL}(C_{DL} - C_{CL}) \quad \textbf{(6-8)}$$

Similarly, mass transport in the CL is challenging to accurately define. Consequently, a preliminary attempt will be made to define an effective mass transfer

resistance parameter (k_{CL}) which incorporates all effects on mass transport within this layer.

$$J_{CL} = Ak_{CL}(C_{CL} - C_M) \tag{6-9}$$

For simplicity, it is assumed that the effective mass transfer coefficient for the catalytic layer (k_{CL}) in Equation 6-9 incorporates the catalytic surface area and reaction rate constant as well as the convective and diffusive mass transfer elements. Perhaps this term is too broad in content although the extreme complexity of the DMFC anode catalytic layer necessitates such an approximation. As the project progresses with further data, deconvolution of this broad term will be undertaken.

Equation 6-10 is an incorporation of the methanol mass fluxes for each region from Equation 6-7, Equation 6-8 and Equation 6-9. The result is the establishment of an overall effective mass transfer parameter (k_{TOT}).

$$j = \frac{J_{TOT}}{A} = \frac{C_B - C_M}{\left(\frac{1}{\delta(1-\beta)h} + \frac{1}{k_{DL}} + \frac{1}{k_{CL}}\right)} = k_{TOT}(C_B - C_M) \tag{6-10}$$

The goal now is to relate this effective mass transport parameter (k_{TOT}) to an experimentally measurable quantity. This can be accomplished by substitution of Equation 6-10 into Equation 6-6 which results in Equation 6-11.

$$k_{TOT}(C_B - C_M) = \frac{i}{6F} + j_M \tag{6-11}$$

For a given bulk concentration (C_B), there is a limiting current density (i_{lim}) at which the concentration of methanol at the catalyst-membrane interface (C_M) goes to zero. It can be assumed that at this point, the methanol crossover flux (j_M) goes to zero. Therefore, the limiting current density can be expressed as in Equation 6-12.

$$i_{\lim} = 6Fk_{TOT}C_B \tag{6-12}$$

To redefine the bulk concentration (C_B), a mass balance is performed over the entire flow channel and is expressed in Equation 6-13 where Q is the volumetric flow rate of methanol.

$$C_{out} = C_{in} - \frac{i_{\lim}A}{6FQ} \tag{6-13}$$

At this point, Equation 6-13 can be substituted into the original definition of (C_B) in Equation 6-5 which results in the definition for C_B in Equation 6-14.

$$C_B = C_{in} - \frac{i_{\lim}A}{12FQ} \tag{6-14}$$

Finally, this definition for bulk concentration (C_B) can be put into Equation 6-12 and the final result is Equation 6-15.

$$i_{\lim} = \frac{6Fk_{TOT}}{1+\frac{Ak_{TOT}}{2Q}}C_{in} \tag{6-15}$$

For a given methanol flow rate (Q), a limiting current density (i_{lim}) exists for a particular inlet methanol concentration (C_{in}). Equation 6-15 can be rearranged into Equation 6-16 to plot the experimentally measurable quantity (i_{lim}) and an experimental variable (Q) where the effective mass transport parameter (k_{TOT}) can be calculated from the intercept.

$$\frac{1}{i_{\lim}} = \left(\frac{A}{12FC_{in}}\right)\cdot\frac{1}{Q} + \left(\frac{1}{6Fk_{TOT}C_{in}}\right) \qquad \textbf{(6-16)}$$

An attempt to study the mass transport properties of synthesized nanostructured electrocatalysts was based on the relationship in Equation 6-16. For a particular MEA, a limiting inlet methanol concentration (C_{in}) was experimentally determined and set at 0.5M methanol. This was accomplished by finding an inlet methanol concentration resulting in a sharp drop in cell voltage at high current densities as illustrated in Figure 6.11.

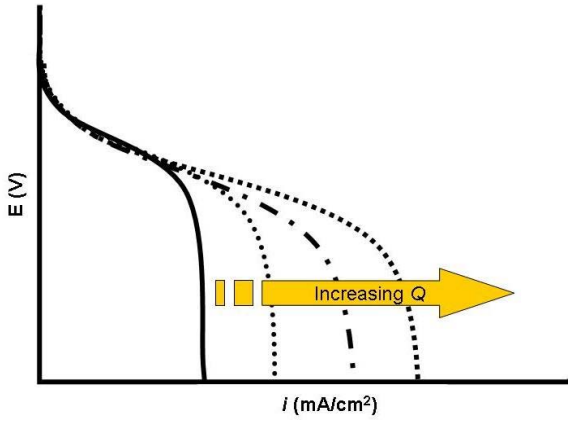

Figure 6.11: Expected polarization curves for transport limited cell with increasing flow rates (Q). The limiting current density (i_{lim}) for a given inlet methanol concentration and flow rate is the point at which the polarization curve encounters the x-axis.

The limiting current density (i_{lim}) is reached due to a severe depletion of methanol in the catalytic layer which also inhibits methanol crossover. The limiting inlet methanol concentration (C_{in}) was fixed at 0.5M methanol for all subsequent experiments. At high concentrations of methanol, around 2M, a sharp drop in cell voltage was not observed unless the flow rate was extremely low. At a high concentration, methanol transport is not the limiting factor in cell performance but limitations are instead due to crossover or kinetics.

The overall effective mass transport coefficient (k_{TOT}) can be calculated from the intercept of $1/i_{lim}$ vs. Q for a particular MEA. If the MEAs were synthesized in identical manner, the slope (in Equation 6-16) should be the same for each MEA. It was hypothesized that an open frame structured electrocatalyst would exhibit higher mass transport limited currents for a given inlet concentration and flow rate than a traditional electrocatalyst resulting in a higher overall effective mass transport coefficient (k_{TOT}).

6.3.2.2 Results of MEA Experiments

Several membrane electrode assemblies (MEAs) were fabricated for the Pt-Ru Black and Aerosol Pt-Ru catalysts in the anodic catalyst ink. Unfortunately, the limiting current densities for each particular MEA were not especially reproducible. The results in Figure 6.12 are of MEAs which exhibited the best overall performance measured for the Pt-Ru Black and Aerosol Pt-Ru catalysts in the anodic catalyst ink.

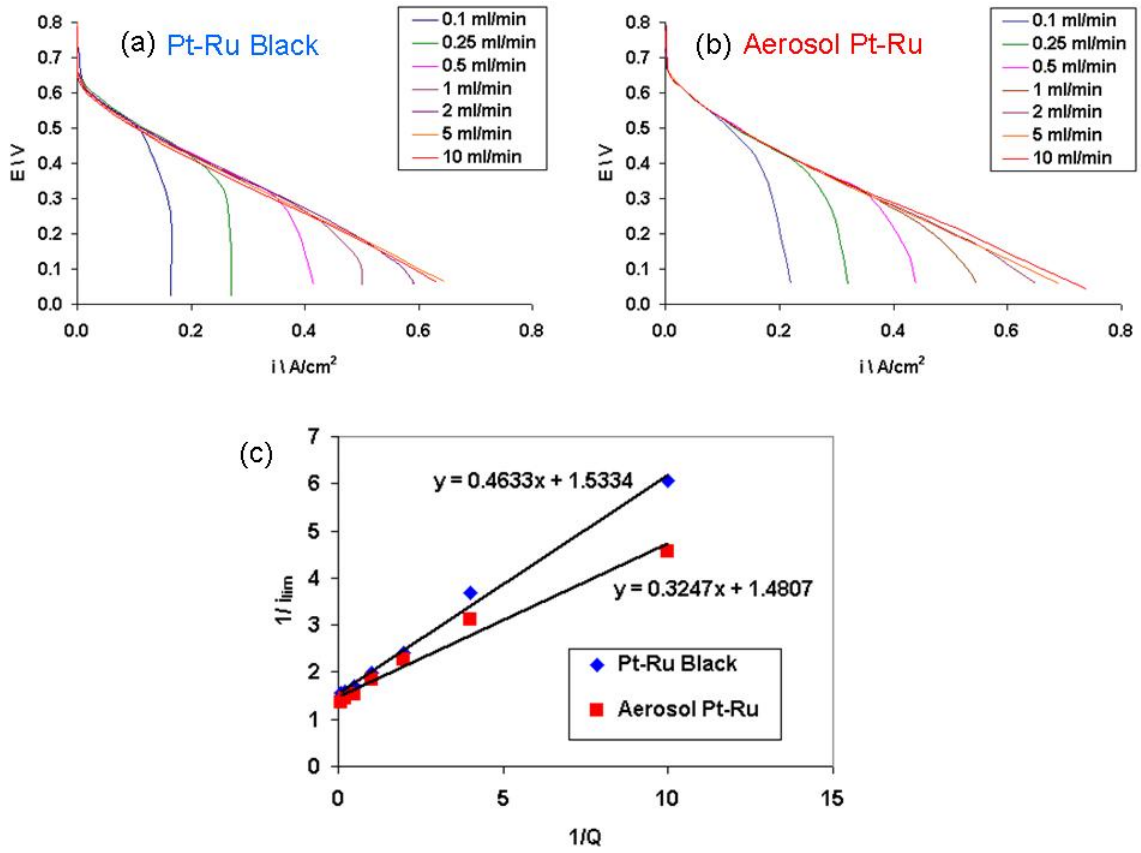

Figure 6.12: Polarization curves for DMFC in single-cell configuration and 0.5M methanol feed for (a) commercial Pt-Ru black and (b) aerosol Pt-Ru in anodic catalyst ink. (c) limiting current vs. flow rate in each polarization curve is compared by the lower graph in which the intercept is related to the overall mass transfer coefficient of each MEA.

For the methodology described in Section 6.3.2.1, an accurate comparison of transport effects due to catalyst layer morphology requires that the slopes of the $1/i_{lim}$ vs. 1/Q plot be identical. As observable in Figure 6.12(c), the slopes are dissimilar meaning that each intercept corresponding to the overall effective mass transport coefficient (k_{TOT}), cannot be compared as a direct result of catalyst layer morphology.

As an overall observation, the theoretical method to study the effect of catalyst layer morphology was found to be experimentally impractical. The method of MEA fabrication in a laboratory setting is not standardized enough to evaluate transport effects at the nanometer level due to variations in the catalyst layer at macroscopic levels.

Catalyst layer transport effects not due to nanoscopic catalyst design may include variations introduced during MEA fabrication e.g. deposition of the catalyst layer. In this study, deposition of the catalyst ink onto the membrane was performed by hand painting the catalyst ink in a cross-hatch pattern. The results of this method can vary by person and as likely observed in this study, the results may vary even if done by the same hand. In addition, slight variations in catalyst ink formulations due to human error can also contribute to variations in catalyst layer morphology and accessiblility of the catalyst surface. These variations could lead to incomplete wetting of the catalyst surface by the aqueous methanol feed.

Currently, studying the effect of catalyst layer morphology by the MEA method is not a viable approach. It is expected that the RDE studies provide the most valuable technique because the catalyst performance alone is extracted from the experimental variations present in MEA experiments.

7 Nanostructured Pt-Sn Electrocatalysts for Electrochemical Ethanol Oxidation in Alkaline Media

7.1 Templated Pt-Sn Electrocatalysts

7.1.1 Catalyst Synthesis

In previous Pt-Ru work, aerosol-derived templated Pt-Ru electrocatalysts were evaluated for the electro-oxidation of methanol in acid media [114]. Despite these Pt-Ru composites having a lower BET surface area compared to commercial Pt-Ru black, the electrochemical performance suggested a higher metal utilization for the templated materials. In this work, an aerosol-derived templated Pt-Sn electrocatalyst having 80% Pt and 20% Sn composition is compared to a templated Pt catalyst synthesized in an equivalent process. We examine the aerosol-derived templated electrocatalysts in conjunction with the poly(phenylene) ionomer for ethanol, methanol and CO oxidation in alkaline media. The templated catalysts are synthesized in an aerosol-based approach in which mono-disperse silica nanoparticles are used to template the metallic precursors.

In this method of assembly, a precursor solution is atomized ultrasonically and undergoes spray pyrolysis. For the Pt-Sn catalyst, the precursor solution consisted of tetraamineplatinum (II) hydroxide, tin (II) chloride and Ludox® TM50 colloidal silica solution. The templated Pt sample was synthesized with a similar precursor solution except the metal/silica template ratio was increased due to an increased amount of tin precursor. Several attempts at synthesizing a Pt-Sn composite were made in a similar manner to the Pt-Ru composite, however, the amount of tin in the precursor solution was

consistently lower than that from EDS analysis. This is likely due to the character of the tin precursor which was not an amine complex like in the case of Pt and Ru. It is believed that the electrostatic attraction between the cationic amine complex (Pt or Ru) and the negative surface polarization of the silica template results in a templated material directly matching the precursor solution metallic ratios. However, for the synthesis of Pt-Sn composites, there is an absence of available amine tin complexes. Therefore, the amount of tin was increased in the precursor solution to increase the Pt-Sn ratio of the final material as determined by EDS. For the Pt-Sn composites presented in this study, the metal:silica template molar ratio was held at 2:1.

7.1.2 Structural and Compositional Analysis

The aerosol synthesis technique can produce a range of metallic compositions, although for the purposes of this analysis, two particular electrocatalysts were studied and compared. The first was a templated 100% Pt catalyst and the second was a templated Pt-Sn catalyst having an atomic composition of 80% Pt / 20% Sn, as determined by Energy Dispersive Spectroscopy (EDS). SEM and TEM micrographs of the templated catalysts before and after silica template removal are shown in Figure 7.1.

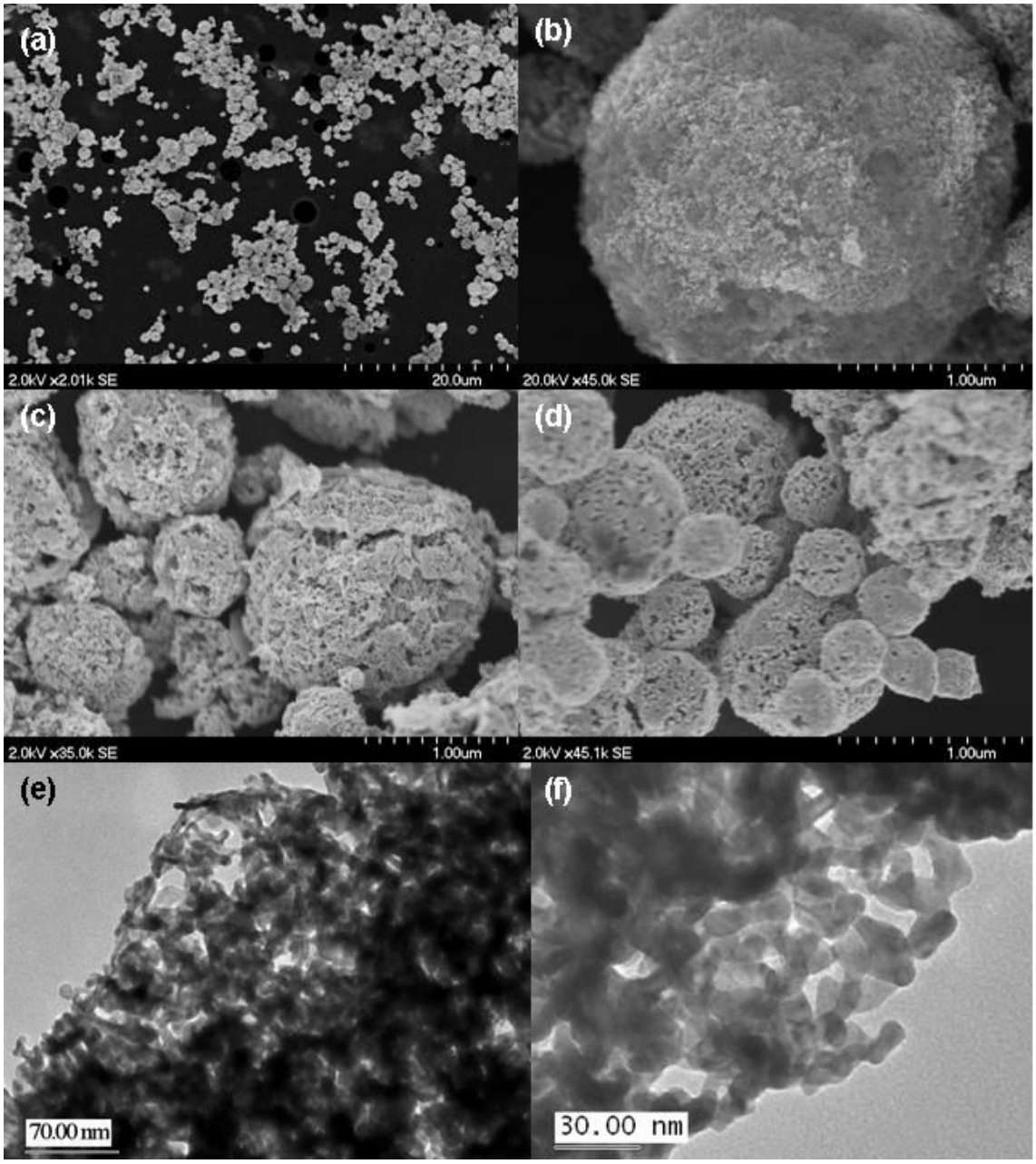

Figure 7.1: SEM micrographs of aerosol-dervied templated Pt-Sn catalyst before silica template removal with (a) 20um scale bar and (b) 1 um scale bar. SEM micrographs of templated (c) Pt-Sn and (d) Pt catalysts after silica template removal. TEM micrographs of templated Pt-Sn catalyst after silica template removal with (e) 70 nm scale bar and (f) 30 nm.

The templated Pt-Sn composite before silica template removal is shown in Figure 7.1(a-b) wherein the spherical morphology characteristic of the aerosol process can be observed. The templated Pt-Sn (Figure 7.1c) and Pt (Figure 7.1d) catalysts after silica

template removal exhibit similar templated morphology. In (Figure 7.1e-f), the voids formed by the silica template can be observed in particular along the thinner edges of the composite whereas in the thicker (darker) regions of the sample, some porosity is still observable. The surface areas of the templated electrocatalysts were approximately 25 m^2/g as measured from BET surface area analysis. X-ray diffraction patterns of the templated Pt and templated Pt-Sn sample are shown in Figure 7.2 and exhibit the characteristic peaks of face-centered cubic (fcc) crystalline Pt.

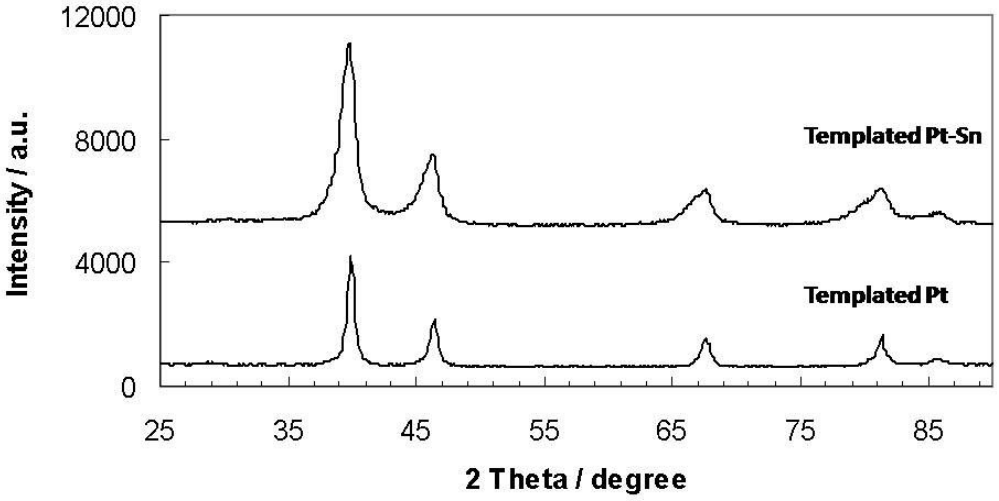

Figure 7.2: XRD diffractograms of templated Pt (bottom) and templated Pt-Sn (top) catalyst powder samples.

The diffraction peaks for the templated Pt-Sn catalyst are slightly shifted to lower 2-theta values with respect to the corresponding peaks of the templated Pt catalyst. No peaks for tin or tin oxide are evident which suggests these species could be present in highly dispersed or in amorphous form. Similar results have been obtained in other studies of Pt-Sn composites [74, 115, 116]. It has been asserted that Pt forms nearly all possible alloys with Sn instead of only the five intermetallic phases (Pt_3Sn, PtSn, Pt_2Sn_3,

$PtSn_2$, $PtSn_4$) distinguished by distinctive XRD patterns [117]. A downward shift in 2-theta values for Pt-Sn composites in comparison to pure Pt would then indicate the incorporation of Sn into the Pt fcc lattice. The change in the Pt fcc crystal lattice parameter has been considered a measure of the extent of alloying in previous literature [118, 119] although a Vegards' type relationship between lattice parameter and alloy composition for Pt-Sn alloys has not been established like in the case of Pt-Ru alloys at this time. The lattice parameters for the templated Pt and templated Pt-Sn catalysts calculated from the XRD patterns are 0.3916 nm and 0.3935 nm, respectively. As opposed to the formation of a Pt-Ru alloy, the formation of a Pt-Sn alloy in the fcc structure leads to an expansion of the lattice parameter.

In conjunction with X-ray diffraction studies, X-ray Photoelectron Spectroscopic (XPS) data can provide additional information about the nature of these composites. A high-resolution XPS spectrum of the Pt 4f and Sn 3d regions for the templated Pt-Sn catalyst is shown in Figure 7.3.

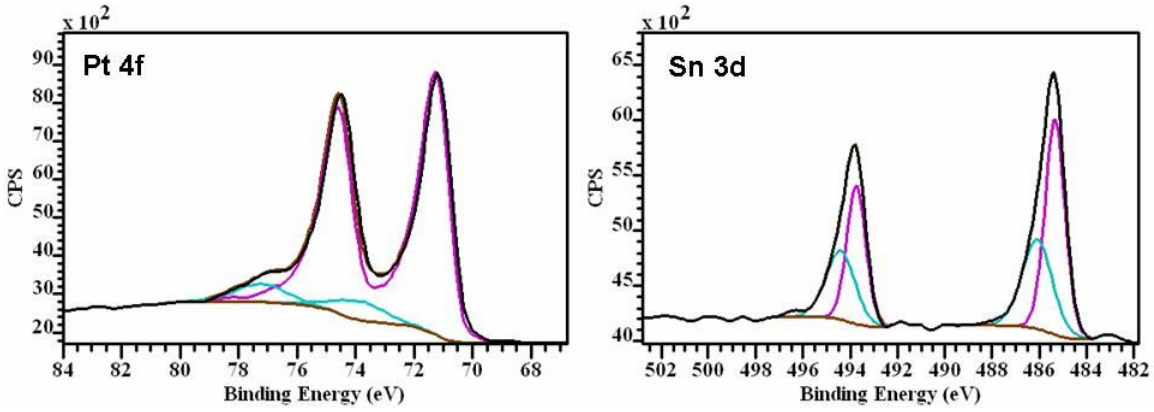

Figure 7.3: High resolution XPS spectra of the templated Pt-Sn catalyst for the Pt 4f (left) and the Sn 3d (right) regions.

The Pt 4f spectrum for the templated Pt-Sn sample was curve-fitted with the Pt peak acquired from the templated Pt sample that was processed in the same manner. Elemental quantification from XPS assign a 83 at.% Pt / 17 at.% Sn composition. The EDS measurements resulted in a 80 at.% Pt / 20 at.% Sn composition. This difference is within experimental error and indicates a compositional homogeneity in the bulk and the surface. The Sn 3d spectrum was curve-fitted with two peaks; the peak at 485.3 eV is associated with Sn in the metallic form and the peak at 486 eV corresponds to Sn in the oxide form (either SnO or SnO_2). The XPS data show a greater percentage of the tin to be in the metallic form (60%) compared to the amount of tin in the oxide form (40%). Of course, XPS is an ex-situ technique and it is well-known from Pourbaix diagrams (plots of potential vs. pH) for Sn that in the presence of alkaline electrolyte and under the range of potentials studied, tin will be in a highly oxidized form.

7.2 Anion-Exchange Ionomer

As described in Section 1.1.2, certain technical issues of stability such as carbonation of the alkaline electrolyte have prevented the alkaline fuel cell (AFC) from being a viable commercial power generator. A robust alkaline anion exchange membrane developed at Sandia National Laboratories has shown promising performance for KOH-free AFCs. The novel polymer consists of benzyl trimethylammonium groups on a poly(phenylene) backbone and is based on similar poly(phenylene) materials for PEM fuel cell applications [120].

Rotating-disc Electrode (RDE) studies incorporating nanostructured aerosol-derived catalysts in conjunction with the anion-exchange ionomer are the focus of this

work which pertains to the investigation of aerosol-derived nanostructured electrocatalysts. However, it should be noted that related membrane electrode assembly (MEA) studies integrating the same anion-exchange polymer in membrane form were undertaken. The effect of alternative anion-exchange ionomers in the catalyst ink on fuel cell performance was examined. The results of these studies are included in Chapter 9 – Appendix A. Certainly, fabrication of MEAs requires in-depth investigations into the integration of the ionomer within the catalyst ink to realize a completely solid-phase MEA.

7.2.1 Ionomer Preparation

The ionomer (Figure 7.4) was prepared by making a poly(phenylene) with pendant 4-methylphenyl groups and then converting an amount of the methyl groups to benzyl trimethylammonium groups.

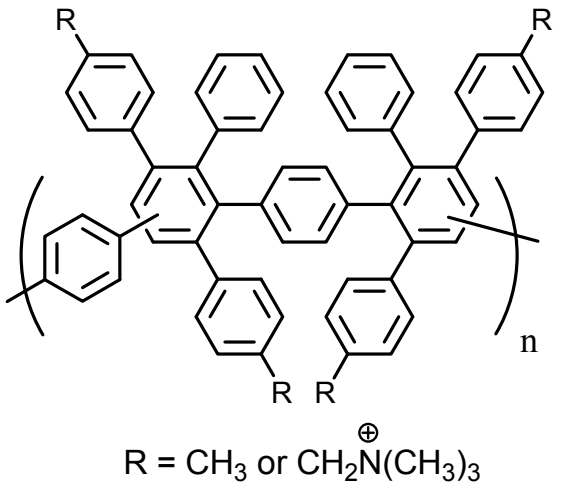

Figure 7.4: Structure of the repeat unit of the poly(phenylene) ionomer used in this study. About 52% of the R groups were methyls and the remainder were benzyl trimethylammonium groups.

As indicated in Figure 7.4, the repeat unit consists of four benzene rings with ambiguous regiochemistry (a mixture of meta and para linkages) on every other ring. In the parent polymer, each of the rings with ambiguous regiochemistry has one pendant phenyl group and two pendant 4-methylphenyl groups. To make the polymer used in this study, 48% of the methyl groups were converted to benzyl trimethylammonium groups.

For the rotating disc electrode (RDE) studies, the ionomer was dissolved in a mixture of ethanol and water to prepare the binder solution. For the membrane electrode assembly (MEA) studies, the ionomer was dissolved in chloroform and poured onto a casting plate. Upon evaporation of the chloroform, the resulting alkaline ionomer membrane can be used in the fabrication of an MEA.

7.3 Rotating Disc Electrode (RDE) Studies in Alkali

As described in Section 4.2.5, the established method of characterizing high-surface-area powder electrocatalysts in a RDE configuration includes the use of Nafion® to bind the catalyst to the glassy carbon RDE [101]. Nafion®, a cation exchange ionomer, is commonly used as a binder even in alkaline studies [63, 74, 121-124]. This is due to the fact that there is an absence of practical anion exchange ionomer alternatives. In acid, the presence of a cation exchange ionomer on the RDE facilitates the transport of protons at the catalyst surface, thereby promoting the reaction. It is hypothesized that in alkali, the presence of a cation exchange ionomer instead impedes the reaction by blocking active sites instead of facilitating ion transport. In alkali RDE studies, it is hypothesized that the presence of an anion exchange ionomer will facilitate the reaction by providing OH^- to the catalyst surface. Despite experimentally determining the minimal amount of

ionomer necessary to bind the catalyst, the effect of the binder will always be present due to these contributions or impediments.

In this work, the standard RDE methodology was adapted to alkaline media by attaching the catalyst powder to the glassy carbon electrode via an anion exchange polymer (ADAPP from Section 7.2) instead of Nafion®. An aqueous suspension of the catalyst powder samples were prepared and sonicated. A 6 μl aliquot of the catalyst solution was deposited onto a glassy carbon RDE and after drying, the anion exchange ionomer solution was deposited on top as a binder. This working electrode preparation procedure was repeated so that a fresh electrode was made for each measurement. The ionomer to electrocatalyst ratio (wt%) was altered while keeping the catalyst loading constant (60 ug/cm^2). Cyclic voltammograms (CVs) of the templated Pt-Sn catalyst in 1M ethanol / 1M KOH and the limiting ethanol oxidation current densities are shown in Figure 7.5.

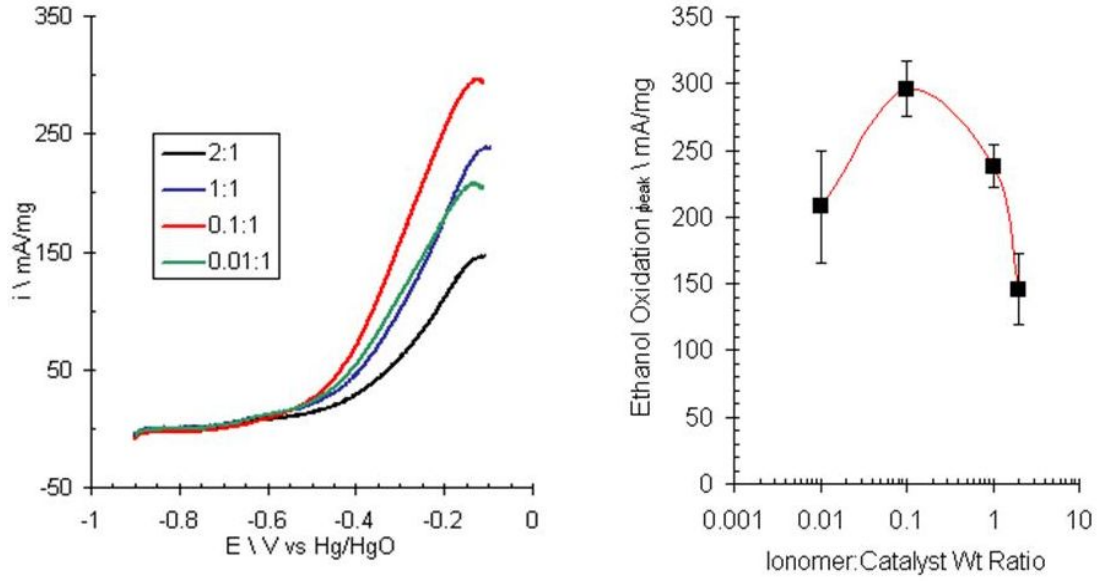

Figure 7.5: Cyclic voltammograms of templated Pt-Sn catalyst at different anion exchange ionomer:catalyst ratios in 1M KOH + 1M Ethanol, 10mV/s scan rate, 1600RPM (left) and the limiting ethanol oxidation current densities plotted vs. ionomer:catalyst ratio (right).

It is apparent from Figure 7.5 that the highest limiting current density for ethanol oxidation occurs at a 0.1:1 ionomer:catalyst ratio. At higher ionomer:catalyst ratios, the diminished current density is likely the result of increased transport hinderances of the reactant through the thicker ionomer film. At lower ionomer:catalyst ratios, the diminished current density is likely the result of catalyst detachment from the glassy carbon RDE due to insufficient ionomer present. The 0.1:1 ionomer:catalyst ratio was determined to be the optimal value and was then held constant for all subsequent measurements discussed here.

An interesting comparison is of the ethanol oxidation behavior of the same catalyst in combination with the commonly-used cation-exchange ionomer Nafion® on the RDE instead of the anion-exchange ionomer. The same procedure was performed for the cation exchange ionomer; the ionomer to electrocatalyst ratio (wt%) was altered while keeping the catalyst loading constant (60 ug/cm^2). Cyclic voltammograms (CVs) of the

templated Pt-Sn catalyst in conjunction with Nafion® and the limiting ethanol oxidation current densities are shown in Figure 7.6.

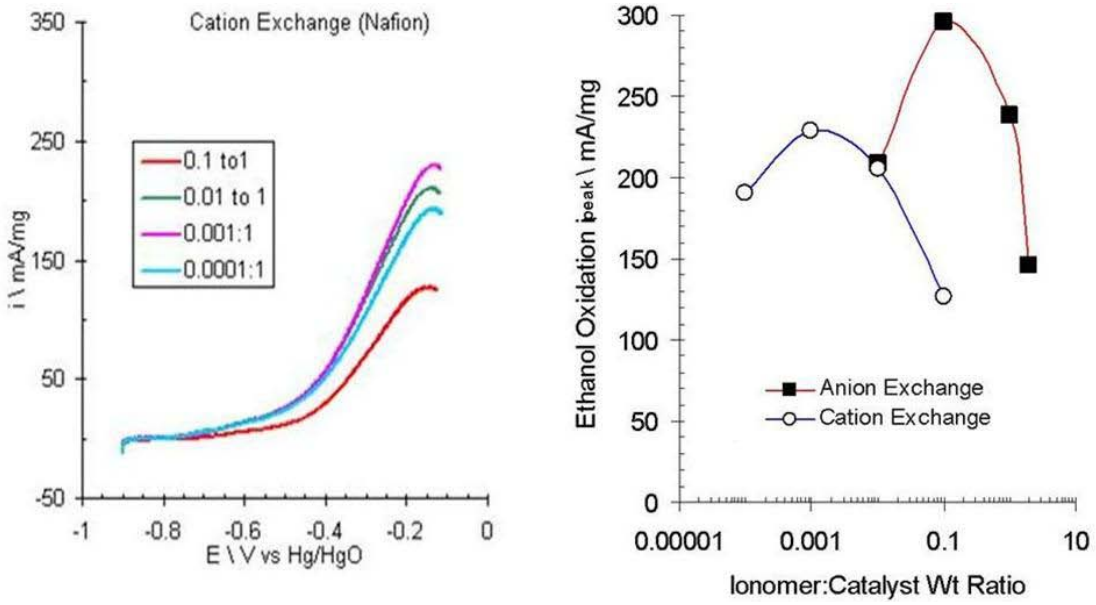

Figure 7.6: Cyclic voltammograms of templated Pt-Sn catalyst at different cation exchange ionomer:catalyst ratios in 1M KOH + 1M Ethanol, 10mV/s scan rate (left) and the limiting ethanol oxidation current densities plotted vs. ionomer:catalyst ratio for both the anion and cation exchange ionomers (right).

It is apparent from Figure 7.6 that the highest ethanol oxidation peak current density is measured with the anion exchange ionomer. The highest ethanol oxidation peak current density for the RDE incorporating the cation exchange ionomer occurs at a 0.001:1 ionomer:catalyst ratio. This value is two orders of magnitude less than that for the anion exchange ionomer. Considering the relative ionomer densities (2.0 g/cm^3 for the cation-exchange ionomer and 1.4 g/cm^3 for the anion-exchange ionomer), one discovers that higher current densities are achieved despite having an order of magnitude thicker ionomer film. The anion exchange ionomer facilitates hydroxyl transport, demonstrating the tremendous significance of ion transport at the catalyst surface.

These studies present a unique investigation of anion exchange ionomers as entrapment materials for RDE studies in alkali. This methodology is used to evaluate templated electrocatalysts for ethanol oxidation reactivity in alkaline media.

7.3.1 Ethanol Electro-oxidation Behavior

Using the anion exchange ionomer-modified RDE methodology, the ethanol oxidation behavior of templated Pt and Pt-Sn catalysts was examined. Initially, three aerosol-derived templated Pt-Sn electrocatalysts with varying compositions were screened for ethanol oxidation in alkaline media. Cyclic voltammograms of the templated Pt and the templated Pt-Sn catalysts with nominal Pt:Sn compositions ranging from 12-29% Sn (as determined by EDS) are shown in Figure 7.7.

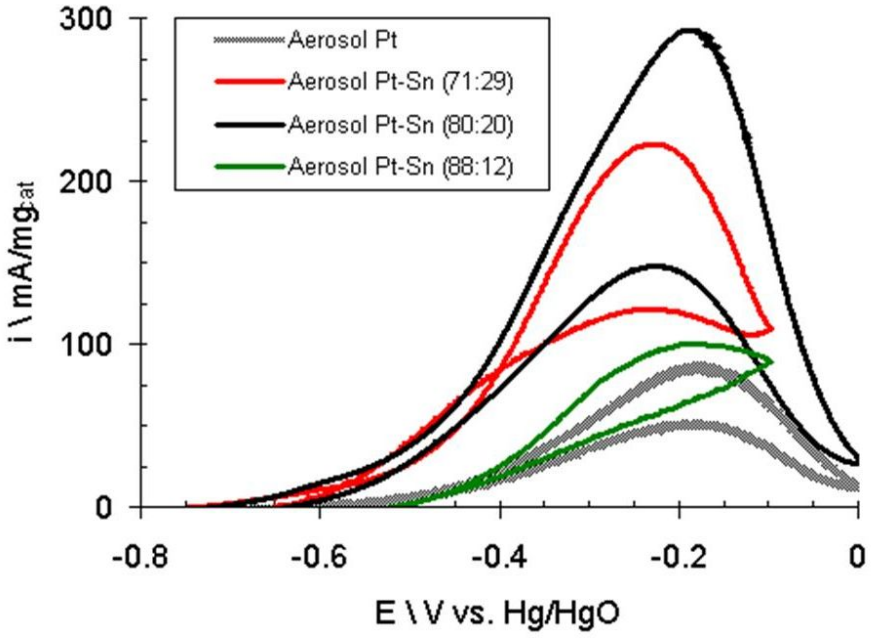

Figure 7.7: Linear sweep cyclic voltammograms for ethanol oxidation in 1M KOH + 1M Ethanol and 10 mV/s scan rate and 1600 RPM at 25°C. The plots compare the mass-specific current density of four aerosol-derived templated electrocatalysts with varying compositions.

The aerosol Pt-Sn (80:20) electrocatalyst shows the greatest overall performance for ethanol oxidation in comparison to the other aerosol-derived templated electrocatalysts evaluated. The aerosol Pt-Sn (80:20) electrocatalyst exhibits the highest peak current density in addition to a lower onset potential for ethanol oxidation. As a result of these investigations, the aerosol-derived templated Pt-Sn (80:20) catalyst is used to further analyze the effect of Sn by comparing it to the aerosol-derived template Pt sample. The aerosol Pt-Sn (80:20) catalyst is thus referred to the templated Pt-Sn sample in the following studies. Cyclic voltammograms of the templated Pt and Pt-Sn electrocatalysts in 1M KOH and 1M Ethanol at 25°C, 40°C and 55°C are shown in Figure 7.8.

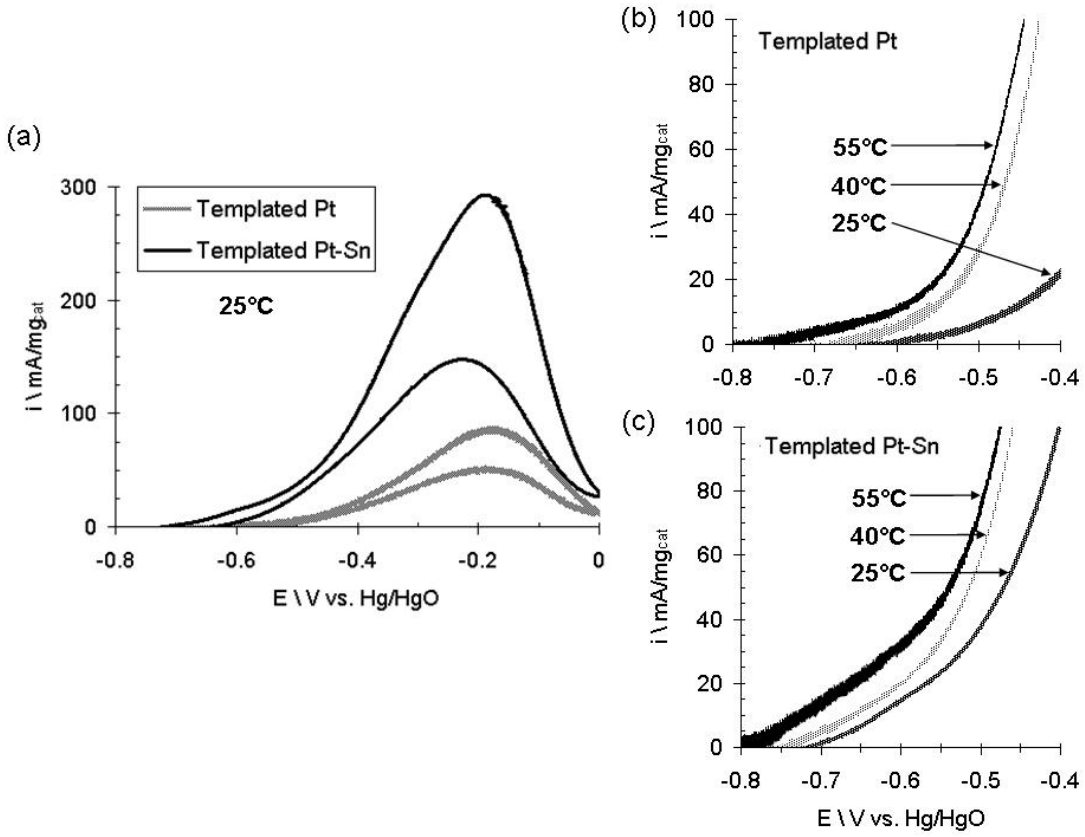

Figure 7.8: Linear sweep cyclic voltammograms for ethanol oxidation in 1M KOH + 1M Ethanol and 10 mV/s scan rate and 1600 RPM. (a) Comparison of templated Pt and Pt-Sn at 25ºC. (b) Templated Pt and (c) templated Pt-Sn at 25 ºC, 40 ºC and 55 ºC.

It is evident from the CVs in Figure 7.8 that the templated Pt-Sn electrocatalyst shows superior performance for ethanol oxidation in alkaline media than the templated Pt electrocatalyst. In Figure 7.8(a), the oxidation onset potential for the Pt-Sn catalyst (ca. -0.75V) is shifted approximately 150 mV more negative than that for the Pt catalyst (ca. -0.6 V). In addition, the peak oxidation current for the Pt-Sn catalyst is about three times that of the Pt catalyst. The oxidation current densities shift to more negative potentials with increasing temperature; this effect can be observed for both the templated Pt and Pt-Sn electrocatalysts in Figure 7.8(b) and Figure 7.8(c), respectively.

7.3.2 Potentiostatic measurements

Potentiostatic measurements provide short-term steady-state current densities and are more closely related to realistic fuel cell operating conditions. Therefore, the performance of the templated Pt and templated Pt-Sn catalysts for ethanol, methanol and CO oxidation in alkaline media was principally studied by short-term steady-state current densities at constant potential. Chronoamperometric measurements were made for both the Pt and Pt-Sn (80:20) catalysts for ethanol, methanol and CO oxidation at 25 ºC, 40 ºC and 55 ºC. Figure 7.9 shows typical chronoamperometric curves which were measured in 1M KOH and 1M ethanol at 55 ºC.

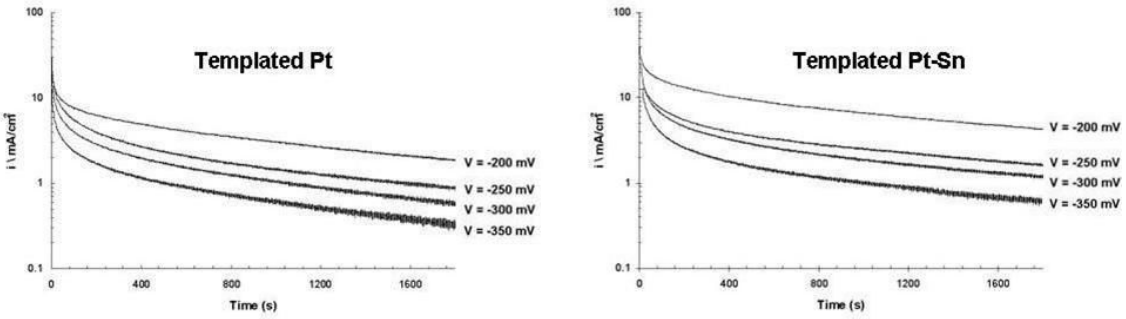

Figure 7.9: Chronoamperometric curves for ethanol oxidation in 1M KOH + 1M ethanol at 55 ºC and 1600 RPM. The potential was held at -200mV, -250mV, -300mV and -350mV vs. Hg/HgO for both the templated Pt (left) and templated Pt-Sn (right) electrocatalysts. The current density is reported on a logarithmic scale.

The initial high current density which is mainly due to the double layer charging process decays to a relatively stable equilibrium current density after 30 minutes. For analysis here, the current density after 15 minutes is used for comparison to reduce the data set but this does not diminish the information that can be gained from this study. The short-term mass-specific steady-state current density values of the templated Pt and Pt-Sn catalysts in 1M KOH and 1M ethanol at 25 ºC, 40 ºC and 55 ºC are plotted versus each corresponding constant potential in Figure 7.10.

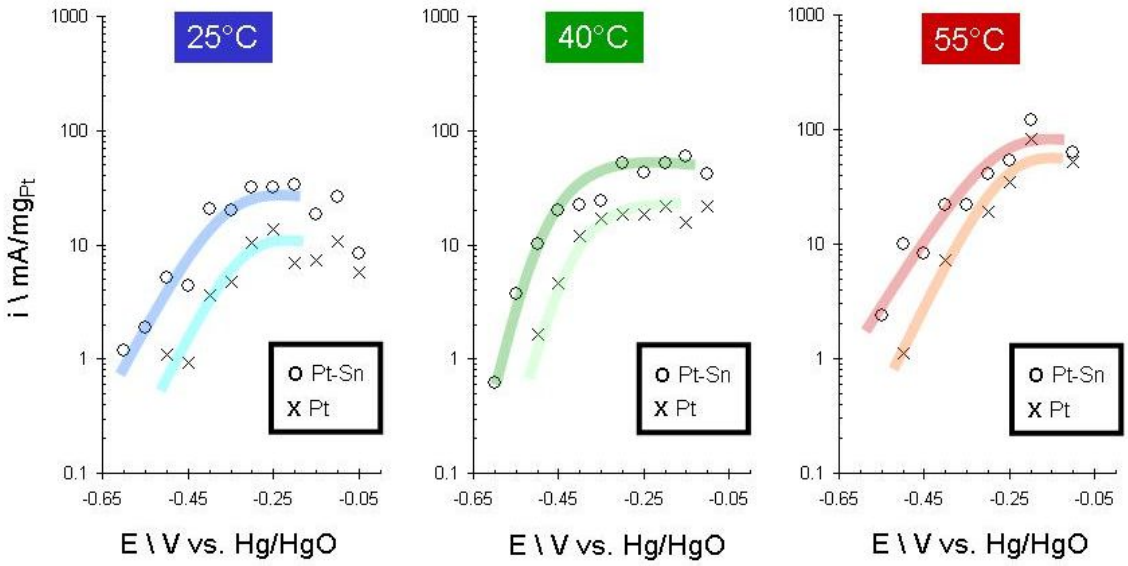

Figure 7.10: Short-term steady-state current densities plotted versus potential held during the chronoamperometric measurements. The plots compare the templated Pt and Pt-Sn catalysts in 1M KOH + 1M ethanol at 25 ºC, 40 ºC and 55 ºC.

It is evident from Figure 7.10 that the short-term steady-state current densities for the templated Pt-Sn catalyst are generally always higher than those for the templated Pt catalyst, regardless of temperature or applied potential. The addition of Sn to Pt could enhance the oxidation of adsorbed intermediates like CO in a similar way as the addition of Ru improves CO oxidation in both acid and alkaline media. For both Pt and Pt-Sn, an increase in temperature results in an increase in peak current density for a given potential. Similar trends are observed for the case of methanol oxidation in alkaline media.

Interestingly, in the case of CO oxidation, an increase in temperature does not necessarily result in an increase in current density as in the case of ethanol. The short-term steady-state current densities for CO electro-oxidation which were performed in CO-saturated 1M KOH are shown in Figure 7.11.

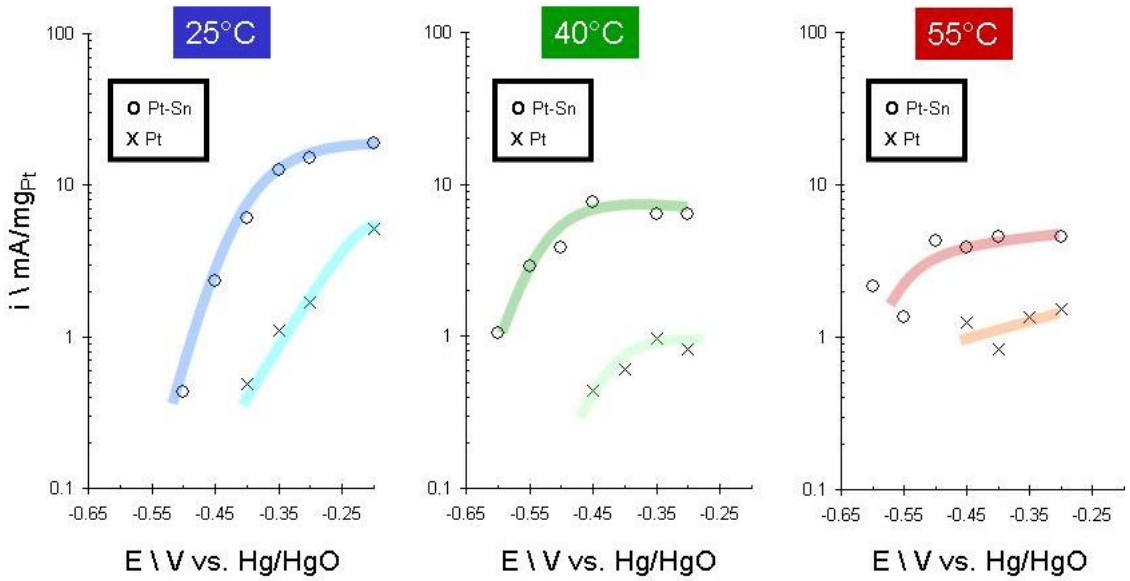

Figure 7.11: Short-term steady-state current densities plotted versus potential held during the chronoamperometric measurements. The plots compare the templated Pt and Pt-Sn catalysts in CO-saturated 1M KOH at 25 ºC, 40 ºC and 55 ºC.

In fact, an increase in temperature results in a decrease in CO oxidation current density. This is especially apparent at higher potentials and for the templated Pt-Sn catalyst. Although the solubility and diffusivity of CO are temperature dependent in aqueous electrolytes, previous investigations have shown that the increase in CO diffusivity with temperature is compensated by the decrease in CO solubility[125]. This observation of decreased CO oxidation current density with increased temperature is investigated further by potentiodynamic measurements in Section 7.3.3.

In this work, the similarities and differences of templated Pt and Pt-Sn catalysts for ethanol and carbon monoxide oxidation in alkali provide an opportunity to investigate the nature of the processes involved during reaction. As stated in Section 2.5.2, previous in-situ infrared spectroscopic studies have shown adsorbed CO is the main poisoning species during ethanol oxidation by Pt in alkaline media. Figure 7.12 compares the current densities for ethanol and carbon monoxide electro-oxidation by templated Pt and

Pt-Sn catalysts at three different temperatures. Note that the short term steady-state mass-specific current densities are in logarithmic scale.

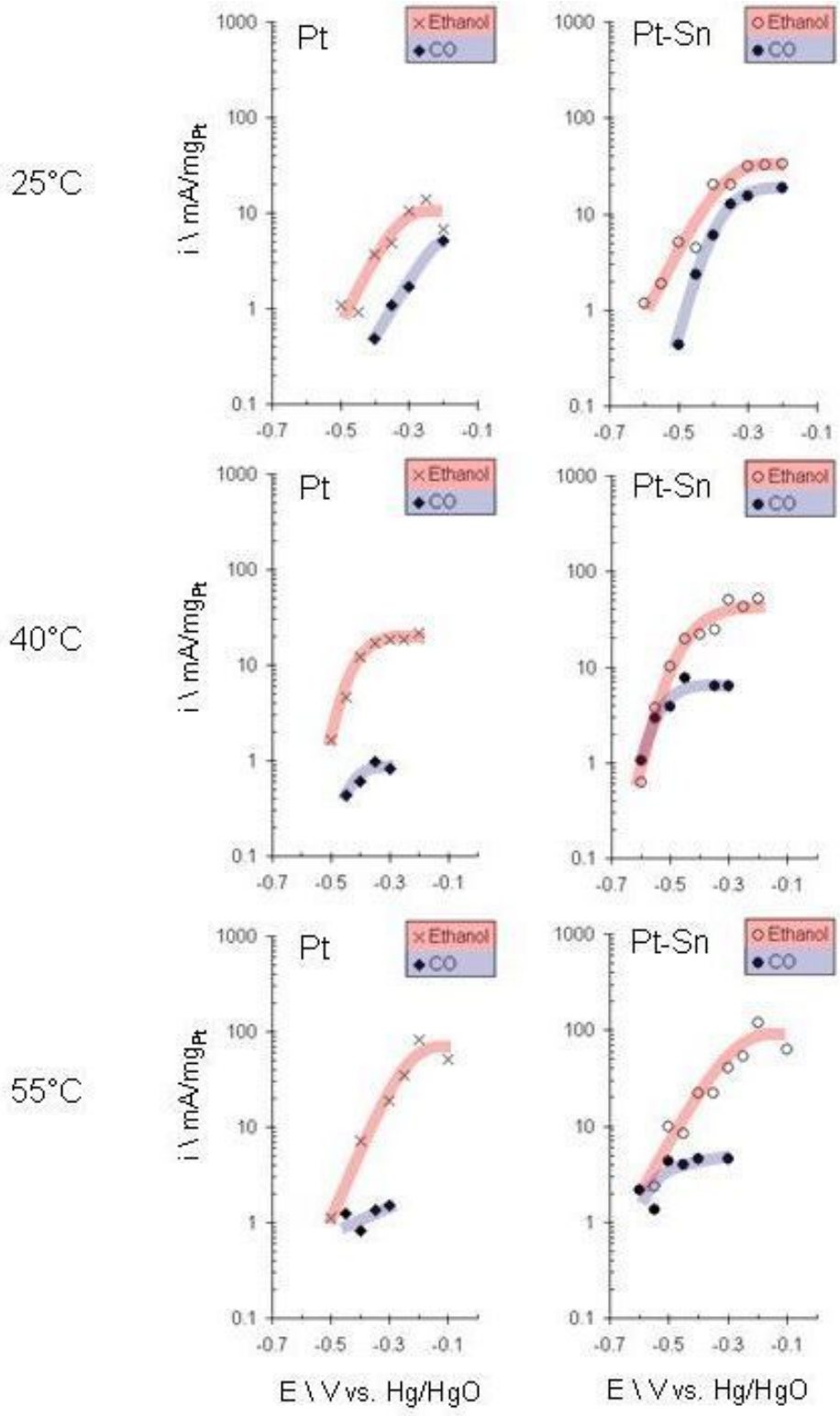

Figure 7.12: Short-term steady-state current densities plotted versus applied potential during chronoamperometric measurements. The plots compare the templated Pt (left) and Pt-Sn (right) catalysts in CO-saturated 1M KOH (blue) and 1M ethanol + 1M KOH (red) at 25 ºC, 40 ºC and 55 ºC. The mass-specific current density is reported on a logarithmic scale.

It is apparent from Figure 7.12 that the most notable difference between Pt and Pt-Sn is the CO oxidation behavior. The beneficial effect of Sn in the Pt-Sn catalyst is evident in that the current densities at low potentials are orders of magnitude higher than for the Pt catalyst. At low temperature (25ºC in Figure 7.12), the CO oxidation current densities closely follow the ethanol oxidation current densities for both the templated Pt and Pt-Sn. At 40ºC, the Pt-Sn CO oxidation current densities differ from Pt in that they again closely follow those for ethanol oxidation until about -400mV vs. Hg/HgO at which point a plateau is reached. At 55ºC, however, the CO oxidation current densities are much lower in comparison to the ethanol oxidation current densities. It has been asserted that for ethanol oxidation by Pt-Sn in acidic media, the oxidation of adsorbed CO and CH_3CO species determines the reaction rate at low temperatures and/or low current densities[67]. It is believed that the presence of tin oxides enhances the oxidation of ethanol because it enhances the oxidation of adsorbed intermediates. In the present studies in alkaline media, similar phenomena are observed. At low temperature, the rates of CO oxidation are close the rates of ethanol. However, at high temperature, the rate of CO oxidation is significantly lower than the rate of ethanol oxidation.

The point at which the ethanol oxidation current densities reach a plateau for the Pt and the Pt-Sn catalyst are most different at the lower temperature. At low temperatures, the ethanol oxidation rate for the Pt-Sn catalyst is significantly higher than that for the Pt catalyst. At higher temperatures, the difference in the ethanol oxidation rates between the Pt and Pt-Sn catalysts becomes negligible. In other words, the Pt

catalyst exhibits the greatest increase of ethanol oxidation current with temperature and likely has a larger activation energy than the Pt-Sn catalyst.

In these studies, the exact activation energy (E_a) cannot be calculated because there are competing processes occurring with an increase in temperature. In particular, the oxide formation process will likely change the apparent activation energy. A review on apparent activation energies for methanol electro-oxidation by Pt in acid and alkaline media has publicized the fact that there is a wide range in published values from 24-86 kJ/mol as overviewed in [40]. The proposed reasons for these conflicting values are the effects of surface poisoning intermediates and oxide formation. The extent of the contributions of variable surface coverage to the apparent activation energy is potential and temperature dependent. The review [40] states that in light of these complications, the activation energy calculated at the potential of peak current should be considered as indicative of the *apparent activation energy* and can be used in estimations and calculations for design. It can be assumed that at this potential, the catalyst surface has the optimum oxide coverage to achieve maximum current, and thus can be used to compare different catalysts (such as here Pt and Pt-Sn). However, the effect of the change in oxide coverage with temperature is still a contributive factor in the value of the apparent activation energy.

The relative apparent activation energies between the templated Pt and Pt-Sn catalysts were calculated from the peak current densities at -0.2V vs. Hg/HgO. The Arrhenius plots are shown in Figure 7.13.

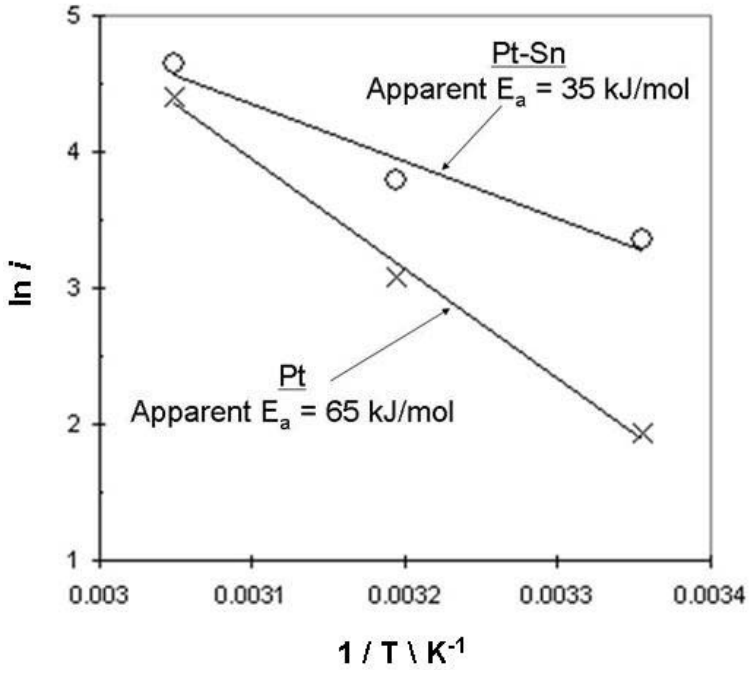

Figure 7.13: Arrhenius plots for Pt and Pt-Sn electrocatalysts in alkaline solution from peak ethanol oxidation current densities (mA/mg_{cat}). The apparent activation energies are 65 kJ/mol and 35 kJ/mol for the Pt and Pt-Sn catalysts, respectively.

The plots in Figure 7.13 indicate that the Pt catalyst has a larger activation energy than the Pt-Sn catalyst under the same conditions. The relative apparent activations energies indicates that the rate of reaction on the Pt catalyst is more temperature-sensitive compared to the Pt-Sn catalyst. The implication of this trend is discussed further in Section 7.3.5.

7.3.3 CO Electro-oxidation Behavior

Additional potentiodynamic experiments were performed to investigate the effect of temperature on the electro-oxidation of carbon monoxide in alkaline media. The simplest experiment is to compare the CO oxidation behavior by cyclic voltammetry at

various temperatures. The cyclic voltammograms (CVs) of the Pt-Sn catalyst in CO-saturated 1M KOH are shown in Figure 7.14.

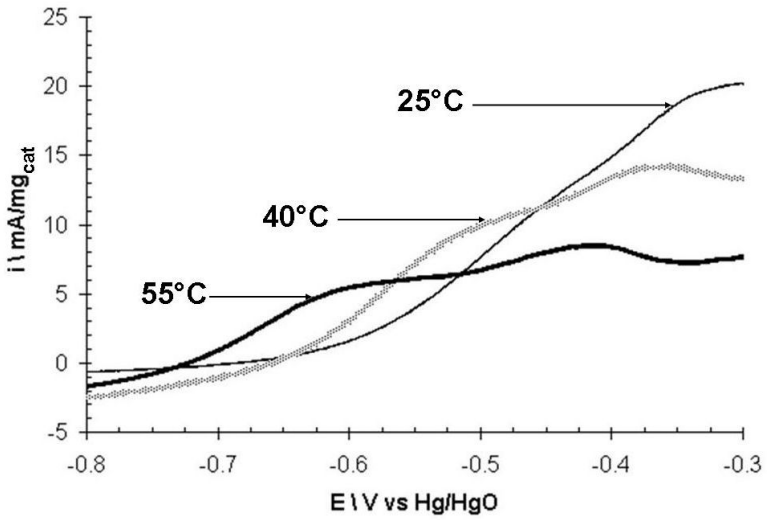

Figure 7.14: Cyclic Voltammograms of the Pt-Sn electrocatalyst in CO-saturated 1MKOH at 25°C, 40°C and 55°C, 10 mV/s scan rate and 1600RPM.

Two main observations from Figure 7.14 reveal the complex CO oxidation behavior with temperature. First, the onset potential for CO oxidation is shifted negatively (ca. 50 mV for every 15°C). This observation suggests that the oxidation of CO is an activated process which is in agreement with a CO oxidation study on Pt single crystals in alkaline media at two temperatures[95]. Secondly, the peak oxidation current decreases with temperature (ca. 5 mA/mg for every 15°C) which is similar to that which is observed from the potentiostatic measurements in this work. The explanation for this phenomenon is assisted by additional investigation of oxidation of pre-adsorbed CO.

Voltammetric oxidation of pre-adsorbed CO offers an opportunity to study the oxidation of CO_{ad} while eliminating the effects of continuous CO adsorption from the solution. First, adsorption of CO is achieved by immersing the working electrode in a

CO-saturated electrolyte while the electrode potential is held just above the hydrogen adsorption/desorption region (in this case at -0.5 V vs Hg/HgO). After adsorption, CO is purged from the solution by bubbling gaseous nitrogen while the potential is continuously held. The potential is then swept negatively to -0.9V vs. Hg/HgO and then positively to 0V vs Hg/HgO. A "CO stripping" peak is observed during the positive going sweep and is due to the oxidation of the pre-adsorbed CO. The resulting voltammograms from these studies are shown in Figure 7.15. for both the templated Pt and Pt-Sn catalysts.

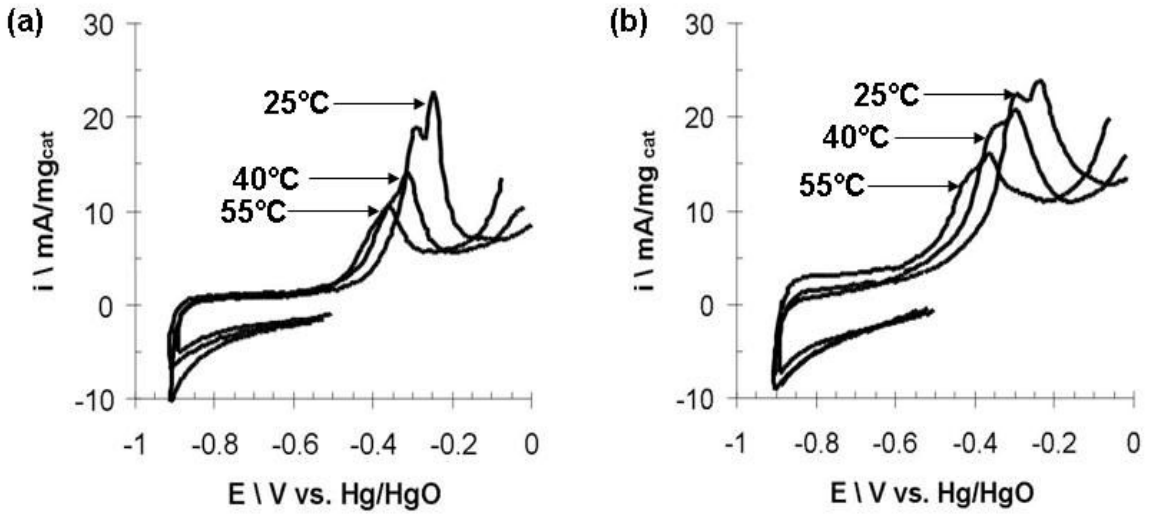

Figure 7.15: Voltammetric oxidation of adsorbed CO in 1M KOH solution at 25 ºC, 40 ºC and 55 ºC (temperatures in bold font) and background cyclic voltammograms in 1M KOH at 25 ºC, 40 ºC and 55 ºC (temperatures in italic font) (a) on templated Pt catalyst and (b) on templated Pt-Sn catalyst.

The CO stripping peak potential in Figure 7.15 decreases with increasing temperature (ca. 50 mV between each 15ºC shift). This suggests that the higher temperatures activate the CO oxidation process presumably due to enhanced mobility of CO_{ad} and an increase in activity of oxygenated species[67]. In addition, the CO stripping peak potentials for the Pt-Sn catalyst are lower (ca. 100 mV) in comparison to the Pt

catalyst which indicates that the addition of tin improves the capability to remove adsorbed CO.

For both the templated Pt and Pt-Sn catalysts, the anodic charge decreases with increasing temperature. The exposed metal area should not change as a function of temperature. It appears that with increasing temperature, the decrease in anodic charge can be attributed to a lower CO_{ads} coverage. A similar phenomenon of decreasing anodic charge with increasing temperature was observed for Pt-Ru/C in acidic media. In the same study, however, Pt/C did not exhibit this behavior; instead the anodic charge was constant for all temperatures. This trend was explained by an increased electrocatalytic activity of Ru at the CO adsorption potential used[126]. In this study however, the anodic charge decreases with increasing temperature for Pt in the same way as with Pt-Sn. The major difference is that this study is conducted in alkaline media. In contrast to acidic media, Pt can be considered oxophilic in alkali. CO may be prevented from building up because OH^- adsorption in alkaline media occurs at low potentials. The lack of adsorption of weakly-bound CO_{ad} at higher temperatures may result from an oxidative change in the surface such as a higher OH_{ad} coverage. It has been proposed that CO coverage might change with temperature in alkaline media although there have not been previous studies in the literature to assist in this determination as stated in a recent review[40]. It is evident in this present work that this is in fact the case.

. Peak splitting during oxidation of pre-adsorbed CO in alkaline media has previously been observed and may possibly be attributed to two alternate mechanisms; the first peak at lower potential may be due to attack by solution-phase OH^- representing a Eley-Rideal mechanism or a non-competitive Langmuir-Hinshelwood type mechanism

between and an oxygen containing species and the second at higher potential may be due to Langmuir-Hinshelwood mechanism between CO_{ad} and OH_{ad} [96, 97, 127].

7.3.4 Behavior in Absence of Reacting Species

The possibility that lower CO_{ad} concentrations at higher temperatures is the result of an oxidative change in the surface can be further investigated by performing background cyclic voltammetric studies. These are performed in nitrogen-saturated 1M KOH without the presence of reacting species. The background cyclic voltammograms are shown in Figure 7.16 for the templated Pt and Pt-Sn catalysts.

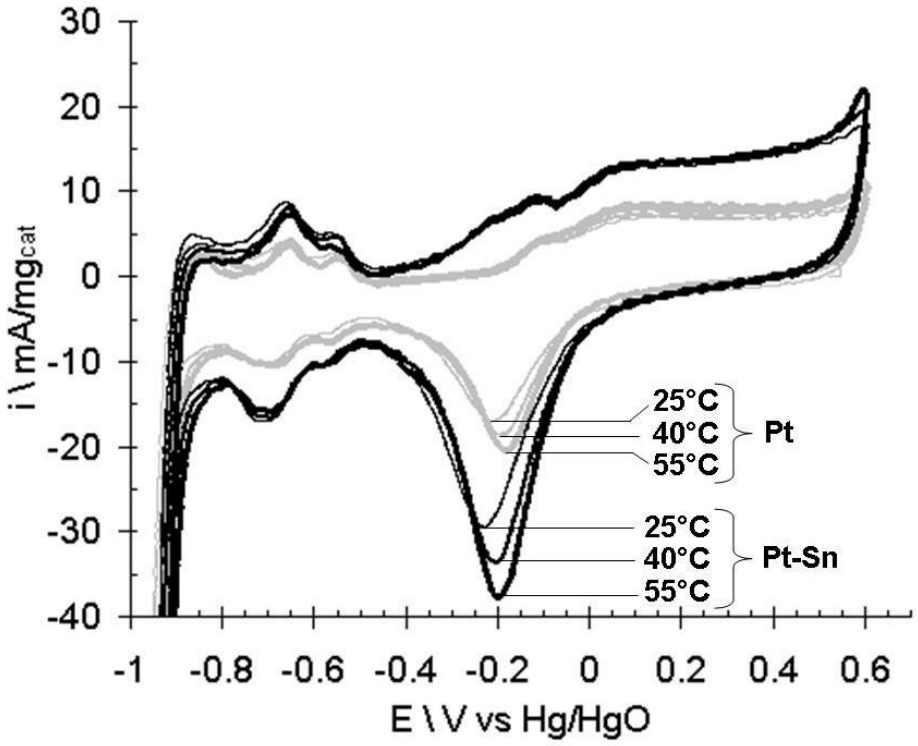

Figure 7.16: Background linear sweep voltammograms of aerosol-derived templated Pt and Pt-Sn in nitrogen-saturated 1M KOH electrolyte solution at 10 mV/s scan rate and 1600 RPM rotation rate at 25 ºC, 40 ºC and 55 ºC.

The characteristic shapes of the background cyclic voltamograms for Pt in alkaline electrolyte in Figure 7.16 are similar to previous observations of polycrystalline Pt electrodes[40, 128, 129]. The hydrogen adsorption/desorption region or "butterfly" region occurs between -0.8V and -0.5V vs. Hg/HgO. This region is immediately followed by the reversible OH^- anion adsorption region occurring up to ca. -0.1 V vs. Hg/HgO. Above this potential, irreversible oxide formation occurs. As observable in Figure 7.16, the magnitude of the reversible oxide reduction peak (ca. -0.2 V vs. Hg/HgO), which is directly related to the amount of oxide formed during the anodic sweep, significantly increases with temperature. The increase of surface oxide formation increases with temperature for both the Pt and Pt-Sn samples. The background scans for Pt-Sn in comparison to Pt exhibit a greater charging current which is most likely due to a larger specific capacitance due to tin oxides given that the BET surface areas of the two materials are nearly identical.

7.3.5 Discussion

The beneficial effect of Sn addition to Pt has been shown for the oxidation of small organic molecules in alkaline media. The use of an anion exchange ionomer in these studies provides a unique opportunity to study the electro-oxidation of ethanol in alkaline media. Commonly, it is necessary to use the cation exchange ionomer Nafion to bind powder electrocatalysts catalysts to the glassy carbon working electrode in the RDE configuration, however in these studies, an anion exchange ionomer allows for a fully alkali study wherein hydroxyl transport to the catalyst surface is facilitated by the anion

exchange ionomer. A Tafel plot of the Aerosol Pt and Pt-Sn electrocatalysts for ethanol oxidation in alkaline media is shown in Figure 7.17.

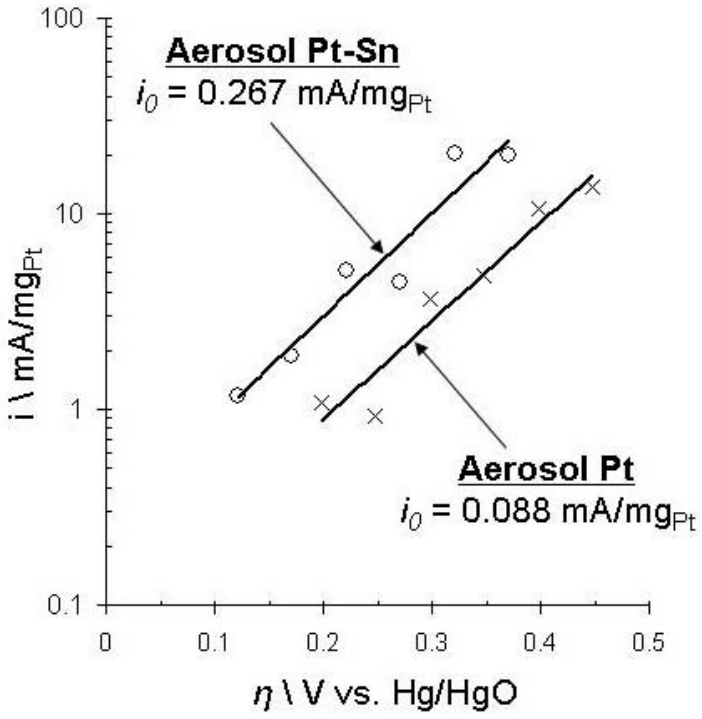

Figure 7.17: Tafel plot (mass-specific current density vs. overpotential η) for aerosol Pt and aerosol Pt-Sn electrocatalysts from chronoamperometric measurementrs in 1M KOH / 1M ethanol at 25°C. The exchange current density i_0 is 0.088 mA/mg$_{Pt}$ and 0.267 mA/mg$_{Pt}$ for the aerosol-derived Pt and Pt-Sn catalysts, respectively.

It is evident from the Tafel plot in Figure 7.17 that the calculated exchange current density i_0 for the Pt-Sn catalyst is significantly greater than for the aerosol Pt catalyst. This data indicates the Pt-Sn catalyst has a higher activity for ethanol oxidation in alkaline media than the Pt catalyst.

It has been shown that the anodic charge decreases with increasing temperature for the voltammetric oxidation of adsorbed CO. With increasing temperature, the decrease in anodic charge is attributed to a lower CO_{ad} coverage. In this case, CO may be

prevented from building up because at higher temperatures, the OH_{ad} surface coverage increases, thus blocking sites and acting as a poison.

The kinetics of ethanol electro-oxidation in alkaline media is probably determined in part by a balance between the rate of ethanol dehydrogenation on multi-fold Pt sites (Equation 7-1) and the rate of a Langmuir-Hinshelwood type reaction between the adsorbed dehydrogenated products and the oxygen-containing species represented by OH_{ad} (Equation 7-2).

$$CH_3CH_2OH \begin{cases} \rightarrow CH_3CH_2O_{ad} \\ \rightarrow CO_{ad} \end{cases} \quad \textbf{(7-1)}$$

$$CO_{ad} + 2OH_{ad} \rightarrow CO_2 + H_2O \quad \textbf{(7-2)}$$

The Langmuir-Hinshelwood reaction rate in Equation 7-2 will be determined by the reactant coverages and the probability of interaction which is dependent on surface diffusion of the adsorbed carbonaceous intermediates[49, 95, 98]. Disturbing the surface coverage balance of the adsorbed carbonaceous intermediates and the oxygen-containing species will have an inhibiting effect on the overall reaction.

For CO oxidation, a higher temperature shifts the balance of surface coverage; the surface becomes more oxidized at higher temperatures, thus blocking sites for CO adsorption. This is made very clear by the extreme decrease in CO oxidation peak reaction rates at higher temperatures in addition to the reduced CO stripping anodic charge at higher temperatures. For the case of ethanol electro-oxidation, the effect of temperature is not so obvious. The peak ethanol reaction rates do not severely decrease with temperature as in the case of CO oxidation. However, the relative behavior of the Pt

and Pt-Sn catalysts with temperature allude to the consequences of temperature-enhanced surface oxide coverage.

A partial analogy can be drawn in regards to the activation processes between ethanol and methanol. It has been observed in this work as well as in the literature that methanol oxidation in alkaline media is an activated process explained in part by temperature-activated methanol adsorption/dehydrogenation[40]. Similarly in the case of ethanol oxidation, an increase in temperature likely results in an increase in the ethanol adsorption/dehydrogenation rate (Equation 7-1). This increases the coverage of adsorbed intermediates on Pt sites. Accordingly, a higher coverage of adsorbed intermediates will decrease their adsorption energy due to repulsive interactions, thus becoming more weakly bound and more reactive. Although a higher temperature leads to an increase in carbonaceous intermediate reactant coverage (Equation 7-2), the higher temperature leads to an increase in the coverage of oxygen containing species which presents the problem of competition for Pt adsorption sites. At low temperature, the availability of Pt adsorption sites for ethanol adsorption/dehydrogenation is greater because the surface is less oxidized. At low temperature (25°C), one observes from the data in Figure 7.12 that the Pt-Sn catalyst has a significantly higher reaction rate than Pt, demonstrating the promoter effect of Sn for OH^- adsorption. Therefore, the presence of Sn compensates for the lower oxide coverage on Pt sites by donating the oxygen-containing species for further oxidation of the carbonaceous intermediates. Alternatively, at a higher temperature (55°C), the ethanol oxidation reaction rates are more similar for the Pt and Pt-Sn catalysts as observed in Figure 7.12. In this case, the availability of Pt adsorption sites for ethanol dehydrogenation is lower for both catalysts due to the poisoning effect of

the higher OH_{ad} coverage with higher temperature. Therefore, the presence of Sn for donation of oxygen containing species becomes irrelevant because both catalysts suffer from an oxide "poisoned" surface.

The apparent activation energy is higher for the Pt catalyst in comparison to the Pt-Sn catalyst which reveals that the rate of reaction on the Pt catalyst is more temperature-sensitive compared to the Pt-Sn catalyst. This result highlights the important effect of increased oxide coverage with increased temperature. The increase in oxide coverage with temperature for the Pt catalyst will have a greater effect in comparison to the Pt-Sn catalyst. In comparison to the Pt catalyst, the Pt-Sn catalyst has a greater OH_{ad} surface coverage supplied by the Sn at lower temperature and therefore the effect of increased oxide coverage with temperature is not as pronounced.

8 Conclusions

The principal objective of this work was to develop a method for synthesizing nanostructured electrocatalysts wherein the structural effects could be examined as a result of a morphology that permeated the entire sample. Bulk templating methods for both Pt/C and Pt-Ru composites have been evaluated in this study as well as commonly in the literature. These bulk templating synthesis techniques are limited due to the fact that the nanostructure does not exist throughout the entire sample. Therefore, accurate examinations of structural effects were previously impossible. The aerosol-based templating technique developed in this work has been shown to be a practical method for the synthesis of nanostructured electrocatalysts and can be conveniently modified to synthesize electrocatalysts of different compositional character.

The method of synthesizing Pt-Ru electrocatalysts was applied to the development of Pt-Sn electrocatalysts. Nanostructured Pt-Sn electrocatalysts were evaluated in a unique approach tailored to electrocatalytic studies in alkaline media. These studies present an initiation investigation of anion exchange ionomers as entrapment materials for RDE studies in alkali. Their significance is linked to the development of membrane electrode assemblies (MEAs) with the same ionomer for a KOH-free alkaline fuel cell (AFC).

At low temperatures, the presence of Sn was found to significantly enhance the ethanol oxidation rate. At higher temperatures, the peak ethanol oxidation rates between the Pt and Pt-Sn catalysts became very similar. This suggests that at higher temperatures, the oxygen-containing species contribution provided by the tin is insignificant due to a more oxidized Pt surface at the higher temperature. The importance of the surface

coverage of oxygen-containing species in the reaction mechanism became apparent with supplementary studies of short-term steady-state ethanol and CO oxidation experiments.

8.1 Future Outlook

The plots in Figure 8.1 provide a broader perspective on oxidation of small organic molecules in alkali and illustrate the distinctive characteristics of ethanol, methanol and CO oxidation by Pt and Pt-Sn from the relative limiting current densities.

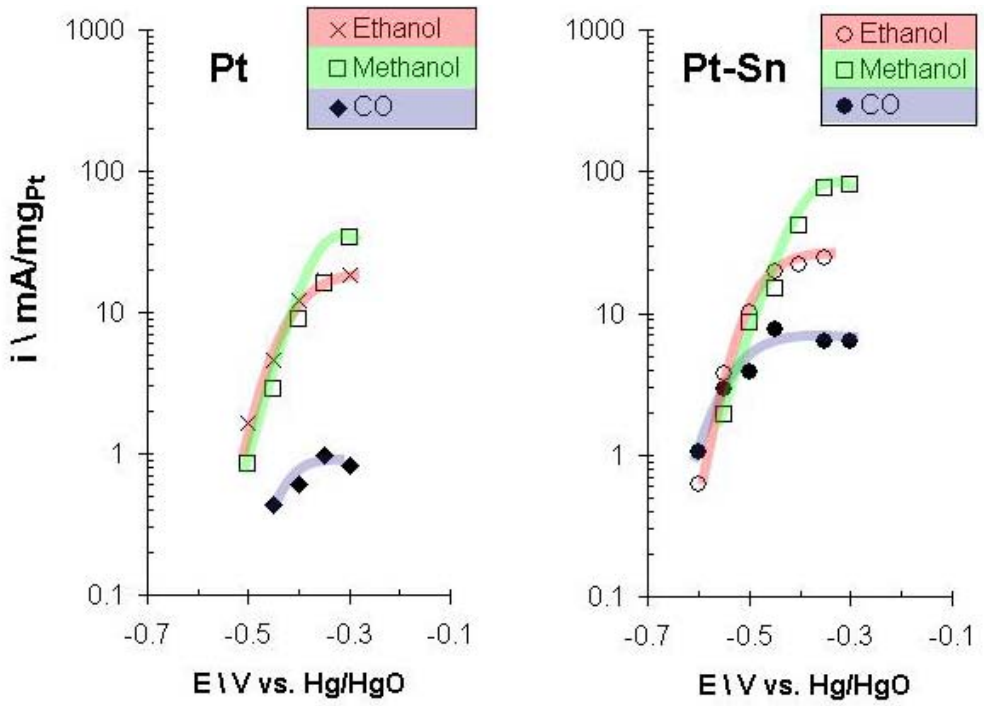

Figure 8.1: Short-term steady-state current densities plotted versus applied potential during chronoamperometric measurements. The plots compare the templated Pt (left) and Pt-Sn (right) catalysts in 1M ethanol + 1M KOH, 1M methanol + 1M KOH or CO-saturated 1M KOH at 40ºC. The current density is reported on a logarithmic scale.

The limiting current density sequence (methanol > ethanol > CO) demonstrates the specific challenges of oxidizing each particular organic molecule and indicates the

importance of the C-C bond scission. In particular, tuning the ideal ethanol oxidation electrocatalyst for C-C bond breakage is of great importance, not just enhanced oxidation of CO-like species which is most likely provided by the addition of Sn.

The most advantageous ethanol oxidation electrocatalyst should also possess enhanced C-C bond cleavage properties for complete oxidation to CO_2 and minimal production of two carbon species (acetaldehyde, acetic acid). The C-C bond scission for ethanol electro-oxidation presents the principal catalyst development challenge. Ternary electrocatalysts present interesting systems, for example Pt-Sn-M where the third metal promotes C-C bond cleavage. Preliminary in-situ FTIR studies have shown the addition of Rh to Pt reduces the amount of acetaldehyde produced apparently promoting C-C bond scission [130, 131]. Very recently, a ternary Pt-Sn-Rh electrocatalyst has been shown to exhibit higher activity for ethanol electro-oxidation than binary Pt-Sn[132].

Relatively inexpensive non-platinum based electrocatalysts provide attractive possibilities for electro-oxidation of small organic molecules. Pd-based electrocatalysts have been investigated as possible replacement for Pt-based electrocatalysts in alkaline media[133-136]. Recent preliminary studies of NiO and CeO_2 promoted Pd composites exhibited higher peak current densities and onset potentials than similar Pt-based electrocatalysts[136]. The possibility of employing nickel, cobalt and iron metals becomes more feasible in alkaline media compared to acid media as corrosion is moderated. Ru-Ni, Ru-Ni-Co and Ni-Fe-Co catalysts have shown encouraging activity for ethanol electro-oxidation[137, 138].

The aerosol synthesis technique developed for nanostructured Pt-Ru electrocatalysts for methanol oxidation was easily modified to the synthesis of

nanostructured ethanol oxidation alloys for DEFCs. The aerosol based synthesis methods developed in this work offer opportunities for extension to Pt-based and non-Pt based ternary catalyst systems by adjustments to the aerosol precursor solution.

9 Appendix A: Anion-Exchange MEA Experiments

This work represents an introduction to a robust alkaline anion exchange membrane that has been developed at Sandia National Laboratories which presents an opportunity for KOH-free AFCs. The membrane is made of a polymer which is comprised of a poly(phenylene) backbone with pendant benzyl trimethylammonium groups and which is based on similar sulfonated poly(phenylene) developed for PEM fuel cell applications[120]. Fabrication of membrane electrode assemblies (MEAs) requires in-depth investigations into the integration of the ionomer within the catalyst ink to realize a completely solid-phase MEA. This work presents one type of comparison between two alternative anion exchange ionomers within the catalyst ink, demonstrating the range of performances due to alternative catalyst ink formulations.

9.1 Experimental

9.1.1 Anion-Exchange Membrane Fabrication

The ATMPP ionomer shown in Figure 9.1 was prepared by making a poly(phenylene) with pendant 4-methylphenyl groups and then converting some of the methyl groups to benzyl trimethylammonium groups.

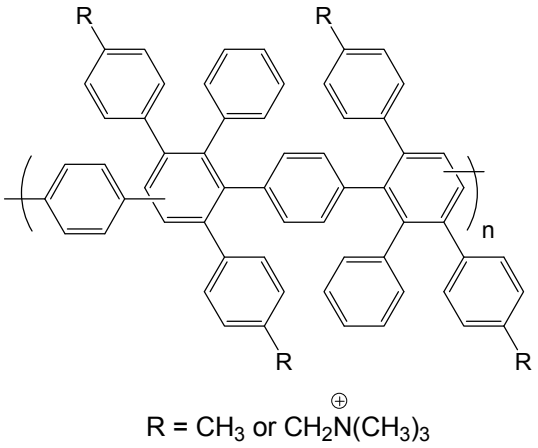

Figure 9.1: Structure of ATMPP ionomer.

The ratio of methyl to benzyl trimethylammonium groups in the polymer was 1.08. A detailed description of the cation exchange form of this polymer synthesis has been published elsewhere[120]. The material synthesis according to the method described previously has been modified to become an anion exchange ionomer.

The ATMPS ionomer shown in Figure 9.2 was prepared by making a poly(sulfone) with pendant methyl groups and then converting some of the methyl groups to benzyl trimethylammonium groups.

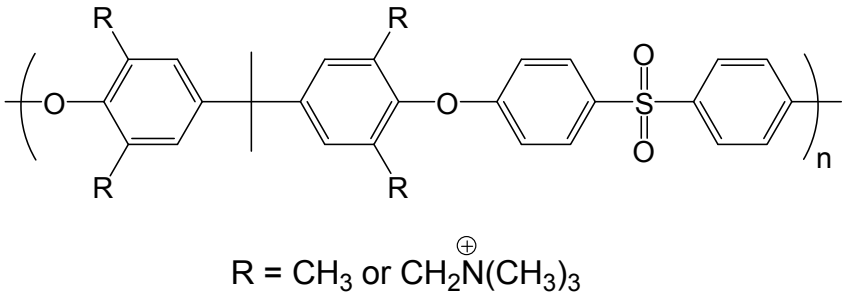

Figure 9.2: Structure of ATMPS ionomer.

Membranes were prepared by solution casting of an intermediate form of the polymer and then soaking the resulting films in aqueous trimethylamine to form the

benzyl trimethylammonium groups. Both the ATMPP and ATMPS ionomers were dissolved in a mixture of ethanol and water for integration into catalyst inks.

9.1.2 MEA Fabrication

All catalyst inks consisted of 10 mg Pt Black (Johnson-Matthey), 100 mg deionized water, 400 mg isopropanol and ionomer in an 80:20 catalyst:ionomer weight ratio. Each membrane electrode assembly (MEA) was fabricated in a similar way wherein the catalyst ink was spray painted onto a solid ATMPP alkaline membrane resulting in 2 mg of Pt/cm^2. A gas diffusion layer (GDL LT 1400-W Low temperature, ELAT(R) GDL microporous layer on woven web) was then applied on both the anode and cathode. The MEA was then pressed at 345 N cm^{-2} at 50°C for 10 min.

9.1.3 MEA Testing

The MEA was placed in a 5 cm^2 cell with serpentine flow channels and the bolts were compressed to 80 in-lbs. The Fuel Cell Technologies Fuel Cell Test Station was used to obtain H_2/O_2 and H_2/air polarization curves. Polarization curves were obtained galvanostatically with a 30 second delay before data actuation. The anode and cathode gases were heated and humidified at 85ºC, and the flow rates were 266 and 466 sccm, respectively. The cell operating temperature was maintained at 80ºC. Polarization curves were acquired at 0 and 30 psi backpressure.

9.2 Results

The effect of MEA cathode composition on performance was evaluated in a fuel cell test station under H_2/O_2 and H_2/air conditions. Polarization curves for oxygen and air are shown in Figure 9.3.

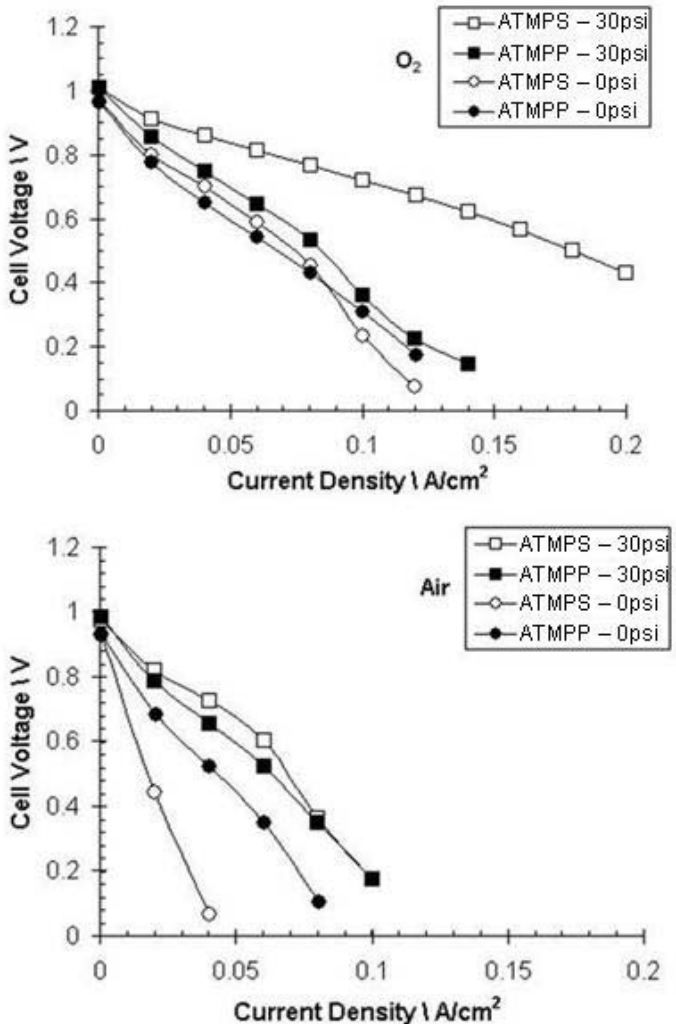

Figure 9.3: Polarization Curves at 80ºC of ATMPP and ATMPS ionomers in catalyst ink operating at zero and 30 psi cathodic backpressure of oxygen (above) and air (below).

The ATMPS ionomer in catalyst ink results in greatest overall fuel cell performance, especially evident at 30 psi. However, the ATMPS ionomer in catalyst ink

exhibits a large reduction in performance under no backpressure while the ATMPP catalyst ink remains relatively stable for 30 psi and no backpressure. The poorest overall performance occurs for the ATMPS catalyst ink at no backpressure.

Information on the limiting processes that occur in the catalyst layer during fuel cell operation can be exemplified with Delta E vs. *i* analysis. Delta E vs. *i* analysis is used to elucidate the transport hindrances that occur in the active layer that strongly influence the overall performance of the electrode. The analysis is done by first obtaining polarization curves in oxygen and air. Next, the difference of the potentials of the electrode while operating in oxygen and air at the same current density is taken. This difference in potentials is theoretically described by Equation 9-1 [139].

$$\Delta E = E_{O_2}(i) - E_{air}(i) = \frac{RT}{\alpha n F}\ln\left(\frac{P_{O_2}}{P_{air}}\right) + \frac{RT}{\alpha n F}\ln\left(\frac{f_{O_2}(i)}{f_{air}(i)}\right) \qquad \textbf{(9-1)}$$

The first term is independent of current and shows the oxygen partial pressure dependence. The second term incorporates the dependence on current density with the efficiency factors for oxygen f_{O2} and f_{air}. The efficiency factors are similar to effectiveness factor in that it is defined as the ratio of currents at a given potential for the real electrode and a hypothetical electrode with the same surface area and no transport losses. At high current densities the second term begins to increase because the efficiency of the electrode operated under air will decrease more rapidly than when under oxygen operation. For example, an electrode that operates relatively free of transport hindrances would produce a ΔE *vs i* curve with a small slope (i.e. flat line). While an electrode with severe transport hindrances would result in a curve with a steep slope.

This technique is used here to evaluate the transport processes that occur in the MEA catalyst layers incorporating the ATMPP and ATMPS ionomers. The ΔE vs. i plots are shown in Figure 9.4.

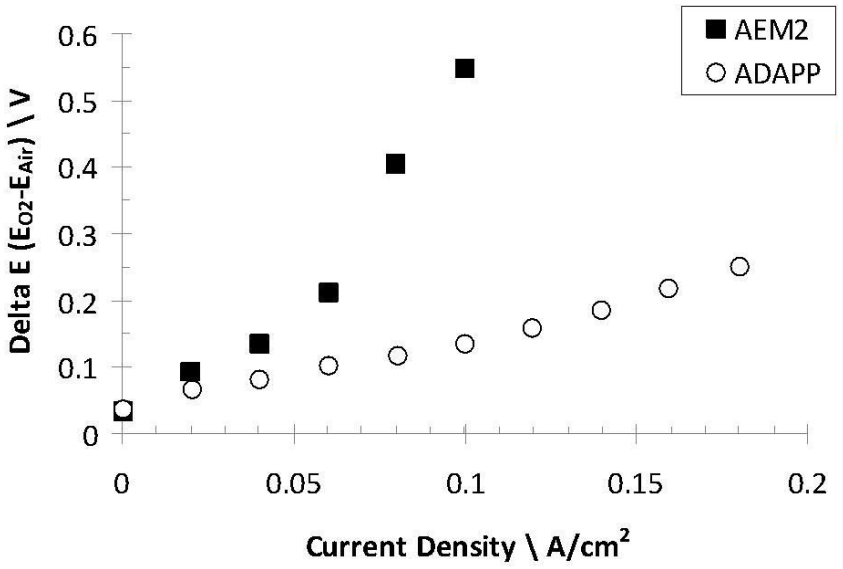

Figure 9.4: Delta E vs. i curves obtained from H_2/O_2 and H_2/Air polarization curves at 80°C and 30 psi backpressure.

It is evident from Delta E vs. *i* analysis that greater transport hindrances occur for in the active layer consisting of the ATMPS ionomer in the catalyst ink than for the ATMPP ionomer in the catalyst ink. This is exhibited in larger slope for the ATMPS MEA.

9.3 Conclusions

Introductory performance data for KOH-free AFCs employing a novel anion-exchange membrane has been shown. Delta E vs. *i* analysis shows only the effect of the cathodic concentration overpotential on electrode performance. Other limiting processes

that are occurring in the electrode and are not influenced by changing the reactant partial pressure are not accounted for in this study. Further investigation into the characteristics of these anion exchange ionomers is important. For example, gas permeability studies are in order. Also, hydrogen crossover was not accounted for in the analysis.

At this point, we can speculate that the random ordering of meta and para linkages in the ATMPP backbone as well as the large number of bulky side groups present make it difficult for the polymer chains to pack closely together in the solid state when compared to ATMPS. Both ionomers are amorphous but the inefficient packing of the ATMPP results in greater void volume which in turn leads to greater water swelling. The samples of ATMPP and ATMPS used in this study both had ion exchange capacity (IEC) values of 1.6 meq/g but films of each sample absorbed 103 and 48 % (by weight) respectively when allowed to equilibrate with water at room temperature. The increased water content in the ATMPP resulted in a higher hydroxide ion conductivity which is in agreement with the ΔE *vs i* curve analysis conclusion that there are greater transport hinderances in the ATMPS ionomer.

10 References

[1] J.D. K. Chan, J. Ren, S. Cheng, K. Y. Tsang, Journal of Materials Chemistry 14 (2004) 505.
[2] A.S. Arico, A.K. Shukla, K.M. El-Khatib, P. Creti, V. Antonucci, Journal of Applied Electrochemistry 29 (1999) 671-676.
[3] L. Liu, C. Pu, R. Viswanathan, Q. Fan, R. Liu, E.S. Smotkin, Electrochimica Acta 43 (1998) 3657.
[4] P. Argyropoulos, K. Scott, W.M. Taama, Electrochimica Acta 44 (1999) 3575-3584.
[5] E.M.B. C. Lamy, J.M. Leger, Journal of Applied Electrochemistry 31 (2001) 799-809.
[6] C.C. F. Vigier, A. Perrard, E.M. Belgsir, C. Lamy, Journal of Applied Electrochemistry 34 (2004) 439-446.
[7] A.L. C. Lamy, V. LeRhun, F. Delime, C. Coutanceau, J.M. Leger, Journal of Power Sources 105 (2002) 283-296.
[8] V. Rao, Hariyanto, C. Cremers, U. Stimming, Fuel Cells 7 (2007) 417-423.
[9] C.H. Hamann, A. Hamnet, W. Vielstich, Electrochemistry, Wiley-VCH, New York, 1998.
[10] Y. Bultel, Ozil, P. and R. Durand, Journal of Applied Electrochemistry 29 (1999) 1025-1033.
[11] Y. Bultel, Ozil, P. and R. Durand, Journal of Applied Electrochemistry 30 (2000) 1369-1376.
[12] F.a.R.D. Gloaguen, Journal of Applied Electrochemistry 27 (1997) 1029.
[13] J. Matthey, http://www.platinum.matthey.com/prices/price_charts.html, Historical Platinum Charts and Data
2008.
[14] J.S. Beck, J.C. Vartuli, W.J. Roth, M.E. Leonowicz, C.T. Kresge, K.D. Schmitt, C.T.W. Chu, D.H. Olson, E.W. Sheppard, S.B. McCullen, J.B. Higgins, J.L. Schlenker, Journal of the American Chemical Society 114 (1992) 10834-10843.
[15] C.T. Kresge, M.E. Leonowicz, W.J. Roth, J.C. Vartuli, J.S. Beck, Nature 359 (1992) 710-712.
[16] D.Y. Zhao, J.L. Feng, Q.S. Huo, N. Melosh, G.H. Fredrickson, B.F. Chmelka, G.D. Stucky, Science 279 (1998) 548-552.
[17] D.Y. Zhao, Q.S. Huo, J.L. Feng, B.F. Chmelka, G.D. Stucky, Journal of the American Chemical Society 120 (1998) 6024-6036.
[18] H.F. Y. Lu, A. Stump, T. Ward, T. Rieker, C. J. Brinker, Nature 398 (1999) 223.
[19] S.H.J. R. Ryoo, M. Kruk, M. Jaroniec, Advanced Materials 13 (2001) 677.
[20] J.F. C. Yu, B. Tian, D. Zhao, G. Stucky, Advanced Materials 14 (2002,) 1742.
[21] A. Fuertes, Journal of Materials Chemistry 13 (2003) 3085.
[22] M. Bore, T.L. Ward, A. Fukuoka, Catalysis Letters 98 (2004) 167-172.
[23] G.L. Egan, J. Yu, C.H. Kim, S.J. Lee, R.E. Schaak, T.E. Mallouk, Advanced Materials 2 (2001) 1040.
[24] C.H.K. H.J. Shin, R. Ryoo, Journal of Materials Chemistry 11 (2001) 260.

[25] Y.S. A. Fukuoka, S. Guan, S. Inagaki, N. Sugimoto, Y. Fukushima, K. Hirahara, S. Iijima, M. Ichikawa, Journal of the American Chemical Society 123 (2001) 3373.
[26] W.C. Choi, S.I. Woo, Journal of Power Sources 124 (2003) 420-425.
[27] R. Parsons, T. Vandernoot, Journal of Electroanalytical Chemistry 257 (1988) 9-45.
[28] W. Vielstich, Journal of the Brazilian Chemical Society 14 (2003) 503-509.
[29] T. Iwasita, Electrochimica Acta 47 (2002) 3663-3674.
[30] J.S. Spendelow, A. Wieckowski, Physical Chemistry Chemical Physics 6 (2004) 5094-5118.
[31] J.M. Leger, Journal of Applied Electrochemistry 31 (2001) 767-771.
[32] M. Watanabe, S. Motoo, Journal of Electroanalytical Chemistry 60 (1975) 267-273.
[33] M. Watanabe, S. Motoo, Journal of Electroanalytical Chemistry 60 (1975) 275-283.
[34] E.A. Batista, H. Hoster, T. Iwasita, Journal of Electroanalytical Chemistry 554 (2003) 265-271.
[35] E.A. Batista, G.R.P. Malpass, A.J. Motheo, T. Iwasita, Journal of Electroanalytical Chemistry 571 (2004) 273-282.
[36] C. Korzeniewski, C.L. Childers, Journal of Physical Chemistry B 102 (1998) 489-492.
[37] H. Hoster, T. Iwasita, H. Baumgartner, W. Vielstich, Physical Chemistry Chemical Physics 3 (2001) 337-346.
[38] T. Iwasita, H. Hoster, A. John-Anacker, W.F. Lin, W. Vielstich, Langmuir 16 (2000) 522-529.
[39] J.S. Spendelow, P.K. Babu, A. Wieckowski, Current Opinion in Solid State & Materials Science 9 (2005) 37-48.
[40] J.L. Cohen, D.J. Volpe, H.D. Abruna, Physical Chemistry Chemical Physics 9 (2007) 49.
[41] H. Wang, T. Loffler, H. Baltruschat, Journal of Applied Electrochemistry 31 (2001) 759-765.
[42] E.A. Batista, G.R.P. Malpass, A.J. Motheo, T. Iwasita, Electrochemistry Communications 5 (2003) 843-846.
[43] A. Ruban, B. Hammer, P. Stoltze, H.L. Skriver, J.K. Norskov, Journal of Molecular Catalysis A-Chemical 115 (1997) 421-429.
[44] M.S. Liao, C.R. Cabrera, Y. Ishikawa, Surface Science 445 (2000) 267-282.
[45] B. Hammer, Y. Morikawa, J.K. Norskov, Physical Review Letters 76 (1996) 2141-2144.
[46] M. Krausa, W. Vielstich, Journal of Electroanalytical Chemistry 379 (1994) 307-314.
[47] H.A. Gasteiger, N. Markovic, P.N. Ross, E.J. Cairns, Journal of Physical Chemistry 97 (1993) 12020-12029.
[48] H.A. Gasteiger, N. Markovic, P.N. Ross, E.J. Cairns, Electrochimica Acta 39 (1994) 1825-1832.
[49] M.T.M. Koper, J.J. Lukkien, A.P.J. Jansen, R.A. van Santen, Journal of Physical Chemistry B 103 (1999) 5522-5529.

[50] V.S. Bagotzky, Y.B. Vassiliev, O.A. Khazova, Journal of Electroanalytical Chemistry 81 (1977) 229-238.
[51] H.N. Dinh, X.M. Ren, F.H. Garzon, P. Zelenay, S. Gottesfeld, Journal of Electroanalytical Chemistry 491 (2000) 222-233.
[52] L. Dubau, C. Coutanceau, E. Garnier, J.M. Leger, C. Lamy, Journal of Applied Electrochemistry 33 (2003) 419-429.
[53] A. Kabbabi, R. Faure, R. Durand, B. Beden, F. Hahn, J.M. Leger, C. Lamy, Journal of Electroanalytical Chemistry 444 (1998) 41-53.
[54] K.W. Park, Y.E. Sung, Journal of Industrial and Engineering Chemistry 12 (2006) 165-174.
[55] J.S. Spendelow, J.D. Goodpaster, P.J.A. Kenis, A. Wieckowski, Langmuir 22 (2006) 10457-10464.
[56] Z.Y. Zhou, N. Tian, Y.J. Chen, S.P. Chen, S.G. Sun, Journal of Electroanalytical Chemistry 573 (2004) 111-119.
[57] J.S. Spendelow, A. Wieckowski, Physical Chemistry Chemical Physics 9 (2007) 2654-2675.
[58] B. Beden, F. Kadirgan, C. Lamy, J.M. Leger, Journal of Electroanalytical Chemistry 142 (1982) 171-190.
[59] E. Morallon, A. Rodes, J.L. Vazquez, J.M. Perez, Journal of Electroanalytical Chemistry 391 (1995) 149-157.
[60] A.V. Tripkovic, N. Marinkovic, K.D. Popovic, R.R. Adzic, Russian Journal of Electrochemistry 31 (1995) 993-1003.
[61] J.M. Perez, E. Munoz, E. Morallon, F. Cases, J.L. Vazquez, A. Aldaz, Journal of Electroanalytical Chemistry 368 (1994) 285-291.
[62] A.V. Tripkovic, K.D. Popovic, J.D. Momcilovic, D.M. Drazic, Journal of Electroanalytical Chemistry 418 (1996) 9-20.
[63] A.V. Tripkovic, K.D. Popovic, B.N. Grgur, B. Blizanac, P.N. Ross, N.M. Markovic, Electrochimica Acta 47 (2002) 3707-3714.
[64] J. Luo, P.N. Njoki, Y. Lin, D. Mott, L.Y. Wang, C.J. Zhong, Langmuir 22 (2006).
[65] W.J. Zhou, Z.H. Zhou, S.Q. Song, W.Z. Li, G.Q. Sun, P. Tsiakaras, Q. Xin, Applied Catalysis B-Environmental 46 (2003) 273-285.
[66] S.Q. Song, W.J. Zhou, Z.H. Zhou, L.H. Jiang, G.Q. Sun, Q. Xin, V. Leontidis, S. Kontou, P. Tsiakaras, International Journal of Hydrogen Energy 30 (2005) 995-1001.
[67] C. Lamy, E. Rousseau, E.M. Belgsir, C. Coutanceau, J.-M. Leger, Electrochimica Acta 49 (2004).
[68] T. Iwasita, B. Rasch, E. Cattaneo, W. Vielstich, Electrochimica Acta 34 (1989) 1073-1079.
[69] S.R. J.M. Leger, C. Coutanceau, F. Hahn, C. Lamy, Electrochimica Acta 50 (2005) 5118-5125.
[70] H. Wang, Z. Jusys, R.J. Behm, Journal of Physical Chemistry B 108 (2004) 19413-19424.
[71] T. Iwasita, W. Vielstich, Journal of Electroanalytical Chemistry 257 (1988) 319-324.
[72] B. Bittinscattaneo, S. Wilhelm, E. Cattaneo, H.W. Buschmann, W. Vielstich, Berichte Der Bunsen-Gesellschaft-Physical Chemistry Chemical Physics 92 (1988) 1210-1218.

[73] P. Bommersbach, M. Mohamedi, D. Guay, Journal of the Electrochemistry Society 154 (2007).
[74] E. Antolini, Journal of Power Sources 170 (2007).
[75] F. Vigier, C. Coutanceau, F. Hahn, E.M. Belgsir, C. Lamy, Journal of Electroanalytical Chemistry 563 (2004).
[76] E.V. Spinace, M. Linardi, A. Oliveira Neto, Electrochemistry Communications 7 (2005).
[77] S. Tanaka, M. Umeda, H. Ojima, Y. Usui, O. Kimura, I. Uchida, Journal of Power Sources 152 (2005).
[78] G. Stalnionis, L. Tamasauskaite, V. Pautieniene, Z. Jusys, Journal of Solid State Electrochemistry 8 (2004).
[79] F. Colmati, E. Antolini, E.R. Gonzalez, Journal of the Electrochemistry Society 154 (2007).
[80] J.S. Spendelow, G.Q. Liu, P.J.A. Kenis, A. Wieckowski, Journal of Electroanalytical Chemistry 568 (2004).
[81] M. Lopezatalaya, E. Morallon, F. Cases, J.L.K. Vazquez, J.M. Perez, Journal of Power Sources 52 (1994) 109-117.
[82] A.A. Elshafei, S.A.A. Elmaksoud, M.N.H. Moussa, Journal of Electroanalytical Chemistry 336 (1992) 73-83.
[83] C.W. Xu, P.K. Shen, Journal of Power Sources 142 (2005) 27-29.
[84] Y.X. Bai, J.J. Wu, J.Y. Xi, J.S. Wang, W.T. Zhu, L.Q. Chen, X.P. Qiu, Electrochemistry Communications 7 (2005) 1087-1090.
[85] C. Xu, P.K. Shen, X. Ji, R. Zeng, Y. Liu, Electrochemistry Communications 7 (2005).
[86] J. Bagchi, S.K. Bhattacharya, Journal of Power Sources 163 (2007) 661-670.
[87] E.A. Batista, T. Iwasita, W. Vielstich, Journal of Physical Chemistry B 108 (2004) 14216-14222.
[88] N.P. Lebedeva, M.T.M. Koper, J.M. Feliu, R.A. van Santen, Journal of Electroanalytical Chemistry 524 (2002) 242-251.
[89] N.P. Lebedeva, M.T.M. Koper, J.M. Feliu, R.A. van Santen, Journal of Physical Chemistry B 106 (2002) 12938-12947.
[90] N.P. Lebedeva, A. Rodes, J.M. Feliu, M.T.M. Koper, R.A. van Santen, Journal of Physical Chemistry B 106 (2002) 9863-9872.
[91] A. Cuesta, A. Couto, A. Rincon, M.C. Perez, A. Lopez-Cudero, C. Gutierrez, Journal of Electroanalytical Chemistry 586 (2006) 184-195.
[92] A. Lopez-Cudero, A. Cuesta, C. Gutierrez, Journal of Electroanalytical Chemistry 586 (2006) 204-216.
[93] M. Bergelin, E. Herrero, J.M. Feliu, M. Wasberg, Journal of Electroanalytical Chemistry 467 (1999) 74-84.
[94] N.M. Markovic, T.J. Schmidt, B.N. Grgur, H.A. Gasteiger, R.J. Behm, P.N. Ross, Journal of Physical Chemistry B 103 (1999) 8568-8577.
[95] T.J. Schmidt, P.N. Ross, N.M. Markovic, Journal of Physical Chemistry B 105 (2001).
[96] S.G. Sun, A.C. Chen, Journal of Electroanalytical Chemistry 323 (1992) 319-328.
[97] J.S. Spendelow, J.D. Goodpaster, P.J.A. Kenis, A. Wieckowski, Journal of Physical Chemistry B 110 (2006) 9545-9555.

[98] M.T.M. Koper, A.P.J. Jansen, J.J. Lukkien, Electrochimica Acta 45 (1999) 645-651.
[99] H. Gasteiger, S. Kocha, B. Sompalli, F. Wagner, Applied Catalysis B: Environmental 56 (2005) 9-35.
[100] F. Gloaguen, F. Andolfatto, R. Durand, P. Ozil, Journal of Applied Electrochemistry 24 (1994) 863-869.
[101] T.J. Schmidt, H.A. Gasteiger, G.D. Stab, P.M. Urban, D.M. Kolb, R.J. Behm, Journal of the Electrochemical Society 145 (1998) 2354-2358.
[102] M. Watanabe, H. Igarashi, K. Yosioka, Electrochimica Acta 40 (1995) 329-334.
[103] J.W. Guo, J. Prabhuram, R. Chen, C.W. Wong, Electrochimica Acta 51 (2005).
[104] V. Radmilovic, H.A. Gasteiger, P.N. Ross, Journal of Catalysis 154 (1995) 98-106.
[105] C. Bock, M.A. Blakely, B. MacDougall, Electrochimica Acta 50 (2005) 2401-2414.
[106] D.G. Liu, J.F. Lee, M.T. Tang, Journal of Molecular Catalysis A-Chemical 240 (2005) 197-206.
[107] B.J. Hwang, C.H. Chen, L.S. Sarma, J.M. Chen, G.R. Wang, M.T. Tang, D.G. Liu, J.F. Lee, Journal of Physical Chemistry B 110 (2006) 6475-6482.
[108] S.Y. Huang, S.M. Chang, C.L. Lin, C.H. Chen, C.T. Yeh, Journal of Physical Chemistry B 110 (2006) 23300-23305.
[109] H. Kim, I.R. de Moraes, G. Tremiliosi, R. Haasch, A. Wieckowski, Surface Science 474 (2001) L203-L212.
[110] C. Bock, A. Collier, B. MacDougall, Journal of the Electrochemical Society 152 (2005) A2291-A2299.
[111] R.A. Stroud, J.W. Long, K.E. Swider-Lyons, D.R. Rolison, Microscopy and Microanalysis 8 (2002) 50-57.
[112] C. Xu, Y.L. He, T.S. Zhao, R. Chen, Q. Ye, Journal of the Electrochemical Society 153 (2006) A1358-A1364.
[113] C.W. Wong, T.S. Zhao, Q. Ye, J.G. Liu, Journal of Power Sources 155 (2006) 291-296.
[114] E.E. Switzer, A.K. Datye, P. Atanassov, Topics in Catalysis 46 (2007).
[115] L. Jiang, Z. Zhou, W. Li, W. Zhou, S. Song, H. Li, G. Sun, Q. Xin, Energy & Fuels 18 (2004).
[116] G. Li, P.G. Pickup, Journal of Power Sources 173 (2007).
[117] V.I. Kuznetsov, A.S. Belyi, E.N. Yurchenko, M.D. Smolikov, M.T. Protasova, E.V. Zatolokina, V.K. Duplayakin, Journal of Catalysis 99 (1986).
[118] S. Mukerjee, S. Srinivasan, Journal of Electroanalytical Chemistry 357 (1993) 201-224.
[119] S. Mukerjee, S. Srinivasan, M.P. Soriaga, J. McBreen, Journal of the Electrochemical Society 142 (1995) 1409-1422.
[120] C.J. Fujimoto, M.A. Hickner, C.J. Cornelius, D.A. Loy, Macromolecules 38 (2005).
[121] H.P. Liu, J.Q. Ye, C.W. Xu, S.P. Jiang, Y.X. Tong, Journal of Power Sources 177 (2008) 67-70.
[122] F. Hu, F. Ding, S. Song, P. Shen, Journal of Power Sources 163 (2006).
[123] C. Xu, P. Shen, Y. Liu, Journal of Power Sources 164 (2007).

[124] J. Bagchi, S. Bhattacharya, Journal of Power Sources 163 (2007).
[125] H.A. Gasteiger, N.M. Markovic, P.N. Ross, Journal of Physical Chemistry 99 (1995).
[126] T. Kawaguchi, W. Sugimoto, Y. Murakami, Y. Takasu, Electrochemistry Communications 6 (2004).
[127] J.S. Spendelow, G.Q. Lu, P.J.A. Kenis, A. Wieckowski, Journal of Electroanalytical Chemistry 568 (2004) 215-224.
[128] M. Alsabet, M. Grden, G. Jerkiewicz, Journal of Electroanalytical Chemistry 589 (2006) 120-127.
[129] S.N. Raicheva, M.V. Christov, E.I. Sokolova, Electrochimica Acta 26 (1981) 1669-1676.
[130] J.P.I. de Souza, S.L. Queiroz, K. Bergamaski, E.R. Gonzalez, F.C. Nart, Journal of Physical Chemistry B 106 (2002) 9825-9830.
[131] S. Sen Gupta, J. Datta, Journal of Electroanalytical Chemistry 594 (2006) 65-72.
[132] F. Colmati, E. Antolini, E.R. Gonzalez, Journal of Alloys and Compounds 456 (2008) 264-270.
[133] F.P. Hu, C.L. Chen, Z.Y. Wang, G.Y. Wei, P.K. Shen, Electrochimica Acta 52 (2006) 1087-1091.
[134] F.P. Hu, F.W. Ding, S.Q. Song, P.K. Shen, Journal of Power Sources 163 (2006) 415-419.
[135] C.W. Xu, L.Q. Cheng, P.K. Shen, Y.L. Liu, Electrochemistry Communications 9 (2007) 997-1001.
[136] C.W. Xu, P.K. Shen, Y.L. Liu, Journal of Power Sources 164 (2007) 527-531.
[137] M.R. Tarasevich, Z.R. Karichev, V.A. Bogdanovskaya, E.N. Lubnin, A.V. Kapustin, Electrochemistry Communications 7 (2005) 141-146.
[138] J.W. Kim, S.M. Park, Journal of the Electrochemical Society 150 (2003) E560-E566.
[139] A. Kaisheva, I. Iliev, S. Gamburzev, Journal of Power Sources 13 (1984) 181-195.

11 Distribution

1	MS0123	Dona Chavez, LDRD Office	01011	
1	MS0734	J. Bruce Kelley	06327	
1	MS0734	Ellen Stechel	06338	
1	MS0888	Michael Hibbs	06338	
1	MS0888	Cy Fujimoto	06338	
1	MS1349	William F. Hammetter	01815	
1	MS0899	Technical Library	09536	(electronic copy)


Sandia National Laboratories